REGULATION OF RHYTHMIC ACTIVITY IN THE STOMATOGASTRIC GANGLION OF DECAPOD CRUSTACEANS

A Dissertation
Presented to
The Academic Faculty

by

Wafa Ahmed Soofi

In Partial Fulfillment
of the Requirements for the Degree
Doctor of Philosophy in the
School of Biomedical Engineering

Georgia Institute of Technology
May 2014

REGULATION OF RHYTHMIC ACTIVITY IN THE STOMATOGASTRIC GANGLION OF DECAPOD CRUSTACEANS

Approved by:

Dr. Astrid A. Prinz, Advisor
Department of Biology
Emory University

Dr. Wolfgang Stein
School of Biological Sciences
Illinois State University

Dr. Robert J. Butera
Department of Biomedical Engineering &
Department of Electrical Engineering
Georgia Institute of Technology

Dr. Samuel J. Sober
Department of Biology
Emory University

Dr. Carmen Canavier
School of Medicine
Louisiana State University

Date Approved: March 27, 2014

To

Naheed Ahmed
Khalid Soofi
Nicholas Kong

ACKNOWLEDGEMENTS

I would first like to thank my advisor, Dr. Astrid Prinz, for guiding me through the process of learning to be a better scientist. Astrid's expert advice throughout my graduate career, on subjects covering everything from troubleshooting experimental protocols to navigating the world after graduate school, has been indispensible to the completion of this dissertation. Astrid, thanks for all of your help during these years; you are one of the best scientists (and teachers) I have ever met.

I would also like to thank Dr. Wolfgang Stein for letting me temporarily join his lab and allocating considerable resources to our *in vivo* project. Wolfie, thanks for your time and patience; it was a real pleasure to work with you. To Ursula and the Stein Lab: Carola, Florian, Astrid, Steffy - thanks for patiently helping me with experimental protocols and for making my time in Germany a wonderful one.

I would like to extend my gratitude to Dr. Carmen Canavier and Dr. Robert Butera for their crucial intellectual contributions to the PRC project. This work has been enjoyable because of the constructive atmosphere of our many discussions throughout the years. Thanks, also, to Dr. Sam Sober for always being available for discussions about analytical methods, as well as "the big picture."

I would also like to extend my heartfelt thanks to the members of the Prinz lab, past and present, for their scientific advice and camaraderie. Amber, Ryan, Santiago, Fred, Cengiz, Andrei, Tomasz, Fatima, Logesh, Rebecca, Claire, Wanlu, and Lin: Thank you all so much. Stay in touch, and I wish you the absolute best in your futures.

Thanks to the Marder Lab for making our collaboration on the *in vivo* work possible.

Thank you to the National Science Foundation for funding five years of my graduate career and to the National Institutes of Health for additional support.

Thanks to SomaFM for preserving my sanity over many, many long days and nights.

To my family: Thank you for getting me 99.9% of the way there.

And finally, to Nicholas: Thank you so much for being an incredible partner. You have made me a better person, and I cannot wait to experience our future years together.

TABLE OF CONTENTS

LIST OF TABLES

Page

LIST OF FIGURES

Page

LIST OF SYMBOLS AND ABBREVIATIONS

CPG	Central Pattern Generator
STG	Stomatogastric Ganglion
STNS	Stomatogastric Nervous System
AB	Anterior Burster Neuron
PD	Pyloric Dilator Neuron
LP	Lateral Pyloric Neuron
PY	Pyloric Constrictor Neuron
LPG	Lateral Posterior Gastric Neuron
GM	Gastric Mill
CoG	Commissural Ganglion
OG	Esophageal Ganglion
dvn	Dorsal Ventricular Nerve
lvn	Lateral Ventricular Nerve
I_{Na}	Fast Na^+ Current
g_{Na}	Fast Na^+ Conductance
I_{CaT}	Fast Transient Ca^{2+} Current
g_{CaT}	Fast Transient Ca^{2+} Conductance
I_{CaS}	Slow Transient Ca^{2+} Current
g_{CaS}	Slow Transient Ca^{2+} Conductance
I_A	A-type Transient K^+ Current
g_A	A-type Transient K^+ Conductance
I_{KCa}	Calcium-dependent K^+ Current
g_{KCa}	Calcium-dependent K^+ conductance
I_{Kd}	Delayed Rectifier K^+ Current

g_{Kd}	Delayed Rectifier K^+ Conductance
I_H	Hyperpolarization-activated Mixed Ion Current
g_H	Hyperpolarization-activated Mixed Ion Conductance
I_{leak}	Leak Current
g_{leak}	Leak Conductance
V_m	Membrane Potential
E_i	Reversal Potential
m	Activation Variable
h	Inactivation Variable
mRNA	Messenger RNA
PRC	Phase Resetting Curve
DCC	Discontinuous Current Clamp
KCl	Potassium Chloride
NaCl	Sodium Chloride
$CaCl_2 \cdot 2H_2O$	Calcium Chloride Dihydrate
$MgCl_2 \cdot 6H_2O$	Magnesium Chloride Hexahydrate
mM	milliMolar
AC	Alternating Current
ISI	Inter-Spike Interval
IBI	Inter-Burst Interval
PM	Phase Maintenance
DC	Duty Cycle
ρ	Spearman's rho
X^2	Chi-squared Statistic

SUMMARY

Neuronal networks produce reliable functional output throughout the lifespan of an animal despite ceaseless molecular turnover and a constantly changing environment. The cellular and molecular mechanisms underlying the ability of these networks to maintain functional stability remain poorly understood. Central pattern generating circuits produce a stable, predictable rhythm, making them ideal candidates for studying mechanisms of activity maintenance. By identifying and characterizing the regulators of activity in small neuronal circuits, we not only obtain a clearer understanding of how neural activity is generated, but also arm ourselves with knowledge that may eventually be used to improve medical care for patients whose normal nervous system activity has been disrupted through trauma or disease. We utilize the pattern-generating pyloric circuit in the crustacean stomatogastric nervous system to investigate the general scientific question: How are specific aspects of rhythmic activity regulated in a small neuronal network?

The first aim of this thesis poses this question in the context of a single neuron. We used a single-compartment model neuron database to investigate whether co-regulation of ionic conductances supports the maintenance of spike phase in rhythmically bursting "pacemaker" neurons. The second aim of the project extends the question to a network context. Through a combination of computational and electrophysiology studies, we investigated how the intrinsic membrane conductances of the pacemaker neuron influence its response to synaptic input within the framework of the Phase Resetting Curve (PRC). The third aim of the project further extends the question to a systems-level context. We examined how ambient temperatures affect the stability of the pyloric rhythm in the intact, behaving animal. The results of this work have furthered our understanding of the principles underlying the long-term stability of neuronal network function.

CHAPTER 1

INTRODUCTION

1.1 Activity maintenance

The nervous systems of all animals, including humans, are in a constant state of flux. From birth to death, the nervous system is continuously undergoing chemical and electrical changes at the subcellular, cellular, and network levels. Properly functioning nervous systems perform certain tasks, such as breathing, walking, or recalling one's home address, with rigid consistency, while also remaining malleable enough to continually assimilate new information from the environment, such as the phone number of a new acquaintance. How does the nervous system maintain this crucial balance between memory and learning, between stability and plasticity? What is happening at the genetic, subcellular, cellular, and network levels? The field of neuroscience has not yet revealed complete answers to these questions.

Tracing the neuronal mechanisms underlying stability and plasticity in human nervous systems is a complex undertaking. Presently, our technology is not advanced enough to unambiguously tease apart the many interdependent phenomena that underlie mammalian nervous system output. To understand the mechanisms of activity regulation, it is necessary to start with a biological nervous system small enough that its *intrinsic properties* and *output* can be exhaustively characterized. Only in such a system can we begin to determine the relationships between nervous system structure and function.

Central pattern generating circuits (CPGs) are a type of neuronal circuit with output that is well suited to studying the mechanisms of maintaining stable activity (Marder and Bucher 2007). CPGs produce stereotyped outputs and control crucial behaviors such as walking, breathing, and chewing in both vertebrates and invertebrates. They exhibit rhythmic output in the absence of rhythmic descending or sensory input and can thus be

studied in isolation under controlled conditions (Chevallier et al. 2008; Marder and Bucher 2007). CPGs have output with a generally well-defined "set point." Deviations from this set point can be quantified; thus, in CPGs, the degree to which activity is maintained can be determined with relative ease.

To properly study mechanisms of activity maintenance, it is best to utilize a system with intrinsic cellular and synaptic properties that can be rigorously characterized. I now describe the stomatogastric nervous system, a biological preparation that fulfills these criteria.

1.2 The stomatogastric nervous system

The stomatogastric nervous system (STNS), an extension of the central nervous system of decapod crustaceans, controls rhythmic movements of the stomach (Fig. 1A, 1C). The STNS, diagrammed in Figure 1B, contains four ganglia, including the commissural ganglia (CoGs), the esophageal ganglion (OG), and the stomatogastric ganglion, or STG. The STG contains neurons that constitute two central pattern generating circuits, including the gastric mill circuit, which controls the muscles involved in chewing, and the pyloric circuit, which controls the pylorus, an apparatus that filters chewed food (Stein 2009). The pyloric circuit includes a pacemaker kernel that consists of three electrically coupled neuron types – the single anterior burster (AB), the two pyloric dilator neurons (PDs), and the two lateral posterior gastric neurons (LPGs). The pacemaker kernel is connected via inhibitory synapses to the single lateral pyloric neuron (LP) and the 4 or 5 (or more, depending on species) pyloric (PY) neurons. The pyloric circuit produces the triphasic pyloric rhythm, which consists of a burst of action potentials from the PD neurons, followed by a burst from the LP neuron, and then by a burst from the PY neurons (Figure 2).

The STNS, and the pyloric circuit in particular, is advantageous for studying the regulators of neuronal activity for a number of reasons. First, when the entire STNS is

removed from the animal and placed into a petri dish filled with cold saline, it continues to produce fictive patterns that are similar to those made in the intact animal (Hartline and Maynard 1975). Since the pyloric circuit consists of motor neurons, the output of the neurons is aligned with the operation of the musculature. Second, the identity of each STG neuron can be determined solely from intracellular recordings of the somata. We can thus study specific STG neurons in multiple preparations under rigorously controlled conditions. Third, it is possible to simultaneously record intracellular activity from multiple neurons in addition to extracellular recordings from descending nerve fibers. Thus, in a typical experimental setup, we can continuously measure the activity of individual neurons as well as the system as a whole. Fourth, through the use of pharmacological blockers and voltage clamp, we can also characterize individual currents in each neuron, allowing us to determine both intrinsic properties and output parameters of a single preparation. Finally, the pyloric rhythm is nearly always spontaneously active (Figure 2), making it a prime example of well-maintained neuronal activity (Marder and Bucher 2007).

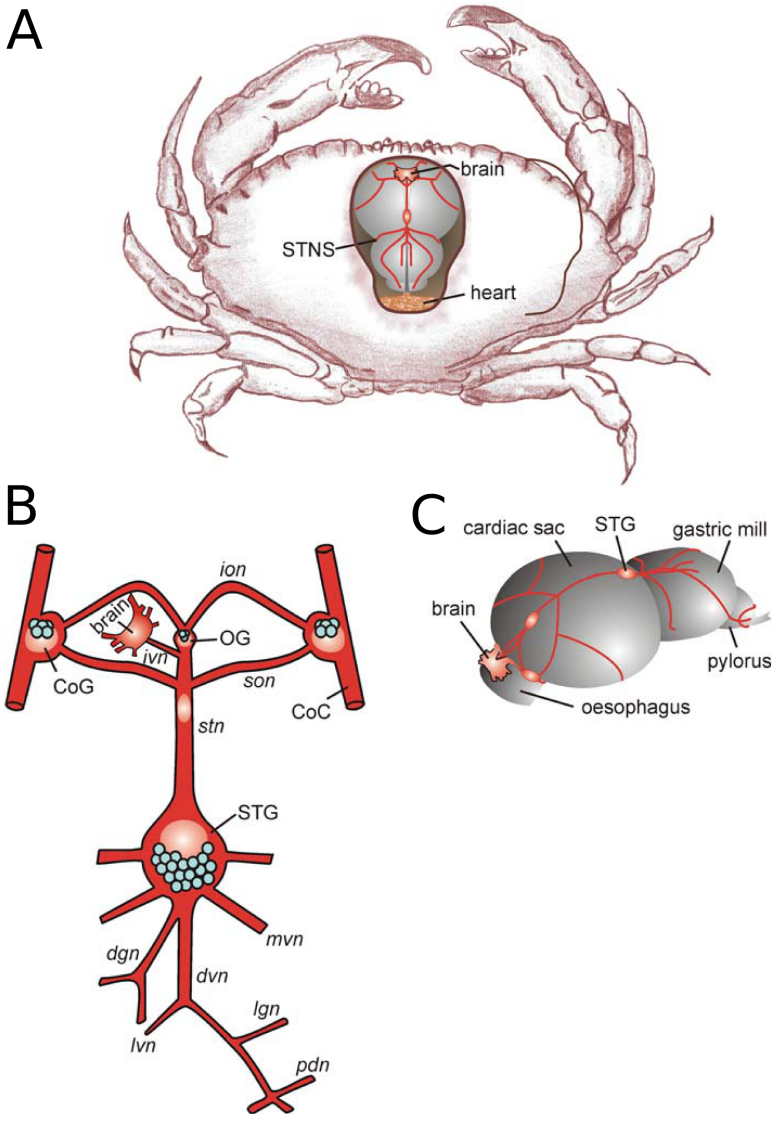

Figure 1. The stomatogastric ganglion is found in the stomatogastric nervous system of decapod crustaceans. (A) Dorsal view of *Cancer borealis*. In this diagram, the part of the carapace directly above the stomach is removed to show the STNS, heart, and brain. (B) Diagram of the STNS. The paired commissural ganglia (CoGs) and esophageal ganglion (OG) provide descending input to the STG. The STG consists of 26-30 neurons (blue circles), of which a subset constitutes the gastric mill and pyloric CPGs. Pyloric network activity is measured via extracellular recordings from the descending dorsal ventricular nerve (*dvn*) and lateral ventricular nerves (*lvn*s). (C) Locations of various parts of the foregut relative to the STNS (shown in red). The STG, which contains CPGs that control the gastric mill and pylorus, is located within the ophthalmic artery (not shown). The hemolymph within the artery contains numerous neuromodulatory substances that can influence CPG activity. Figure originally published in J Comp Physiol A (2009) 195:991 "Modulation of Stomatogastric Rhythms" by Wolfgang Stein as Fig. 1. Reproduced from (Stein 2009) with kind permission from Springer Science and Business Media.

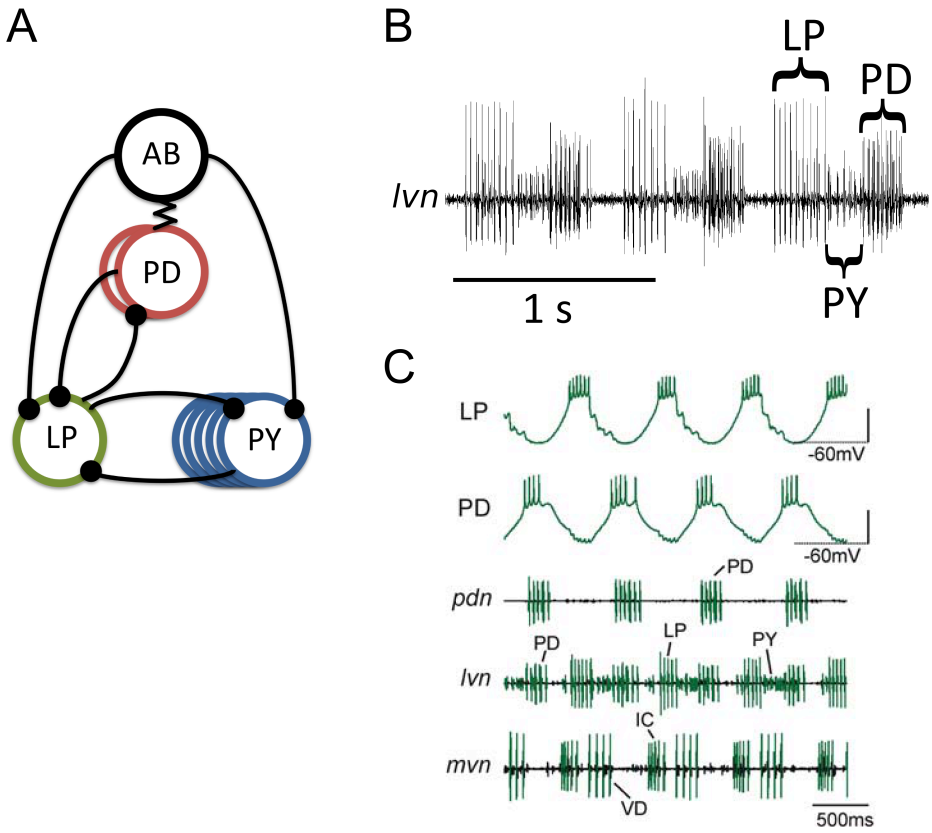

Figure 2. The pyloric circuit produces the triphasic pyloric rhythm. (A) Diagram of the pyloric circuit. Zigzag lines indicate electrical couplings, and black dots indicate inhibitory synapses. The AB (black) and PD (red) neurons constitute the pacemaker kernel, which connects via inhibitory synapses to the LP (green) and PY (blue) follower neurons. (B) Extracellular recording from the *lvn*, showing the pyloric rhythm. The PD neurons burst first; this is followed by a burst from the LP neuron, which is followed by a burst from the PY neurons. This triphasic rhythm has a frequency that is usually on the order of 1 Hz. (C) Simultaneous intracellular recordings of the LP and PD neurons and extracellular traces from the pyloric dilator nerve (*pdn*), *lvn*, and median ventricular nerve (*mvn*), on which bursts from the inferior cardiac (IC) and ventricular dilator (VD) neurons are visible. Traces are not from the same recording as (B). Vertical scale bar is 13 mV for LP and 20 mV for PD. Panel C originally published in J Comp Physiol A (2009) 195:992 "Modulation of Stomatogastric Rhythms" by Wolfgang Stein as Fig. 2b. Reproduced from (Stein 2009) with kind permission from Springer Science and Business Media.

1.3 Natural variability of cellular parameters

To relate the input to the output of a small neuronal network, we need to have a quantitative understanding of the intrinsic properties of the individual neurons within that

network (Prinz et al. 2004b). Neurons, like all cells, have a membrane composed of a lipid bilayer that has many types of ion channels embedded within it. These ion channels conduct current between the intracellular and extracellular sides of the membrane by allowing ions to flow through them. Many ion channels are highly selective and will only conduct certain ions based upon their charge or size. In addition, the channels' ability to conduct ions is dependent upon chemical, mechanical, and/or electrical cues. The current conducted by these ion channels can modify the neuron's membrane voltage extremely rapidly. These changes in membrane voltage are manifested in the form of action potentials and postsynaptic potentials in neighboring cells – crucial signaling processes in the nervous system (Kandel et al. 2000). The current that flows through each type of ion channel can be calculated with a modified version of Ohm's law that considers the gating properties of the ion channels, the maximal ion channel conductance, and the reversal potential of each ionic current:

$$I_i = \bar{g}_i m_i^p h_i (V_m - E_i)$$

Here, I_i is the current of ion i, V_m is the membrane voltage, and E_i is the reversal potential of ion i. The parameter $\bar{g}_i$ is the ion channel type's maximal conductance. This is the conductance value for each ion channel type when all individual ion channels are completely open and conducting the maximum amount of current. This parameter is dependent upon the total number of channels of type i embedded in the membrane. m_i^p is the voltage-dependent activation variable of ion channel type i; p is its associated exponent. h_i is the voltage-dependent inactivation variable of ion channel type i.

These equations, extended from the original Hodgkin and Huxley model for the electrical activity of the squid giant axon, constitute a highly successful mechanistic, mathematical model of a biological neuron. We can use a system of such equations to build conductance-based models of STG neurons, and in so doing, perform careful and

systematic analyses of the relationships between input parameters and output measures (Prinz 2010).

We know from measurements of conductances in lobsters and crab STG neurons that the maximal conductances can have a wide range of values (Marder and Goaillard 2006). Differences in conductance levels between animals, and at different times in the same animal (MacLean et al. 2005; MacLean et al. 2003), can have large effects on neuronal activity. In addition, certain STG neurons co-regulate specific ionic conductances to maintain aspects of neuronal activity. Experimentally modifying I_A, for example, results in an endogenous increase in I_H with little change in neuronal output (MacLean et al. 2003). Ion channel densities are thus *intrinsic neuronal parameters that are key regulators of neuronal activity.*

In summary, over the past several decades, we have developed a solid grasp of both the *structure* and the *output* of the crustacean stomatogastric ganglion. By simultaneously measuring intrinsic cellular properties, synaptic properties, cellular output, and network output, we can find associations between changes in network properties and changes in activity. These findings have brought us much insight into mechanisms of activity regulation in small invertebrate neuronal networks (Marder 2011).

Experimental examination of network properties and network output is necessary for initial characterization of the system, but due to technical limitations, only a small number of parameters can be measured or manipulated at any time. However, after experimentally isolating specific currents and determining their Hodgkin-Huxley parameters, we can now generate mechanistic models of STG neurons based upon a system of Hodgkin-Huxley equations that allow us to predict neuronal output given a set of input parameters. By using these types of neuron models, known as "conductance-based models," we can explore the effects of a much greater number of parameters than is possible with experimental preparations. In the next section, we further describe the

utility of conductance-based single-neuron and network models in understanding structure-output relationships.

1.4 Structure-output relationships in conductance-based model neurons and neuronal networks

Sections 1.4 - 1.6 are adapted from a chapter to be published in the forthcoming book *Computational Modeling of Central Pattern Generators: Principles and Challenges of Neuronal Network Design* (Springer; editors: Dr. Erik Sherwood and Dr. Silvia Daun-Gruhn). This chapter was written in collaboration with Dr. Astrid A. Prinz.

Ever since Ramon y Cajal's development of the "neuron doctrine," which states that nervous systems consist of independent cellular units (Cajal 1888; DeFelipe 2010), neuroscientists have been interested in mapping the *network architecture* of these systems – i.e., which neurons are connected to which other neurons, how strongly, and with what type of synapse. The complete set of synaptic connections between neurons in a network is also commonly referred to as the *connectome.* Ambitious efforts are underway to characterize the architecture of such complex networks as the mammalian retina (Anderson et al. 2011), neuromuscular circuits in mammals (Lu et al. 2009), and, on a larger scale, regions of the human brain (Akil et al. 2011; Craddock et al. 2013; Helmstaedter 2013). While a complete map of the architecture is necessary to fully understand these highly complex networks, it is not sufficient. To take the next step in understanding the significance of a network's architecture, we must be able to characterize its relationship to the network's output. In other words, we need to know: How specific is the relationship between network architecture and network function? Can a variety of different network architectures result in the same network output? Conversely, can the same network architecture result in different network outputs? Furthermore, and beyond connectivity and synaptic parameters, what role do intrinsic

cellular parameters, such as membrane conductances, play in determining network output? To answer these questions, we must utilize model systems for which the network architecture, cellular parameters, and network output are readily characterized.

Small central pattern generating (CPG) circuits, including the pyloric circuit in the stomatogastric ganglion, are especially well suited for studying the relationship between network architecture and output. Over the past several decades, many computational and experimental studies have been performed on the STG to assess the relationship of network parameters to network output (Goaillard et al. 2009; Goldman et al. 2001; Prinz et al. 2004b; Taylor et al. 2009; Turrigiano et al. 1995). Before discussing the particulars of this work, it is important to delineate what we mean by "network parameters" and "network output." "Network parameters" are biophysical quantities intrinsic to a neuronal network that generally remain constant over the time scale of interest. They include both intrinsic cellular parameters, which are specific to each neuron, and network architecture, which describes the connections between neurons. Key cellular parameters include the maximal conductances of specific ion channel types in the membranes of single neurons. These values depend on the respective densities of those ion channels in the cell membrane and can vary widely between animals (Golowasch et al. 1999; Liu et al. 1998; Schulz et al. 2006). Key descriptors of network architecture include: which neurons connect to which (i.e. connectivity), the type of synapse (inhibitory or excitatory), and the synaptic strength, which is a function of the synapse's maximal conductance and can vary between animals (Goaillard et al. 2009). "Network output" refers to the characteristics of the electrical activity of a network. For the CPGs discussed here, characteristics of interest include cycle period, duty cycle (burst duration normalized by cycle period), and delay between the bursts of two neuron types.

1.5 High-dimensional model neuron databases as an approach to determining structure-output relationships

Traditionally, the effect of specific intrinsic membrane conductances in a single neuron

has been determined by manipulating these conductances one at a time and quantifying the resulting change in electrical activity (Golowasch et al. 1992; Guckenheimer et al. 1993; McCormick and Huguenard 1992). In biological neurons, this is accomplished by genetically altering the density of specific ion channels, by pharmacologically blocking subsets of channel types, or by mimicking these conductances with dynamic clamp. However, neuronal activity is collectively governed by all of a neuron's membrane conductances, and each conductance is variable from animal to animal in terms of magnitude (Golowasch et al. 1999; Schulz et al. 2006). Manipulating individual conductances one-by-one does not fully capture the effect of the full complement of conductances on the neuronal activity (Golowasch et al. 2002; Prinz et al. 2003a). Thus, modifying one conductance at a time may not have a consistent effect on cellular output from animal to animal because each neuron is most likely displaying a unique combination of conductances.

A similar problem exists when manipulating membrane conductances in Hodgkin-Huxley type model neurons (Marder and Abbott 1995). When developing a canonical model neuron, a modeler will typically choose specific values for all model parameters (including maximal conductances) that lie within a biologically realistic range. However, these ranges can be large, because maximal conductances in biological neurons vary widely between animals, even in the same cell type (Schulz et al. 2006). Within these ranges, the modeler must choose all conductance values for the model, then manipulate them one at a time to determine their effects on neuronal output. With this technique, one cannot immediately determine whether a failure to see an expected relationship between a particular conductance and neuronal output is due to a global absence of that relationship or is simply unachievable given the combination of conductances chosen for the model. Thus, varying one conductance at a time in an individual (biological or model) neuron provides a limited view of that conductance's role in controlling neuronal output (Prinz 2010; Prinz et al. 2003a).

One might think that it is reasonable to experimentally measure values for each maximal conductance in several animals, then use the average of those values to construct a canonical model neuron. In fact, a model constructed in this manner can fail to exhibit the activity of the biological neurons whose parameter values were used to generate it (Golowasch et al. 2002; Prinz 2010). Why don't the averaged values of the individual sets of membrane conductances produce output that is an "average" of each individual neuron's activity? Golowasch et al. (2002) demonstrated that this "failure of averaging" phenomenon can occur because the distribution of model neurons producing a particular type of activity - also referred to as the activity "solution space" - can be of a non-convex shape. In other words, the mean of the solution space may not lie within the solution space itself (Marder and Taylor 2011). Further studies (Achard and De Schutter 2006; Prinz et al. 2003a) have corroborated the idea that the solution spaces of complex model neurons are often highly complex, and predicting their shapes is not trivial.

From such studies, it becomes clear that a single "canonical" model neuron is not always sufficient to capture the effects of individual conductances on neuronal output. Recent studies have instead begun using a method known as *ensemble modeling* (Prinz et al. 2003a; Prinz et al. 2004b) which captures the variability of both the input parameters and the output measures of the model. Generally speaking, the ensemble modeling method involves simulating a large number of models over a range of values for every parameter of interest. Target ranges for the output measures of interest are then defined. Depending upon the application, these target ranges may be based on values that have been experimentally observed, or they may be arbitrarily chosen. The subset of models with output that falls within the chosen target ranges constitutes the solution space.

Given a set of input parameter ranges and target ranges for output measures, what is a good way to find a solution space? Figure 3 shows several example methods for mapping solution spaces (Prinz 2010). One method is to tune variables one at a time (Fig. 3A), starting from a single point in solution space. A second method is to run an

evolutionary algorithm several times, find one solution each time, then interpolate between them (Fig. 3B). Alternatively, one can perform simulations at random (Fig. 3C) or regularly spaced (Fig. 3D) points in parameter space. As is schematized in Figure 3, solution spaces can be concave and non-contiguous, which can explain why a model neuron built using the averages of experimentally measured parameter values often does not exhibit the expected activity type (Golowasch et al. 2002).

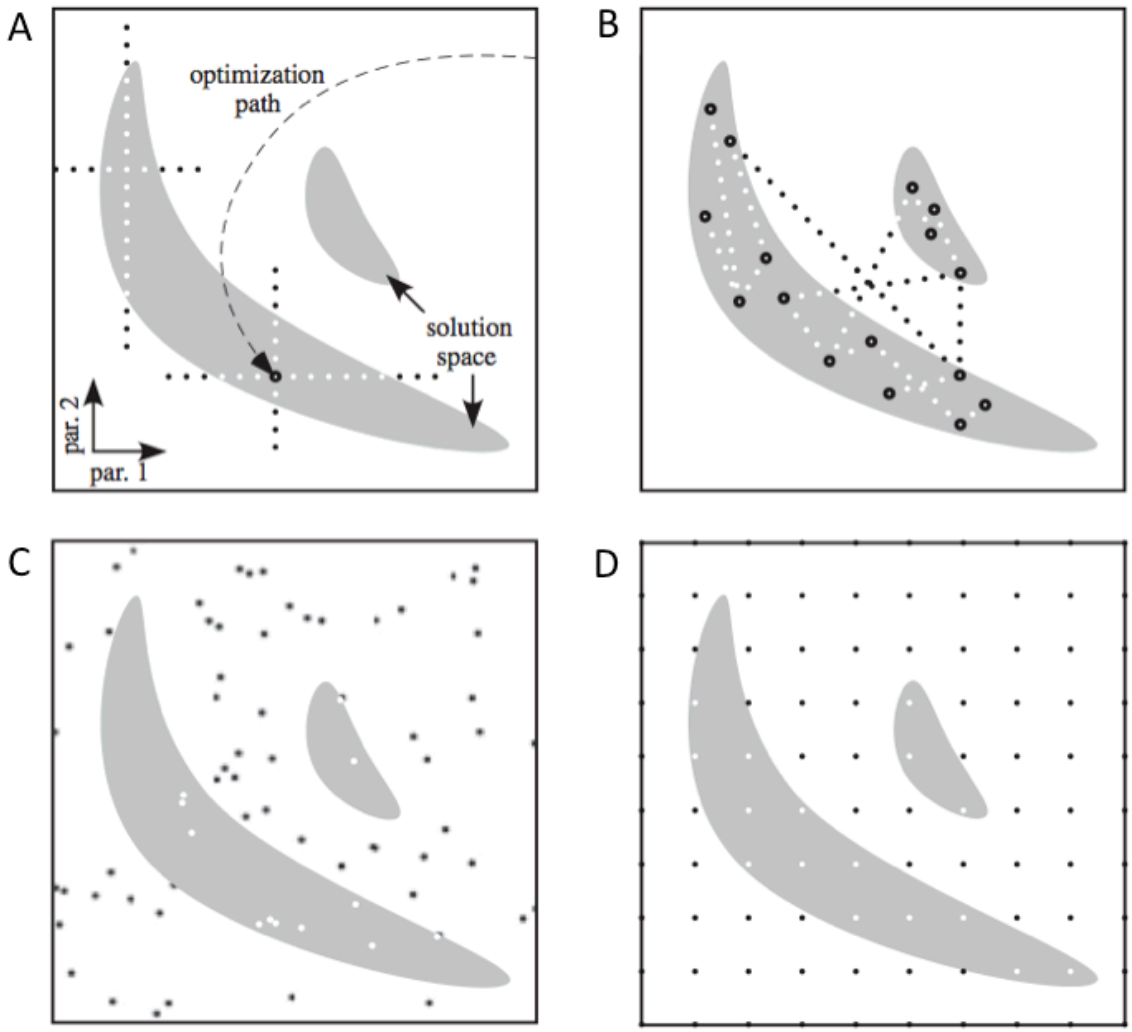

Figure 3. Example methods of mapping solution spaces within a two-dimensional parameter space. The white area represents two-dimensional parameter space, and the gray region represents the solution space. Simulated parameter sets are shown as dots, with white dots representing solutions and black dots representing non-solutions. (A) Parameter space is explored by varying one parameter at a time. (B) An evolutionary algorithm is run several times to find several results; hyperplanes are then created using subsets of these results and used to map the solution space. (C) A stochastic exploration

of parameter space. (D) An exploration of parameter space using regularly spaced parameter values. From (Calabrese and Prinz 2009; Prinz 2010).

Ensemble modeling has been used to quantitatively examine the relationship between intrinsic cellular parameters and cellular output. One such study (Prinz et al. 2003a) involved the development of a high-dimensional database of single-compartment conductance-based pacemaker model neurons. To create this database, eight maximal conductances in a conductance-based model neuron were independently varied over six regularly spaced values, from 0 mS/cm^2 to a specific maximum value. Ranges for each conductance were based upon experimental data (Turrigiano et al. 1995). For all 6^8, or 1,679,616, conductance combinations, the spontaneous activity of the conductance-based model neuron was simulated until it reached steady-state activity. This activity was then analyzed and classified by type (bursting, spiking, silent, and irregular). Input parameters and output measures (activity type, period, burst duration, duty cycle, and others) for each of the 1,679,616 model neurons were catalogued in a searchable database that is available online (Hudson and Prinz 2010; Prinz et al. 2003a).

Because the database described above includes information about both the intrinsic membrane parameters and the neuronal output, it can serve as a useful aid in exploring relationships between cellular parameters and electrical output in single neurons. Several studies have utilized this database to demonstrate that a wide variety of ion channel conductance combinations can result in similar types of output from the neuron (Hudson and Prinz 2010; Prinz et al. 2003a; Soofi et al. 2012).

While this database is useful for studying the relationship between intrinsic membrane conductances and output measures in a single pacemaker neuron, it does not provide information about how that neuron's output affects the activity of its neuronal network. How do the synaptic strengths between the neurons in a CPG affect the output? How do the intrinsic membrane conductances of the other neurons in the

network affect the output? How specific is the relationship between network structure and network output?

To answer these questions, parameter space exploration and ensemble modeling were used to develop a database containing over 20 million versions of a model of the pyloric CPG in the crustacean STNS pyloric circuit. To conduct the study, model neurons that matched the spontaneous firing patterns and rebound properties of the neurons in the crustacean pyloric circuit were chosen from the previously published database of STNS model neurons mentioned above (Prinz et al. 2003a). The strengths of the 7 inhibitory synapses in the circuit were varied through 5 or 6 different values that ranged from 0 nS synaptic conductance (corresponding to no synaptic connection) to 100 nS (which represents a synapse strong enough to clamp the postsynaptic neuron to the synaptic reversal potential). All ~20 million combinations of these model neurons and synapse strengths were simulated, stored in a network model database, and their activity was classified as functional if they produced a tri-phasic rhythmic burst pattern in the correct order (AB/PD-LP-PY) that fell within the biologically observed ranges for rhythm characteristics such as period, burst durations, duty cycles, delays, and phase relationships. Two percent of the simulated networks, approximately 450,000 networks, matched these highly constraining requirements and were thus considered functional pyloric network models. Examples of functional and non-functional network models are shown in Figure 4 (Prinz et al. 2004b).

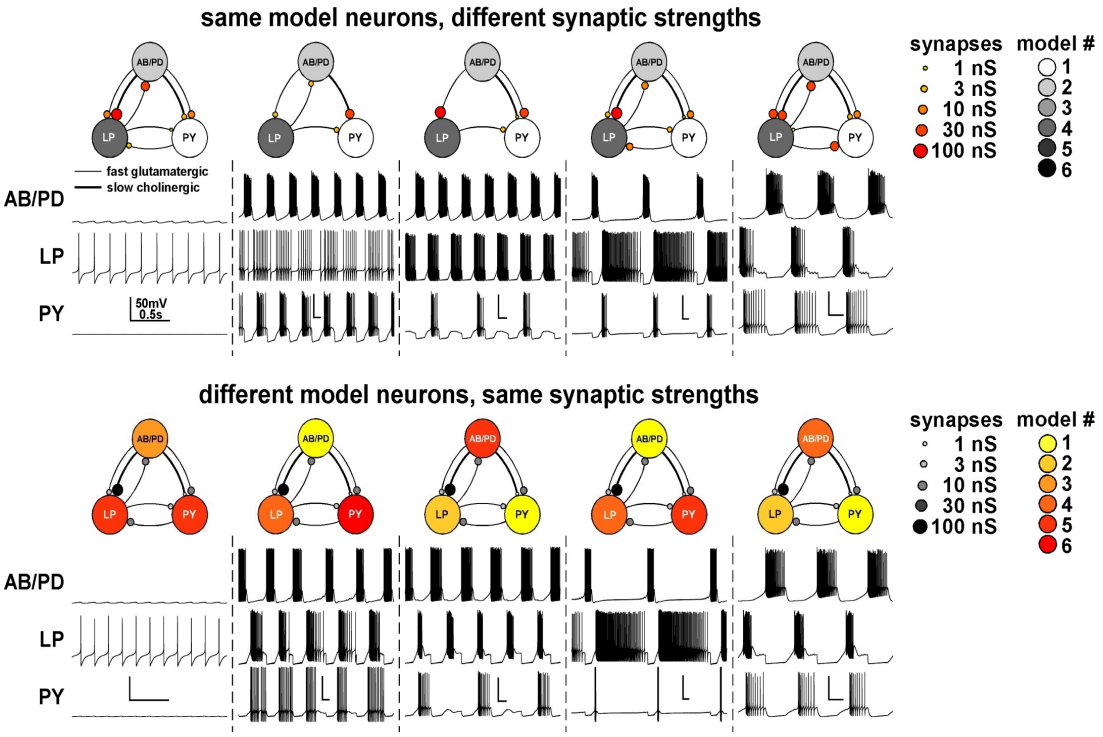

Figure 4. Ten examples from a database of 20 million network models generated by combining different model neurons and synapse strengths. For each network a schematic indicating its model neurons and synapse strengths and the simulated voltage traces for the AB/PD, LP, and PY neurons are shown. The top row shows network models with the same model neurons but different synaptic connections. The bottom row shows network models with the same synaptic connections but different model neurons. Only the two networks at the right end of the figure produce functional pyloric activity. Adapted by permission from Macmillan Publishers Ltd: *Nature Neuroscience* (Prinz et al. 2004b), Copyright 2004. Nature Publishing Group.

Comparison of the rightmost networks in the top and bottom row of Figure 4, which both generate functional network output, indicates that they do so with quite different synaptic connections. Indeed, all synapses in the network except for the LP-to-PY synapse were found to vary over the entire range from 0 nS to 100 nS within the functional network models (Prinz et al. 2004b), demonstrating that a tightly constrained network architecture is not necessary for proper pyloric network function. Furthermore,

over half (54%) of the functional network models included one or several synapses whose strength was 0 nS; i.e., these synapses were actually missing from the circuit. Strikingly, among these 54% functional network models with missing synapses were over 3,000 pyloric network models with the minimal connectivity of only synapses from the AB/PD pacemaker kernel to the LP and PY follower neurons, but no connections between the followers or back to the kernel.

Conversely, even the "best" network architecture, i.e. the particular combination of synapse strengths that generated functional output for the largest fraction (88 out of 150, or 59%) of model cell combinations, failed to do so for the remaining 41% of cell combinations. Even in a circuit in which the properties of the individual neurons are physiologically realistic and should be conducive to their role in the network, there thus appears to be *no* single network architecture that is sufficient to ensure proper network function under all circumstances.

The conceptual results from this modeling study, that a particular and stereotyped network architecture is neither *necessary* nor *sufficient* for the generation of biologically functional network output, is also supported by experimental data. In the STNS, the strength of chemical synapses between pairs of identified neurons exhibits several-fold variability from animal to animal (Goaillard et al. 2009).

1.6 Co-regulation of network parameters as a mechanism for output stability

As described in the previous sections, simple neuronal networks can achieve similar output despite variations in network architecture (Prinz et al. 2004b; Saideman et al. 2007) and intrinsic cellular parameters (Prinz et al. 2004b; Schulz et al. 2006). How does a neuronal network exhibit such consistent output in the face of variability in circuit parameters? Are there any rules that govern this variability? These questions can be partly answered by examining the shapes of the solution spaces in such computational studies as those just described (Prinz et al. 2003a; Prinz et al. 2004b).

One clear observation is that, while the shapes of solution spaces remain complex and often unpredictable, they are often contiguous in parameter space (Prinz et al. 2003a; Prinz et al. 2004b; Taylor et al. 2006). Another observation is that solution spaces are topographically organized; those solution spaces containing similar activity types are more likely to be adjacent to one another in parameter space. For example, the burst period of a model neuron generally varies smoothly across parameter space (Prinz 2010; Taylor et al. 2006). If one solution space is defined as having a target burst period of, say, 1 s to 1.2 s, then those model neurons that fall near, rather than inside, that solution space are likely to have burst periods that are near that solution space's target range. Topographical organization of solution spaces is also present at the network level (Grashow et al. 2010; Soto-Trevino et al. 2001). From the perspective of homeostatic regulation, this is a desirable situation. Small fluctuations in the maximal conductances of a biological neuron will not drastically change the activity of the neuron; the network activity is thus unlikely to be greatly affected.

A third observation is that certain cellular and synaptic parameters exhibit pairwise correlations within solution spaces (Ball et al. 2010; Hudson and Prinz 2010; Soofi et al. 2012). In other words, as one moves through parameter space by increasing one particular cellular parameter, then another cellular parameter would need to be increased (or decreased) in order to remain in the same solution space. At the single-neuron level, the co-regulation of certain ionic conductances within a model neuron is associated with maintaining specific parameters of electrical output, such as spike frequency, duty cycle (Hudson and Prinz 2010), and spike phase (Soofi et al. 2012); however, conductance correlations in functional model neurons are not always ubiquitous or strong (Taylor et al. 2009). At the network level, a pyloric network model is more likely to display proper pyloric rhythmicity when an increase in PD-to-LP synaptic strength is accompanied by a corresponding decrease in AB-to-LP synaptic strength (Prinz, unpublished data). This evidence suggests that while a wide variety of network parameter combinations may lead

to similar network output, these parameter values are subjected to a specific set of co-regulatory rules at the network level. It may be that following this set of rules, rather than having a specific set of parameter values, is key to maintaining reliable network output.

The computational studies described above provide a wide-ranging view of parameter effects on cellular and network output in models. However, we do not have a similarly comprehensive knowledge of the relationship between cellular and network parameters and output in biological circuits, since current techniques do not allow experimentalists to use high-dimensional brute-force methods such as those described above. By instead examining individual pairs of conductances, a number of experimental studies in the crustacean pyloric circuit have suggested pairwise conductance co-regulation as a mechanism for preserving consistent output. Experimentally increasing the mRNA copy number for the transient potassium (A-type) ion channel, for example, intrinsically increases the hyperpolarization-activated (H-type) current without substantial changes in overall cellular activity (MacLean et al. 2005; MacLean et al. 2003). In fact, a number of pairwise correlations between ion channel expression levels are found in identified pyloric neurons. Additionally, in the STG, different cell types have unique combinations of conductance correlations. Thus, cellular identity may be defined, in part, by unique mechanisms for transcriptional co-regulation of ion channel genes (O'Leary et al. 2013; Schulz et al. 2006; Schulz et al. 2007; Temporal et al. 2012; Tobin et al. 2009).

So far, we have described the presence of correlations among intrinsic parameters of single neurons. Have any such correlations been observed at the network level? There is evidence that the AB neuron-to-LP neuron synaptic strength and the PD neuron-to-LP neuron synaptic strength are negatively correlated with one another, so that the total strength of the synapse from the AB/PD pacemaker kernel onto LP is relatively constant (Goaillard et al. 2009). This result corroborates the findings from the network database.

Ensemble modeling is a highly useful method for understanding the relationship between network architecture and network output. Results from computational studies indicate that: (1) specific network architectures are neither necessary nor sufficient for functional output and (2) network parameters may follow co-regulatory "rules" in order to maintain network activity. These findings suggest that CPG output is more tightly regulated than the intrinsic cellular or synaptic parameters of the system. Since neural systems must be able to produce reliable output throughout the lifetime of an animal despite constant molecular turnover and environmental changes, it is reasonable to assume that the compensatory mechanisms discussed here are a means of stabilizing output and preventing sudden, possibly adverse effects to the network as a whole.

1.7 Manipulating neurons with dynamic clamp

The ability to model voltage-dependent currents with Hodgkin-Huxley-type equations has also resulted in another innovation – the ability to introduce realistic, artificial synaptic or intrinsic membrane currents into a living neuron in real time. This technique – known as dynamic clamp (Sharp et al. 1993a; b) – has become a standard electrophysiology tool (Prinz et al. 2004a). Unlike voltage clamp or current clamp, dynamic clamp effectively adds or subtracts conductances to the neuron by following the Hodgkin-Huxley-type equation, $I_i = \bar{g}_i m_i^p h_i (V_m - E_i)$ for each conductance g_i. The method is performed as follows: At each time step (50 microseconds or less), the membrane voltage of the neuron, V_m, is recorded, and the reversal potential, E_i, of current i is subtracted from V_m to obtain the driving force. Then, this is multiplied by the given maximal conductance value g_i, the voltage-dependent activation variable m_i^p and in the case of inactivating currents, the inactivation variable h_i, to calculate a current I_i, which is then rapidly injected. This current value is updated and injected at each time step. The dynamic clamp technique is useful for creating hybrid circuits of artificial and biological neurons, as well as for adding individual synaptic or membrane currents into an isolated

neuron (Prinz et al. 2004a).

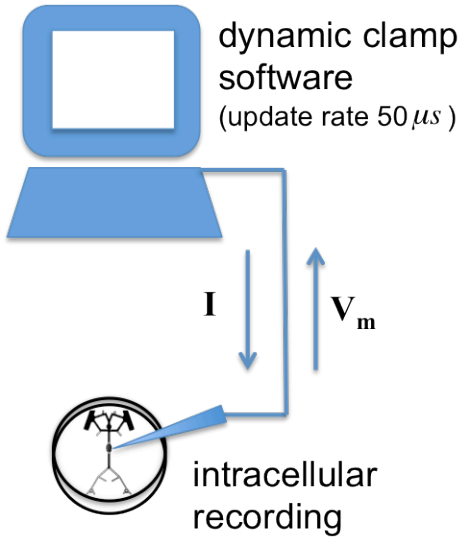

Figure 5. Simplified schematic diagram of dynamic clamp technique. At each time step, the membrane voltage (V_m) is recorded from a neuron (in this case, an STG neuron), and is used to compute the necessary current to be injected to produce a desired conductance value. To reproduce rapidly activating and inactivating currents, such as I_{Na}, the time step of the real time software must be quite small; 50 microseconds or smaller is ideal if fast conductances, such as those associated with the fast Na^+ current, are being simulated.

1.8 Temperature sensitivity of neuronal circuits

So far, we have discussed the roles of certain ionic currents in regulating activity of small neuronal networks. It is also important to consider the nature of the perturbations that might cause changes in rhythmic activity. The ability of a neuronal circuit to maintain reliable, rhythmic activity is made all the more difficult by a constantly changing environment. One challenge that is faced by the nervous systems of cold-blooded animals, such as decapod crustaceans, is to cope with constant changes in ambient temperature. Certain animals, such as *Cancer borealis* and its close relative *Cancer pagurus,* must handle changes in temperature of several degrees Celsius within the course of a single day. The many subcellular components of nervous systems, such as ion

channels, often have widely varying temperature dependencies; it is therefore not a trivial task for a nervous system to function properly at a wide range of temperatures. Many neuronal circuits exhibit a rate increase in output with increasing temperature (Robertson and Money 2012). In fact, when exposed to temperatures that increase from 7°C to 23°C *in vitro*, the pyloric rhythm frequency increases approximately four-fold. However, the phases of the neuron bursts that define the rhythm itself are remarkably well preserved (Tang et al. 2010) (Figure 6). This maintenance of activity may result from biological restrictions on the Q_{10} values of various subcellular components of the system. It is of interest to us to determine whether such stringent preservation of activity is present not only *in vitro*, but in the natural environment of the intact animal.

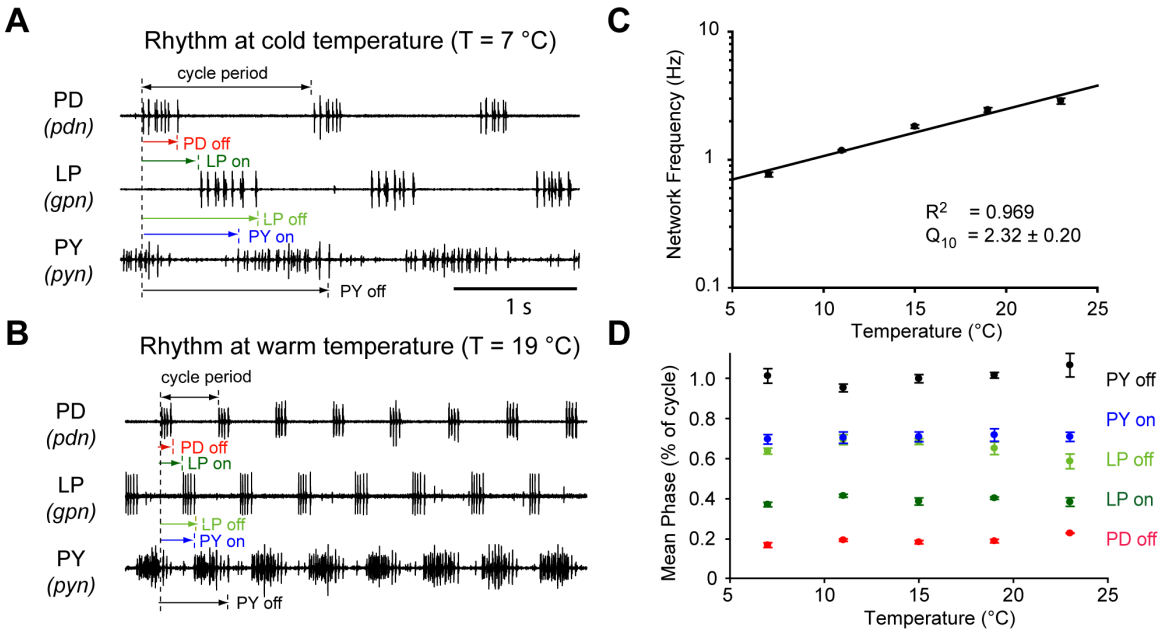

Figure 6. Quantification of pyloric network output at different temperatures. (A) Example extracellular nerve recordings of the pyloric rhythm at cold temperature (T = 7°C). The onset and offset delay of each neuron relative to the onset of PD neuron burst are indicated. Horizontal scale bar, 1 s, for both (A) and (B). (B) Example extracellular nerve recordings from the same preparation as in (A) but at warm temperature (T = 19°C). The same delay measurements are indicated as in (A). (C) The frequency of the pyloric rhythm plotted as a function of temperature from T = 7°C to T = 23°C (n = 7). (D) The mean phase (delay divided by cycle period) values of the pyloric rhythm plotted

as a function of temperature from T = 7°C to T=23°C (n=7). Figure and caption reprinted from (Tang et al. 2010), originally distributed under the terms of the Creative Commons Attribution license.

1.9 Thesis Organization

In this work, I describe the motivation, design, implementation, analysis, and implications of three studies that investigate the regulation of single-neuron and network activity in the stomatogastric ganglion of the decapod crustacean. The remainder of this thesis is organized as follows:

In **Chapter 2**, I describe the observation of spike phase maintenance in a pacemaker neuron, then explore whether the co-regulation of ionic conductances may underlie this phenomenon via analysis of a high-dimensional single-compartment model neuron database.

In **Chapter 3**, I determine the effects of specific ionic conductances on the response of model neurons to synaptic input. I do this by analyzing the Phase Resetting Curve (PRC) of single-compartment and multi-compartment models. I also examine the effects of these conductances on the PRC in a biological neuron via dynamic clamp injection or pharmacological blockade of specific ionic currents in the PD neuron of the pyloric circuit.

In **Chapter 4**, I examine the effect of changes in ambient temperature on the frequency and phases of the pyloric rhythm in the intact, behaving crustacean.

In **Chapter 5,** I summarize this work and consider the future roles that small invertebrate neuronal networks may play in understanding structure-function relationships in complex nervous systems.

CHAPTER 2

CO-VARIATION OF IONIC CONDUCTANCES SUPPORTS PHASE MAINTENANCE IN STOMATOGASTRIC NEURONS

This chapter was published in full as a peer-reviewed research article in the *Journal of Computational Neuroscience* (Springer). Citation: Wafa Soofi, Santiago Archila, and Astrid A. Prinz. "Co-variation of ionic conductances supports phase maintenance in stomatogastric neurons." *Journal of Computational Neuroscience* 33.1 (2012): 77-95. With kind permission from Springer Science and Business Media.

2.1 Introduction

Neural central pattern generating circuits are able to maintain consistent rhythmic activity throughout the lifetime of the animal. To retain network functionality, each neuron must preserve its unique electrical role within the network. This role is partially governed by each cell's set of membrane currents (Levitan 1988), which must be constantly regulated in order to maintain a consistent electrical identity. This identity is preserved even as the proteins that compose the membrane ion channels undergo turnover (LeMasson et al. 1993). The mechanism by which neurons regulate their membrane currents to maintain network function is, as of yet, not entirely understood.

The pyloric pattern-generating circuit of the stomatogastric nervous system (STNS) in crustaceans is one of the best-characterized oscillatory neural networks (Marder 1997; Selverston 2010; Selverston and Moulins 1985). The pyloric circuit innervates muscles that control the region of the stomach known as the pylorus. It produces a triphasic motor pattern that consists of a burst of action potentials from the pyloric dilator (PD) neurons, followed by a burst from the lateral pyloric (LP) neuron, then by a burst from the pyloric (PY) neurons. The stomatogastric ganglion (STG) contains a small number of neurons that are consistently identifiable across animals, and it produces reliable,

rhythmic electrical activity for up to several days or weeks *in vitro*. This system has been used in network-level and single-cell studies of homeostatic regulation (Marder and Bucher 2007). Several studies have shown that neuronal activity is governed in part by the maximal conductances (henceforth referred to simply as "conductances") of specific ion channel types, but the manner in which they do so is highly nonlinear. In certain instances, a small change in one conductance results in a large change in electrical activity (Goldman et al. 2001). Conversely, many different sets of ionic conductances can result in similar neural activity (Achard and De Schutter 2006; Prinz et al. 2004b; Schulz et al. 2006; Swensen and Bean 2003; 2005). Of particular interest is the role of correlations between sets of ionic conductances (Khorkova and Golowasch 2007) and ion channel mRNA levels (Tobin et al. 2009) in preserving neural activity. Overexpression of the transient potassium current (I_A) in lobster STG neurons elicits an increase in the hyperpolarization-activated mixed-ion current (I_h), with minimal changes in electrical activity (MacLean et al. 2005; MacLean et al. 2003), suggesting that a neuron can actively modify its membrane properties in order to regulate its electrical output. Computational studies scanning the conductance space of model neurons have also found that pairwise co-regulation of conductances can preserve certain aspects of neural activity (Ball et al. 2010; Hudson and Prinz 2010). The presence of these correlations suggests that the neuron is following a set of biological "rules" which are necessary for it to maintain a homeostatic equilibrium.

Much of the work on the pyloric circuit has focused on the relationships between bursts in the various neurons in the network. Previous studies have shown that pyloric burst phases are relatively invariant over time (Hooper 1997a; 1997b), suggesting that the burst phase holds some functional importance to the pyloric rhythm. The mechanism by which the neuron accomplishes burst phase maintenance has not been resolved. Relatively little work has been done to elucidate the role of intra-burst spike patterns. It was originally believed that the spike timing within a burst played a less critical role than

the timing of slow-wave oscillations in governing network activity (Graubard 1978; Raper 1979). However, recent studies have suggested that certain intra-burst properties, such as spike frequency and the number of spikes per burst, have significant effects on muscle response (Hooper and Weaver 2000; Morris and Hooper 1997; Morris et al. 2000). Other experiments have demonstrated the presence of synaptic modulation of precise spike patterns within bursts (Brochini et al. 2011; Szucs et al. 2003), and these spike patterns may have some functional significance. Furthermore, modeling studies have suggested that network responses are sensitive to these spike patterns (Latorre et al. 2006).

In this work, the relationship between spike delay and period was quantified in the crab STG. We observed that spike delays within pyloric bursts can vary proportionally with period, so that the phases of the spikes, relative to the beginning of the burst, are invariant to the period. We hypothesized that pairwise conductance correlations may be associated with this maintenance of spike phase. To test this hypothesis, two separate computational studies were performed. The first study altered the conductances of a "canonical" burster, two at a time, to determine the effects on that burster's activity. We refer to this as the "single-burster" study. An advantage to varying only two conductances at a time is that a large number of simulations can be run in two-dimensional conductance space, providing us with a high-resolution view of the pairwise relationships. A disadvantage to this approach is that the results involve modulating the parameters of a single, arbitrarily chosen burster; they thus do not constitute a comprehensive view of how spike phase is maintained in the eight-dimensional conductance space of the model neuron. The second study provides a view of this conductance space by using a model neuron database, in which all eight conductances are allowed to vary freely, to develop populations of bursters with low spike phase differences relative to one another. These populations' conductance distributions were examined over all 28 pairwise combinations of the eight conductances. We refer to this as

the "population" study. The first study asks, "If six of eight of a model neuron's conductances are constrained, can the neuron preserve its activity by co-modulating the other two conductances?" The second study asks an inverse question: "If we extract from a database a population of model neurons constrained to a specific type of activity, do the pairwise distributions of their conductances suggest that the co-modulation of certain conductance pairs is needed to preserve their activity type?" The two studies complement each other, and we found that certain conductance correlations were evident in both approaches.

2.2 Methods

2.2.1 Experimental studies

Jonah crabs (*Cancer borealis*) were purchased from commercial suppliers and stored in a cold-water artificial seawater tank at ~12^{O}C. Crab saline (11 mM KCl, 440 mM NaCl, 13 mM $CaCl_2 \cdot 2H_2O$, 26 mM $MgCl_2 \cdot 6H_2O$, 11.2 mM Trizma base, 5.1 mM maleic acid, pH 7.45 ± 0.03) was refrigerated until needed.

2.2.1.1 Preparation

The animal was cold-anesthetized for 20-30 minutes by submerging it in ice prior to dissection. The stomach, which includes the STNS, was removed from the animal, pinned into a deep Sylgard-lined dish, and submerged in chilled (10-15^{O}C) saline. The STNS, including the STG and the nerves that innervate the stomach muscles, was dissected out of the stomach and pinned in fresh saline in a Sylgard-lined Petri dish. The preparation was transferred to an electrophysiology rig where fresh saline was chilled with a Peltier thermoelectric cooler and superfused over the nervous system.

2.2.1.2 Electrophysiology

Vaseline wells were built around the lateral ventricular nerve (*lvn*, which contains axons from PD, LP, and PY neurons) on each side, and a stainless steel wire electrode was

placed in each well to make extracellular nerve recordings of network activity. The extracellular recording provides a convenient measure of the network cycle frequency as well as the LP neuron inter-spike intervals without having to impale multiple cells. An A-M Systems Model 1700 Differential AC Amplifier was used for extracellular recordings, and all free-running rhythm data was acquired with an Axon Instruments Digidata 1322A and pClamp 9.2 software (Molecular Devices).

2.2.2 Modeling studies

2.2.2.1 Simulation

The single-compartment conductance-based stomatogastric model neuron that was utilized to simulate neural bursting activity has been previously described (Prinz et al. 2003a). This model consists of a set of eight Hodgkin-Huxley-type ionic currents, each specified by one or two differential equations that describe voltage-dependent channel activation and inactivation. During each individual simulation, all model parameters were kept constant. The parameters in this study included eight conductance values which were taken from a model neuron database that has also been previously described (Prinz et al. 2003a). The voltage dependence and temporal dynamics for seven of these conductances were based upon *in vitro* experiments on unidentified stomatogastric cells in culture (Turrigiano et al. 1995). These conductances were: fast sodium (g_{Na}), fast transient calcium (g_{CaT}), slow transient calcium (g_{CaS}), transient potassium (g_A), calcium-dependent potassium (g_{KCa}), delayed-rectifier potassium (g_{Kd}), and a voltage-independent leak conductance (g_{leak}). Values for the eighth conductance, a hyperpolarization-activated mixed-ion inward conductance (g_H), were derived from studies on guinea pig lateral geniculate relay neurons (Huguenard and McCormick 1992).

All simulations and analysis were performed in MATLAB. Simulations were run for 20 seconds with a time step of 0.05 ms. Both the membrane voltage and the intracellular calcium concentrations were updated at each time step using the exponential method

detailed in (Dayan and Abbott 2001). Activation and inactivation variables were updated using the Euler method. Spike times were recorded at each time that the voltage made a negative-to-positive crossing over 0 mV. These spike times were then used to find which of the model neurons were stable bursters. Inter-spike intervals (ISIs) that were greater than five times the length of the previous ISI were deemed inter-burst intervals (IBIs), and the activity between the start times of two consecutive IBIs was deemed a burst cycle. After varying the threshold for classifying an ISI as an IBI between two to six times the previous ISI, we found that our chosen value of five-fold for this threshold was suitable for the present analysis. If the corresponding ISIs within each of the last three complete burst cycles differed by less than 10% from their mean, the model neuron was classified as a stable burster. Since our aim was to examine intraburst spike phase maintenance, only neurons that had reached a stable bursting pattern by the end of the simulation time were analyzed. If no IBIs were detected, according to the above criteria, the model neuron was assumed not to be a stable burster and, therefore, not to have definable intraburst spike phases. These model neurons (including silent neurons and tonic spikers) were excluded from the analysis. All regularly bursting model neurons reached stable activity well before the end of the simulation time.

2.2.2.2 Quantifying phase difference

To determine the effect of individually varying conductances on spike phase in the single-burster study, a "canonical" burster was first chosen, with maximal conductances shown in Table 3. This burster demonstrated steady bursting activity and a period of 0.98 seconds, similar to that of the pyloric rhythm typically seen *in vitro* (Marder and Bucher 2007). We then compared the spiking activity of the canonical burster to that of a "modified" burster in which one or two of the conductances were varied from the canonical value. A simple metric was used to quantify the spike phase difference between the canonical and modified bursting model neurons. If we let t_i^j denote the time

of the *j*th spike in a regular burst from model *i* (spike s_i^j), where each model *i*'s burst cycle has a period of p_i, the spike phase H_i^j of s_i^j is then defined as:

$$H_i^j = \frac{t_i^j - t_i^1}{p_i}$$

To allow spike phase comparison between models with different numbers of spikes per burst, this metric was only calculated for the first *N* spikes, where *N* denotes the lowest number of spikes between the canonical and altered bursters. The average phase difference D_i between the canonical burster and each of the altered bursters is then calculated by summing the phase differences and dividing by *N*-1:

$$D_i = \frac{1}{N-1}\sum_{j=1}^{N-1}\left|H_i^j - H_c^j\right|$$

where H_c^j is the spike phase for spike *j* of the canonical burster *c*. Thus, the metric D_i may be thought of as the "average phase difference per spike" relative to a canonical burster. We note that this metric ignores all spikes beyond the *N*th spike. Quantifying differences in spike phase for bursters with different numbers of spikes is not trivial (Lago-Fernandez 2007). Here, we are choosing to only examine those spikes that are common to both bursters. Fig. 7 illustrates the phase maintenance metric for pairs of model neurons with varying degrees of average spike phase difference. For the purposes of our computational studies, we deem any pair of model neurons with an average spike phase difference of less than 0.01 to be exhibiting high phase maintenance.

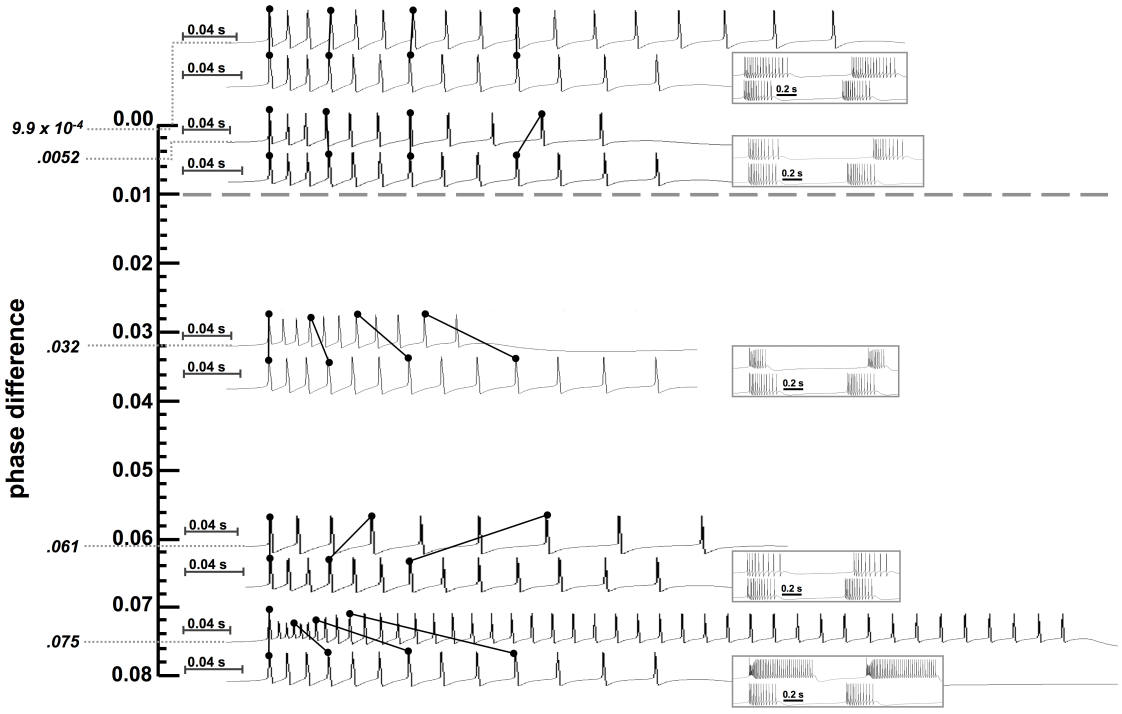

Figure 7. Five pairs of model neuron voltage traces demonstrating progressively greater phase differences. Voltage traces were normalized by each of their respective periods; thus, the first spike of each burst is aligned. Time scale bars are shown to the left of each trace. The lower trace in each pair represents one burst from the canonical model neuron. The upper trace represents one burst from a model for which two conductances were varied from their canonical values. The black lines drawn between action potential peaks in the upper and lower traces show the divergence in phase between the first, fourth, seventh, and tenth spikes of each burster. The more vertical these lines are, the greater the maintenance of phase is between the two bursters. Traces in the insets have not been normalized by period to demonstrate the differences in the periods between the original and canonical bursters. Those pairs of model neurons with a phase difference of less than 0.01 were considered to have a high level of phase maintenance

2.2.2.3 Data structure and statistical analysis: single-burster study

For a set of eight conductances, the number of distinct two-element subsets is given by the binomial coefficient $\binom{8}{2}$, which is equivalent to 28 possible conductance pairs. To study the effects of pairwise conductance variation on spike phase, the conductance

values were independently varied, two at a time, by multiplying the canonical value by a set of multiplicative factors ranging from 0 to 3 in increments of 0.1 (see Table 3). This resulted in 31 x 31, or 961, combinations of values for each of the 28 conductance pairs. The average phase difference D_i per spike between each modified burster and the canonical burster was calculated. For each of these pairs of the eight conductances, two-dimensional color-coded graphs were generated by plotting the average spike phase difference versus the two conductance values. The degree of correlation between each of the two conductance pairs was quantified by identifying the subset of burster models within the 31 x 31 grid that exhibited a difference in phase from the canonical burster of 0.01 or less. The conductance values for those burster models that satisfied this condition were then examined for correlations using the nonparametric Spearman's rank correlation coefficient. Due to the gridlike structure of the data, using significance testing alone carries the risk of overestimating the degree of correlation. We thus define as correlated those relationships with a Spearman's rank correlation coefficient of $|\rho| \geq 0.4$ and a p-value of less than 0.05. Since our study focuses solely on examining putative monotonic relationships between conductances, we chose to perform a piecewise examination of any nonmonotonic relationships that were seen. The data was divided into approximately monotonic sections via visual inspection. We note that our method of defining the sets of bursters with high phase maintenance only considers whether $|\rho|$ is above or below the threshold; the absolute difference between the ρ value and the threshold is disregarded. However, by examining which correlations persisted as the threshold was lowered (providing a more stringent criterion for spike phase maintenance), we saw that a higher $|\rho|$ generally indicates more tightly maintained spike phases (data not shown).

2.2.2.4 Model neuron database

Co-varying pairs of conductances while constraining all others provides a systematic way to examine the effects of ionic currents on model neuron behavior, but only in a very

localized region of conductance space. Another, more comprehensive method of examining the influence of conductance on model neuron output is through the use of a large database of model neurons, wherein all eight conductances are independently and systematically varied. Each of the model neurons in the database can then be classified based upon various features of their electrical activity, and the underlying conductances of those neuron populations that satisfy a given set of criteria (for example, bursters with a cycle period between 1 and 1.1 seconds) can then be examined for trends. A previously existing large model neuron database was utilized to determine whether a population of model neurons with independently varied conductance values that was constrained to regular bursters with tightly maintained spike phases would exhibit pairwise conductance correlations (Prinz et al. 2003a). This database was constructed by simulating the spontaneous activity of the single-compartment conductance-based model neuron described above for six equally spaced, independently varied values of eight conductances. This resulted in 6^8, or 1,679,616, total model neurons. A variety of intrinsic activities were represented in this database, including regular and irregular spiking activity, regular and irregular bursting activity, and silence (no activity). Only those model neurons classified as regular bursters (712,613 model neurons in all) were analyzed in this study. Comparing the spike phases of neurons that burst only a few times per cycle nearly always results in a very low difference in spike phase. To avoid the possible confounding effect of low spike numbers on our results, we restricted the bursters analyzed to those with more than 4 spikes per burst.

2.2.2.5 Selecting model neuron populations with high and low levels of phase maintenance

From the regular bursters in the database, we selected several populations of model neurons with high phase maintenance, such that the neurons within each population had similar spike phases relative to the other neurons within the same population. To collect these populations, we constrained the duty cycle (defined as the fraction of the cycle

period during which the neuron is bursting) of the model neurons to a narrow range, then restricted the number of spikes per burst to a specific value. The duty cycle is equivalent to the phase of the last spike in the burst. Because the ISIs in these bursting models generally do not exhibit large amounts of variability from model to model, constraining the phase of the last spike also constrains the phases of the other spikes in the burst. Thus, by constraining duty cycle and spike number, we obtained populations of model neurons with low phase differences relative to one another. The width of the duty cycle range is equivalent to the maximum difference that any two bursters in the population may have in the spike phase of the last spikes in their respective bursts. Thus, the average phase difference per spike within these populations is well below the width of the duty cycle range. The phases are therefore, by our definition, highly maintained in these populations; we consider them a suitable model of phase maintenance in bursting neurons. Fig. 8(a) shows a sample "high phase maintenance" population of 500 bursters with duty cycles constrained between 0.06 and 0.07 and spike number constrained to 6. As a control, we also selected an analogous set of model neuron populations with low phase maintenance by constraining the period and the number of spikes per burst, but allowing the duty cycle to vary freely. A sample "low phase maintenance" population is shown in Fig. 8(b), with the period constrained between 0.70 and 0.74 seconds and the number of spikes per burst again constrained to 6. The variation of spike phase values in the sample "low" phase maintenance group is three- to fifteen-fold greater than in the "high" phase maintenance group, showing that their spike phase characteristics are quantifiably separable. We then statistically analyzed the "low" and "high" phase maintenance populations for the presence of conductance correlations.

To determine whether any present correlations were an effect of constraining either the duty cycle or the spike number alone, we further selected populations of regular bursters in which either the duty cycle or the number of spikes per burst was constrained, but not both at once. The conductance correlations for all three population types (those

with constrained duty cycle, constrained spike number, and constrained duty cycle and spike number) were statistically analyzed and compared.

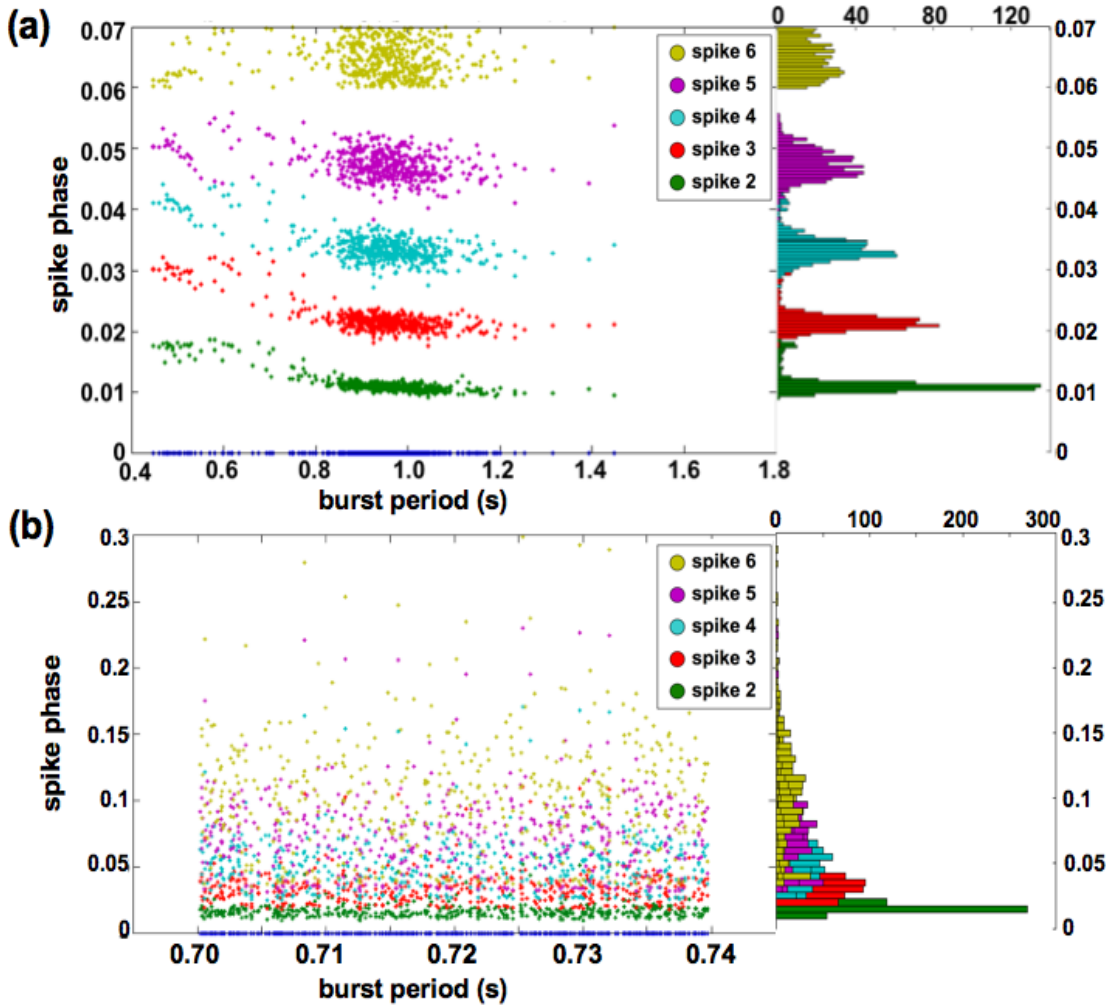

Figure 8. Comparison of burster populations with high and low phase maintenance. **(a)** Spike phase vs. period for 500 randomly chosen bursters with 6 spikes per burst and duty cycles between 0.06 and 0.07. The period is unconstrained. Histograms (right side of plot) illustrate the spread of the spike phases. The narrow distributions indicate that this population exhibits high phase maintenance. **(b)** Spike phase vs. period for 500 bursters with 6 spikes per burst and periods between 0.70 and 0.74 seconds. The duty cycle is unconstrained. A wide distribution of spike phases indicates that this burster population exhibits low phase maintenance

2.2.2.6 Data structure and statistical analysis: population study

To check for the presence of pairwise conductance correlations, we collapsed the neuron

populations down from an eight-dimensional parameter space into each of the 28 possible sets of two-dimensional space. Each of these two-dimensional distributions was then evaluated for correlations. We statistically quantified the strength of the conductance correlations in each burster subplot. One cannot assume that the model neuron output is obeying a theoretical underlying distribution, since this output has been artificially constrained. We therefore used nonparametric statistical tests as performed by (Hudson and Prinz 2010). For both "high phase maintenance" and "low phase maintenance" populations, conductance pairs were deemed correlated if they met the criterion of Spearman's $|\rho| \geq 0.4$, with a p-value < 0.05. We further used the nonparametric Wilcoxon rank-sum test to determine whether the sets of correlation coefficients for the two sets of model neuron populations were significantly different ($p < 0.05$). For the study comparing neuron populations with constrained duty cycle and number of spikes per burst ("high phase maintenance" populations) to the populations in which only the spike number or duty cycle was constrained, two nonparametric tests, the chi-squared test of independence and the Spearman's rank correlation test, were used to determine the presence of correlations between the various pairs of conductances. Correlations were deemed present if the chi-squared statistic met the criterion of $X^2 \geq 70$ and Spearman's rank correlation coefficient met the criterion of $|\rho| \geq 0.30$. The threshold values were chosen by examining the X^2 and Spearman's ρ values for difference matrices containing visually detectable correlations. These thresholds were then universally used to test all sets of neuron populations for the presence of correlations (Hudson and Prinz 2010).

2.3 Results

2.3.1 Experimental study

We analyzed six long term recordings of the lateral pyloric (LP) neuron in the pyloric network of *Cancer borealis*. In approximately half of these recordings, the ISI varied proportionally with the burst period over time, so that spike phases were maintained. A

sample preparation demonstrating this phenomenon is shown in Fig. 9(a). We plotted the delay of spikes 2-6 (relative to spike 1 of each burst) against the burst period and found a significant positive slope for all fitted trendlines (Fig. 9(b)). To quantify how close the observed spike phases were to being "perfectly" maintained, we adapted a previously described technique (Hooper 1997a). If a bursting neuron exhibits perfect spike phase maintenance, then as the burst period approaches zero, the phases of the spikes in a burst will also approach zero. Thus, plotting the spike delay relative to the beginning of the burst against the present burst period should result in a linear trendline with a positive slope and a y-intercept at (0,0). The second point that defines this "perfect delay" line must lie on the trendline that is fitted to the observed data. For each of the six preparations examined, we chose this point to be at the mean burst period for that preparation. The slope of the observed spike delay vs. period trendline for any bursting neuron should fall somewhere between zero (signifying a complete lack of phase maintenance) and the slope of the perfect delay line. A comparison of the average slope of the spike delay-burst period plot for a given neuron with the slope of perfect delay line therefore indicates the degree of phase maintenance that the neuron exhibits. For the sample experimental recording shown in Fig. 9, ratios of the slopes for the average spike delay/period trendlines to the slopes for the lines indicating perfect phase maintenance range between 0.70 and 0.76, indicating a relatively high degree of phase maintenance (Fig. 9(c)). The independence of spike phase from the period is illustrated by the horizontal trendlines in Fig. 9(d). Five other preparations were similarly examined. Of these, one exhibited ratios ranging between 0.30 and 0.51, and the other exhibited ratios between 0.73 and 1.08. Thus, three of the six preparations we examined demonstrated some degree of phase maintenance, two of them at a high and one at a moderate level. The remaining three preparations exhibited ratios near or below 0, suggesting that no phase maintenance was present.

Our metric for phase maintenance does not explicitly account for changes in period; it

therefore cannot differentiate between phases that have been maintained despite large changes in period and phases that are maintained simply because other aspects of the bursting activity (period, burst duration) have been maintained, as well. For each of the preparations, we compared both the standard deviation of the periods and the percent difference between the minimum and maximum periods to the degree of phase maintenance. No relationship was detected between the amount of variation of the period (using either metric) and the degree of phase maintenance, suggesting that the presence of phase maintenance is not due to a lack of change in the period.

To determine how well the spike phases are maintained within a single preparation over time, we calculated the difference between the phase of each spike in each burst and the mean phase of that spike for all bursts in the data set shown in Fig. 9. We then averaged each burst's spike phase differences, resulting in one average phase difference for each burst in the data set. The distribution of these average spike phase differences are shown in Fig. 9(e). The mean of the average spike phase difference for each burst is 0.0064 (red dashed line). We chose to use a similar value (0.01) to define our lower limit of spike phase maintenance in the modeling studies.

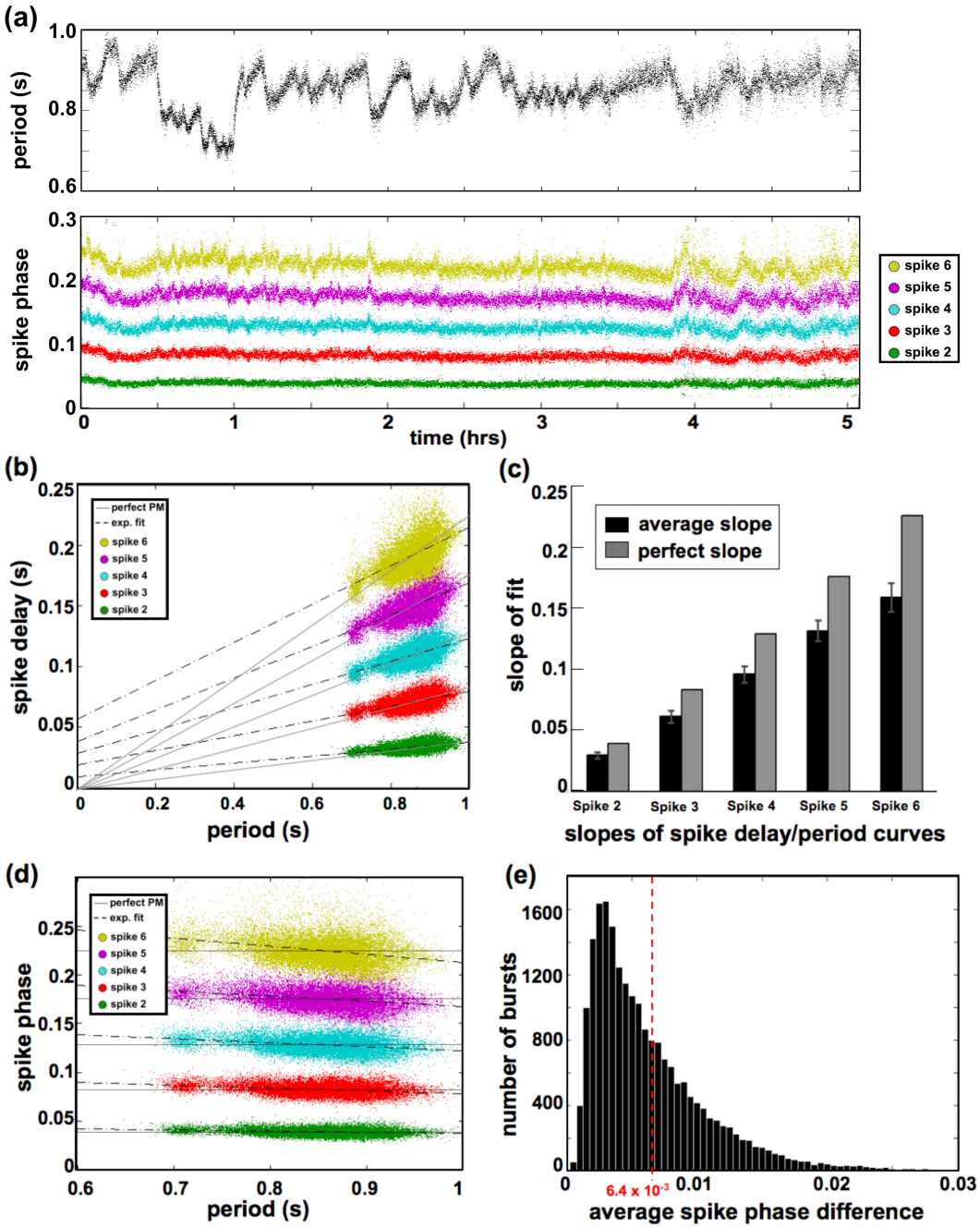

Figure 9. Experimental data demonstrating that as period varies, spike phases can be well maintained. The pyloric rhythm from an *in vitro* preparation was recorded for approximately five hours. **(a)** Period and spike phases for each burst are shown for the duration of the recording **(b)** Raw data and linear fits of the delay for spikes 2-6 of each burst versus the cycle period. Each data point represents one spike. Dashed black lines ("exp. fit") indicate linear fits to the experimental data. Lines indicating perfect phase maintenance ("perfect PM") are shown in light grey. All fits have a significant positive slope. The plot is scaled to indicate the y-intercepts for each trendline. Perfect phase maintenance would correspond to lines with a y-intercept at (0,0). **(c)** The ratio of the

average slope to the slope of the line indicating perfect phase maintenance ranged between 0.70 and 0.76 for spikes 2-6 in each burst. The first spike of each burst was not analyzed because its delay was defined as 0 s. **(d)** Spike phase was close to independent of the pyloric period. **(e)** Histogram showing the distribution of the average difference of the spike phases of each burst from the mean spike phases for the entire data set. The mean spike phase difference is 0.0064 (shown as dashed red line)

2.3.2 Single-burster study

In the twenty-eight pairs of conductances in the single-burster study, different types of qualitative relationships were seen: monotonic, non-monotonic, and independent relationships. Fig. 10(a) depicts the degree of phase difference for each of the 28 pairs of conductances, when both conductances in the pair are varied. Table 4 shows the Spearman's ρ and p-values for every pairwise correlation. The correlations for each conductance pair are summarized in Fig. 10(b). According to our criteria ($|\rho| \geq 0.4$, $p < 0.05$), six conductance pairs had monotonic relationships that were correlated across the entire data set, and seven had non-monotonic relationships that exhibited at least one correlation when examined in a piecewise fashion. Of the monotonic relationships, five conductance pairs were positively correlated in model neuron populations exhibiting phase maintenance, and one was negatively correlated. Of the nonmonotonic relationships that were examined piecewise, three had a positively correlated and a negatively correlated component, one had two positively correlated components, and three had only one component of two that was correlated. Of all 28 conductance pairs, g_{CaT}/g_{Kd} exhibited the strongest relationship (Fig. 10(c)), with a ρ of 0.98 ($p < 1.4 \times 10^{-45}$). Linearly varying g_{CaT} to g_{Kd} with a ratio of approximately 0.019 results in phase maintenance. Deviating from this positive ratio results in a drastic increase in the spike phase difference. Notably, these two conductances do not tightly regulate whether the neuron is bursting; as can be seen in Fig. 10(a), the model neuron bursts across wide ranges of values for both conductances. For another strongly correlated conductance

pair, g_A and g_{CaS}, the conductances constrain the bursting ability of the neuron as well as the ability to maintain spike phase. Certain conductance pairs with nonmonotonic relationships had strongly monotonic regions that resulted in phase maintenance. The phase-maintained population for the g_{Na}/g_{Kd} pair had one region with a negative monotonic relationship (ρ = -0.89, $p < 1 \times 10^{-40}$) and another region with a positive monotonic relationship (ρ = 0.93, $p < 1 \times 10^{-10}$). Other pairs of conductances only exhibited correlations in certain regions of conductance space. Both the g_A/g_{Kd} pairs and the g_{CaS}/g_{Kd} pairs, for example, only exhibit correlations for higher values of g_{Kd}. The conductance that appeared to least affect average spike phase difference was g_H; no correlations of g_H with other conductances resulted in populations with spike phase maintenance.

Our criteria for a conductance relationship to be deemed a correlation included a minimum value for Spearman's ρ. Excluding this criterion would cause nine other pairs of conductances to appear correlated in the phase-maintained model neuron populations (Table 4). Some, such as the g_{Kd}/g_H pair, appear only weakly correlated. We have restricted our discussion to those relationships with a higher ρ, but we note that relaxing this criterion unmasks several weaker correlations that also modestly affect spike phase maintenance.

We examined the variation in period over the ranges of conductance values (data not shown); as with the experimental data, a strong relationship between spike phase maintenance and period maintenance does not appear to exist. Fig. 7 shows, for example, that the pairs of bursters exhibiting average spike phase differences of 0.0052 (a low value) and 0.075 (a high value) have similar differences in period. To see whether our choice of aligning bursts by their first spike affected our findings, we also examined the phase differences after aligning all bursters by their last spike. The phase differences were generally greater when using last-spike alignment, which may arise in part from the differing degrees of spike frequency adaptation at the ends of the bursts. However, the

correlations that resulted were highly similar to those found using first-spike alignment, suggesting that the overall relationship between phase maintenance and ion channel correlations is not localized to particular regions of the burst, but is generalizable to the nature of the burst as a whole.

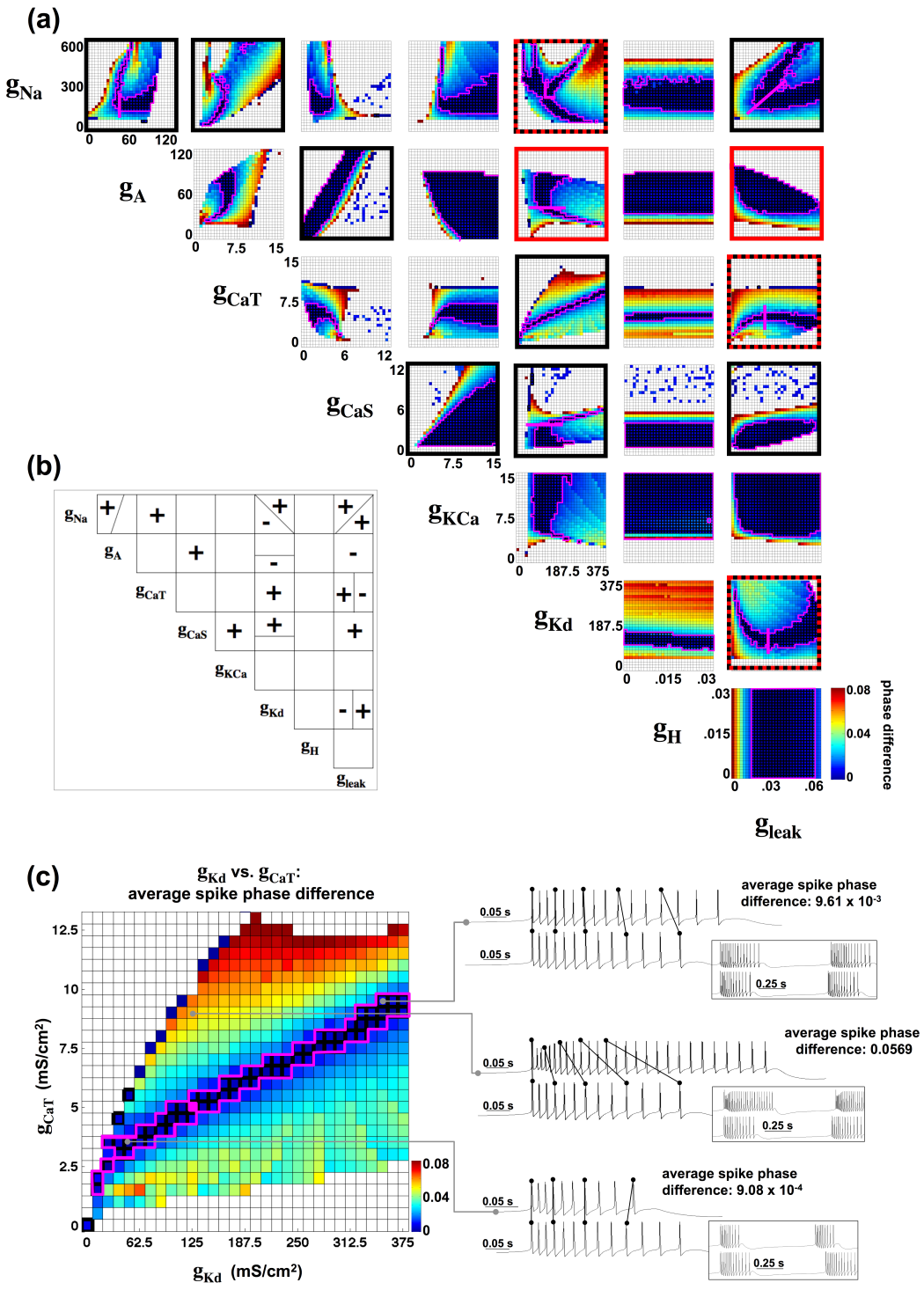

Figure 10. Phase differences and conductances correlations in the single-burster study. (a) Average spike phase differences relative to the canonical burster for the pairwise co-variations of all 28 pairs of conductances. Dark blue regions have the highest phase maintenance, and dark red regions have the lowest phase maintenance. White squares indicate model neurons that were not regular bursters. Regions with low spike phase differences (< 0.01) that were examined for correlations are outlined in magenta

and have their grid lines in bold. Conductance data sets with nonmonotonic relationships that resulted in phase maintenance were analyzed piecewise; the divisions between these regions of analysis are indicated with straight, solid magenta lines. Bold black outlines indicate conductance pairs with positive correlations, and bold red outlines indicate conductance pairs with negative correlations. Dashed red-and-black outlines indicate the presence of both a negative and a positive correlation. **(b)** Summary of correlations seen in all 28 conductance pairs. Positive correlations are indicated by a plus sign, and negative correlations are indicated by a minus sign. Conductance correlations were deemed present if Spearman's rank correlation coefficient had a value of $|\rho| \geq 0.4$ ($p < 0.05$). Blank squares indicate conductance pairs for which no correlation was found. Squares that are divided indicate nonmonotonic relationships that were analyzed in a piecewise fashion. **(c)** Original voltage traces show that positively varying g_{CaT} and g_{Kd} supports spike phase maintenance. Three pairs of voltage traces are shown whose phase differences are highlighted on the bar plot. Traces are normalized by their respective periods; the first spike of each burst is aligned. The lower trace in each pair represents one burst from the canonical model neuron, marked on the plot with a magenta square. The upper trace represents one burst from a model for which g_{Kd} and g_{CaT} varied from their canonical values. Black lines drawn between action potential peaks in the upper and lower traces show the divergence in phase between every third action potential of each burster. Traces in the insets have not been normalized by period to demonstrate the differences in the periods between the original and canonical bursters

2.3.3 Population study

The method of analysis used in the single-burster study only considers a very restricted region of conductance space, in which two of eight conductances are varied at one time. The second study, utilizing a large model neuron database, allowed all conductances to vary freely. Rather than plotting the phase differences between sets of models, we plotted two-dimensional histograms to determine whether certain pairs of conductances tended to vary together in a large model neuron population with a high degree of phase maintenance.

2.3.3.1 Histograms and difference matrices for a sample burster population

For each pair of conductances (28 in total) and each burster population, a 6-by-6 two-dimensional histogram was generated, plotting the number of model neurons in the subpopulation versus two of their conductance values. However, the two-dimensional

histograms do not explicitly account for the null hypothesis of independence between the two conductances' effects on bursting activity. To correct for this, a set of "expectation matrices" was generated (Hudson and Prinz 2010). These matrices are developed by multiplying the one-dimensional histograms for each single conductance together, then normalizing by the total number of model neurons in the population, to create a six-by-six grid of probability values. Each value represents the probability of a model neuron from the population being present in that bin, given the assumption that the two conductances are independent from one another. A set of "difference matrices," in which we subtracted the expectation matrix from the original two-dimensional histogram, was then plotted. In these plots, each bin illustrates the percentage difference between the expected value for the number of model neurons in that bin, given the assumption of independence between the conductances, and the actual value. To compare this method of examining model neuron populations to our original method of examining a single canonical burster, we first examined the conductance correlations of a population that included the canonical burster (Fig. 11). This population was constrained to include 13 spikes per burst, and its duty cycle range was allowed to vary by ± 0.005 from the canonical burster's duty cycle. By restricting the duty cycle to a range of 0.01, we guarantee that the average spike phase difference is less than this value. The correlations for the single-burster study are shown with the conductance correlations from the population study in Table 4.

The correlations calculated from phase difference (single-burster study) and the correlations calculated from the histograms (population-based study) both point to phase-maintaining relationships between the sodium conductance (g_{Na}) and transient calcium conductance (g_{CaT}), as well as between the slow calcium conductance (g_{CaS}) and calcium-dependent potassium conductance (g_{KCa}). According to our criteria, the population study does not explicitly show a correlation between the transient calcium conductance (g_{CaT}) and the delayed rectifier conductance (g_{Kd}), but Table 4 shows that the relationship is

comparably strong. The agreement between the two studies regarding the significance of these three conductance pairs suggests that they may play a role in spike phase maintenance in different regions of conductance space. There was no agreement between the two studies regarding which conductance pairs had negative conductance correlations that resulted in phase maintenance.

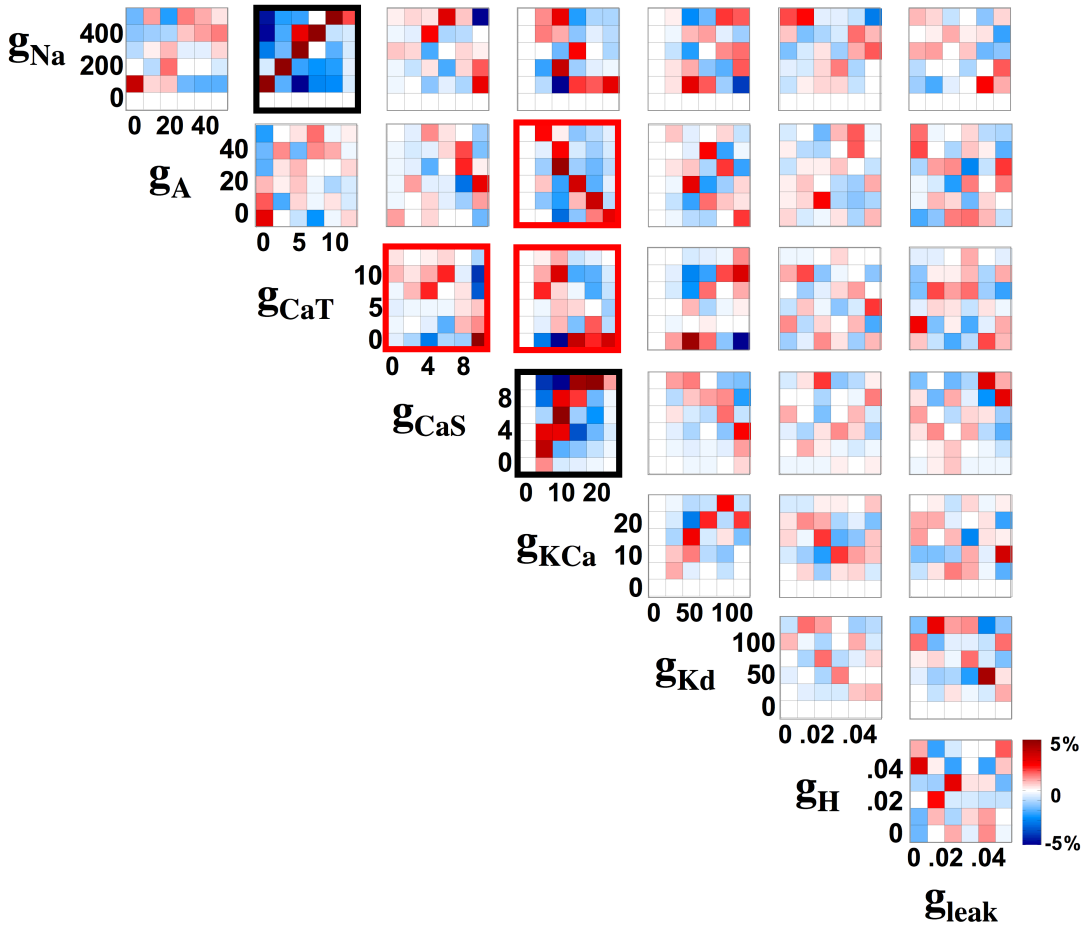

Figure 11. Difference matrices showing the presence of correlations between certain pairs of conductances for a burster population exhibiting a high level of phase maintenance. This population was chosen such that the canonical burster from the single-burster study would be included; the duty cycle was restricted to 0.2784 ± 0.005, and the number of spikes was restricted to 13 per burst. Bold black outlines indicate conductance pairs with positive correlations, and red outlines indicate the pairs that demonstrate a negative correlation

2.3.3.2 Comparison of several burster populations

In order to generate a single difference matrix, it is necessary to choose a single, arbitrary duty cycle range and number of spikes per burst. To further determine whether certain conductance correlations are consistently associated with phase maintenance for a variety of duty cycles and numbers of spikes per burst, we next examined several neuron populations in a similar fashion to the sample model neuron population discussed above. We investigated these sets of model neuron populations in two ways. First, we compared a set of model neuron populations with "high phase maintenance" to a set of populations with "low phase maintenance." Secondly, we compared the "high phase maintenance" populations, in which both duty cycle and number of spikes per burst were constrained, to analogous populations for which either the duty cycle or spike number was constrained, but not both. Conductance correlations that are present in the model neuron population exhibiting high phase maintenance, but not in the population exhibiting low phase maintenance or in the populations with only the duty cycle or spike number constrained, are specifically associated with maintaining phase.

2.3.3.3 "High" versus "low" phase maintenance populations

The "high phase maintenance" model neuron populations had spike numbers ranging from 5 to 20 and duty cycle ranges of 0.01 units in width ranging from 0.10-0.11 to 0.69-0.70. This resulted in 960 separate "high phase maintenance" populations. The "low phase maintenance" model neuron populations had spike numbers ranging from 5 to 20 and period ranges of 0.01 seconds in width, ranging from 0.5-0.51 seconds to 1.09-1.1 seconds, resulting in 960 "low phase maintenance" populations.

Histograms of the correlation coefficients for the populations of model neuron bursters with "high" and "low" phase maintenance were plotted for each of the 28 pairs of conductances, five of which are shown in Fig. 12. For certain pairs, the correlation coefficients appear stronger for the population representing high phase maintenance than

for the population representing low phase maintenance (g_{Na}/g_{CaT}, g_{CaS}/g_{KCa}, Fig. 12(a)-(b)). This suggests that correlating these particular conductances may aid specifically in the maintenance of spike phase. Certain other pairs, however, saw stronger correlations in populations with low phase maintenance (g_A/g_{CaS}, g_{CaT}/g_{CaS}, Fig. 12(c)-(d)). Other correlation coefficients do not appear to be specifically high for the population of neurons exhibiting high levels of phase maintenance, relative to those exhibiting low phase maintenance (g_{CaT}/g_{Kd}, Fig. 12(e)).

To ensure that the correlations seen were not a result of the initial restriction of the database to all regular bursters, pairwise correlations were calculated for several populations of 10,000 randomly chosen regular bursters. No strong correlations were evident in these populations, suggesting that restricting the neuronal activity type to bursting does not, by itself, result in the emergence of strong conductance correlations.

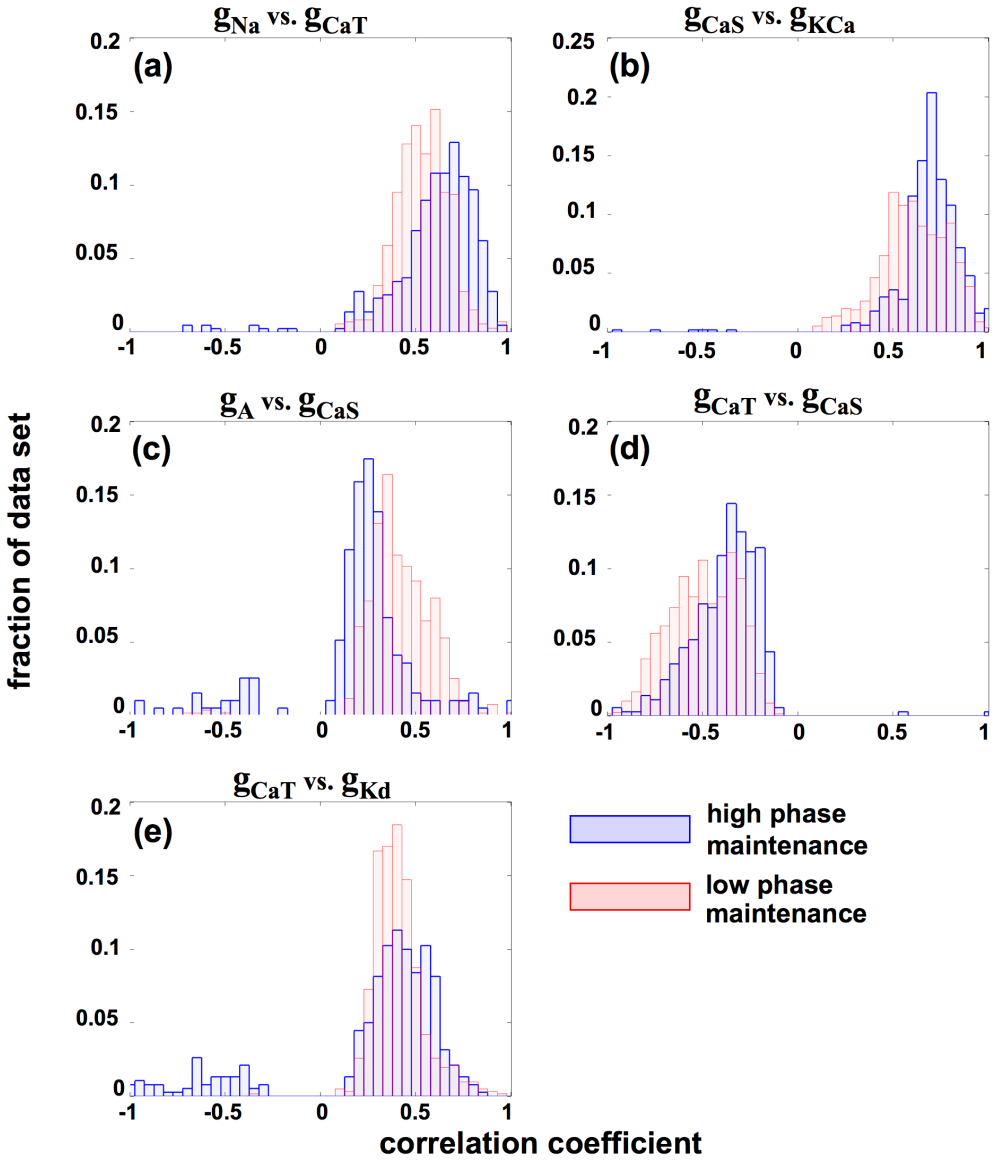

Figure 12. Histograms of conductance correlation coefficients for a selection of conductance pairs. The y-axis indicates what fraction of the entire data set each bin constitutes. Populations of bursters with a high degree of phase maintenance are shown in blue, and burster populations that emulate a lack of phase maintenance are shown in red. **(a)** g_{Na} and g_{CaT} ($p = 1.5 \times 10^{-20}$) and **(b)** g_{CaS} and g_{KCa} ($p = 6.37 \times 10^{-19}$) demonstrate positive correlations that were significantly stronger (Wilcoxon rank-sum test, $p < 0.05$) in the population with high phase maintenance than in the population with low phase maintenance. Conversely, the conductance pairs **(c)** g_A and g_{CaS} ($p = 1.1 \times 10^{-33}$) and **(d)** g_{CaT} and g_{CaS} ($p = 5.9 \times 10^{-24}$) demonstrated a significantly greater correlation in the population with low phase maintenance than in the population with high phase maintenance. **(e)** The g_{CaT}/g_{Kd} correlation coefficients demonstrated no difference between the populations with high and low phase maintenance. ($p > 0.05$)

2.3.3.4 Effect of constraining duty cycle or spike number alone

In order to compare the "high phase maintenance" populations with those populations in which only the duty cycle or the number of spikes per burst was constrained, two additional sets of populations were generated, one with the duty cycle constrained to a range of 0.01, and one with the number of spikes per burst constrained to a single integer value. Again, the model neuron populations had spike numbers ranging from 5 to 20 and duty cycle ranges of 0.01 units in width ranging from 0.10-0.11 to 0.69-0.70. To ensure that an adequate number of model neurons were present in the histograms (each of which consisted of a 6-by-6 grid), only those bins containing at least 200 model neurons were considered. This limited the analysis to 147 populations. The three sets of burster populations (those with a constrained duty cycle, a constrained spike number, and both a constrained duty cycle and spike number) were collected as follows. Exactly 200 model neurons were chosen from each of the 147 burster populations that were constrained by duty cycle and spike number and contained at least 200 bursters (Fig. 13(a)). Next, 147 populations consisting of exactly 200 model neurons that were constrained only by duty cycle were extracted by randomly selecting from all model neurons with a specific number of spikes per burst (Fig. 13(b)). The distribution of the duty cycle bins from which these populations were chosen was designed to match that of the populations constrained by both duty cycle and number of spikes per burst. For example, since there are three populations of at least 200 model neurons with 15 spikes per burst and some specific duty cycle range (outlined in red in Fig. 13(a)), three model neuron populations of 200 randomly chosen model neurons with an unconstrained duty cycle were also chosen from this bin, so that all of the model neurons in each of the three populations had 15 spikes per burst. A similar procedure was undertaken for selecting the 147 populations of bursters with a constrained duty cycle range (Fig. 13(c)). The X^2 and Spearman's ρ values of these three sets of 147 burster populations were then compared. Bar plots showing the percentage of model neuron populations with correlated

conductance pairs were compared for the three types of populations (Fig. 14), for all 28 conductance pairs. If a greater percentage of the populations with both duty cycle and spike number constrained had correlations than did those populations with either duty cycle or spike number constrained alone, it would suggest that spike phase maintenance, by our definition, is regulated by that particular conductance pair.

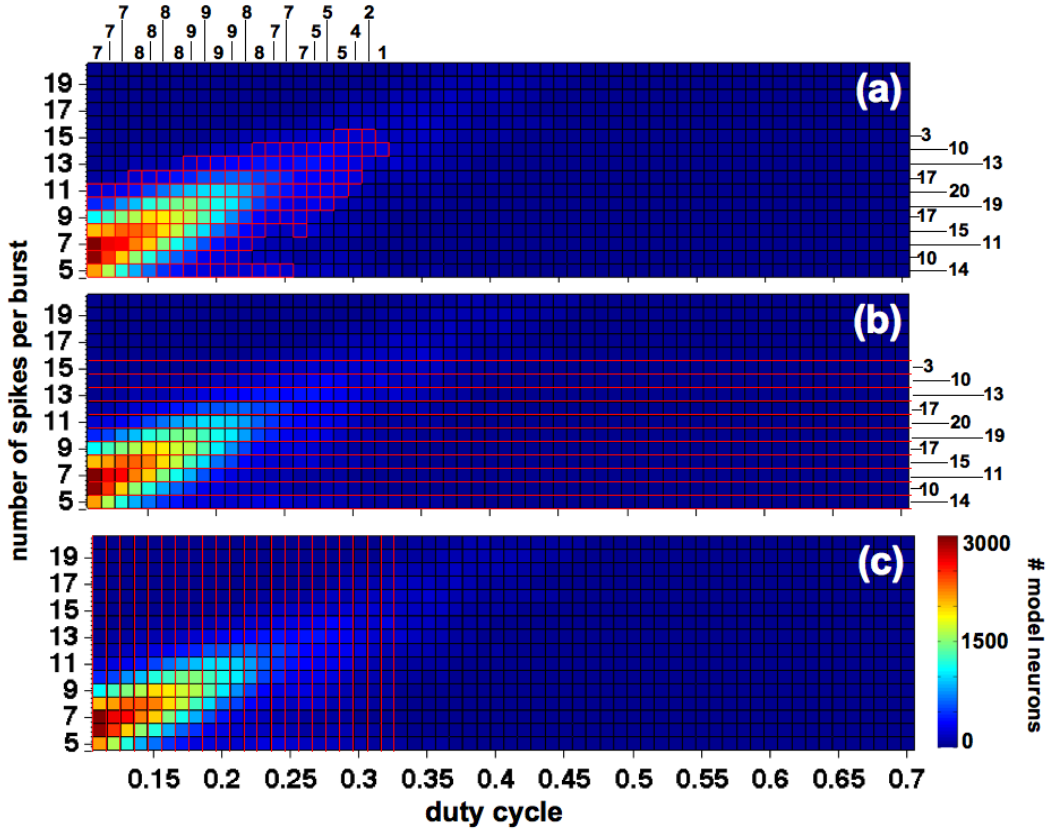

Figure 13. Histogram depicting the number of model neurons in each of the 960 bins selected by constraining the duty cycle and number of spikes per burst of model neurons in the database. To assess the relationship of conductance correlations to spike phase maintenance, model neuron populations were collected by constraining by duty cycle and number of spikes per burst, duty cycle alone, and number of spikes per burst alone. Model neurons were partitioned by duty cycle into bins of width 0.01 and by integer numbers of spikes per burst. **(a)** Bins outlined in red indicate populations constrained by both duty cycle and spike number that are also of a size greater than or equal to 200, fulfilling our criteria for analysis. **(b)** Populations of 200 randomly selected bursters were gathered from sets of data outlined in red, wherein the number of spikes per burst, but not duty cycle, was constrained. The number of populations from each set of data is indicated on the right of the panel. **(c)** Populations of 200 randomly selected bursters were gathered from sets of data outlined in red, wherein the duty cycle, but not the number of spikes per burst, was constrained. The number of populations from each set of data is indicated above the top panel

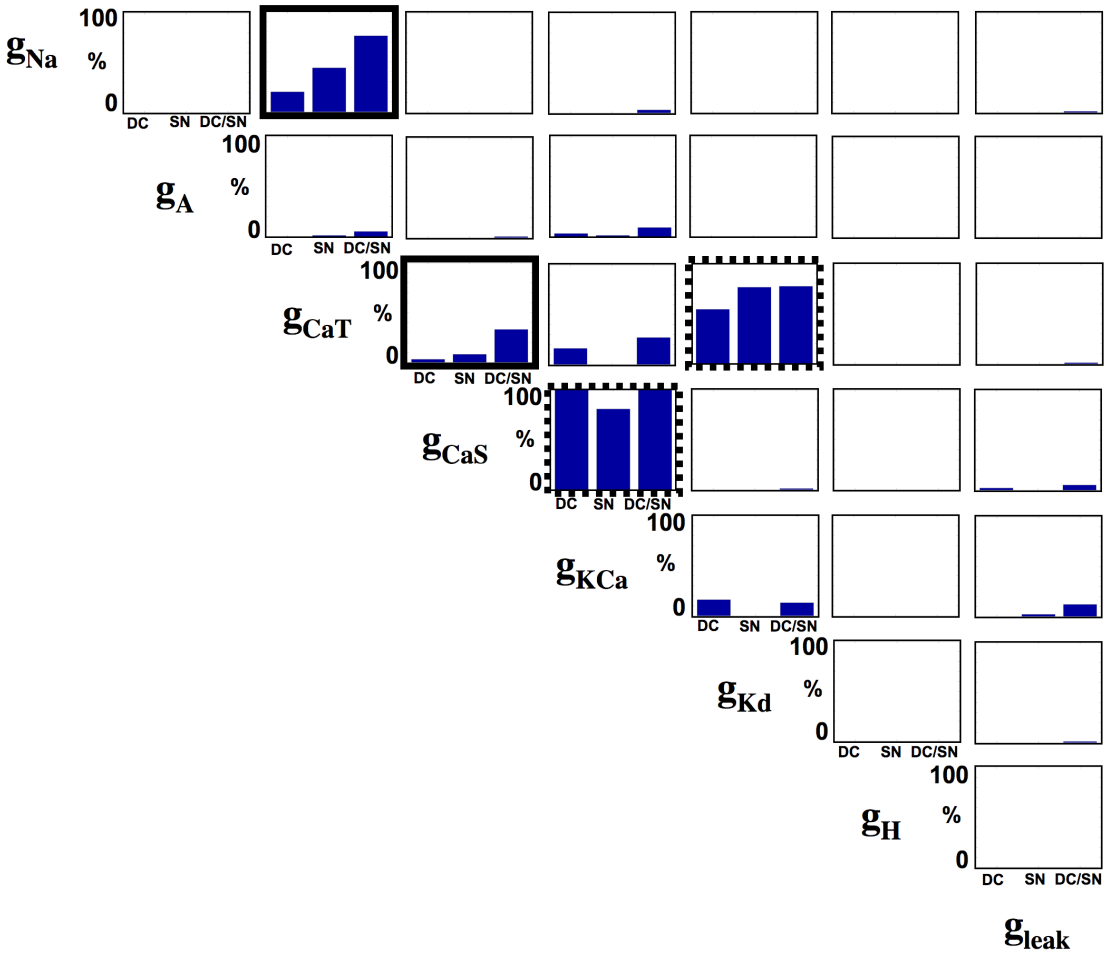

Figure 14. Percentage of model neuron populations that meet the criteria for significantly correlated conductances ($X^2 \geq 70$ and Spearman's $|\rho| \geq 0.30$). Bars indicate populations with constrained duty cycle (DC), constrained number of spikes per burst (SN), or with both constrained duty cycle and number of spikes per burst (DC/SN). Conductance correlations that appear specifically related to maintaining phase include g_{Na}/g_{CaT} and g_{CaT}/g_{CaS} (solid bold outlines). Correlations between g_{CaS}/g_{KCa} and g_{CaT}/g_{Kd} pairs (dashed outlines) are seen in all three types of populations

For the sodium and transient calcium conductances, 76% of the populations with a high degree of phase maintenance exhibited correlations, where both the duty cycle and number of spikes per burst were constrained. Of those populations with constrained duty cycle or constrained numbers of spikes per burst alone, 20% and 44% appeared to have strong correlations, respectively. Thus, the g_{Na}/g_{CaT} pair may be specifically involved in maintaining spike phase. Similarly, for the g_{CaT}/g_{CaS} pair, 33% of the populations with a

high degree of phase maintenance exhibited correlations, while only 3% and 8% of those populations with constrained duty cycle or constrained numbers of spikes per burst alone exhibited correlations. The g_{CaS}/g_{KCa} pair also exhibited a high number of strong correlations, but the percentages of strong correlations in each of the three sets of populations were similar, suggesting that this pair of conductances may be involved in maintaining one parameter or the other but is not exclusively associated with the maintenance of spike phase in bursting neurons.

It is possible that the duty cycle bin size (here, arbitrarily chosen to be 0.01 units in width) may affect whether correlations are present. We performed the above study using various bin sizes and found that as long as the bins are sufficiently small, their width does not greatly affect the strength of the correlation coefficients.

The box plots for the g_{Na}/g_{CaT} conductance pair (Fig. 15) and the g_{CaT}/g_{CaS} conductance pair (Fig. 16) illustrate stronger chi-squared values in the population exhibiting high phase maintenance. In the g_{Na}/g_{CaT} pair, the chi-squared values also appear to increase in strength as both the duty cycle and number of spikes per burst increase. This increase is most striking in the population with both parameters constrained. In the g_{CaT}/g_{CaS} pair, the populations with both parameters constrained have greater chi-squared values than the populations with only duty cycle or spike number constrained for the majority of duty cycle ranges and particularly at low numbers of spikes per burst. For both pairs, the Spearman's ρ values are similar for all three population types (duty cycle and spike number constrained, duty cycle constrained only, and spike number constrained only). Thus, for the g_{Na}/g_{CaT} and g_{CaT}/g_{CaS} conductance pairs, a stronger dependence exists between the conductances (indicated by the chi-squared value) for the population with both constrained duty cycle and spike per burst (representing high phase maintenance), but the monotonicity (indicated by ρ) is similar for all population types. The box plot for the g_{CaS}/g_{KCa} conductance pair shows that the correlations are similar for all three of the sets of populations, suggesting that this

particular conductance pair may be involved in constraining duty cycle or spike phase, but is not exclusively involved in maintaining both at once (Fig. 17).

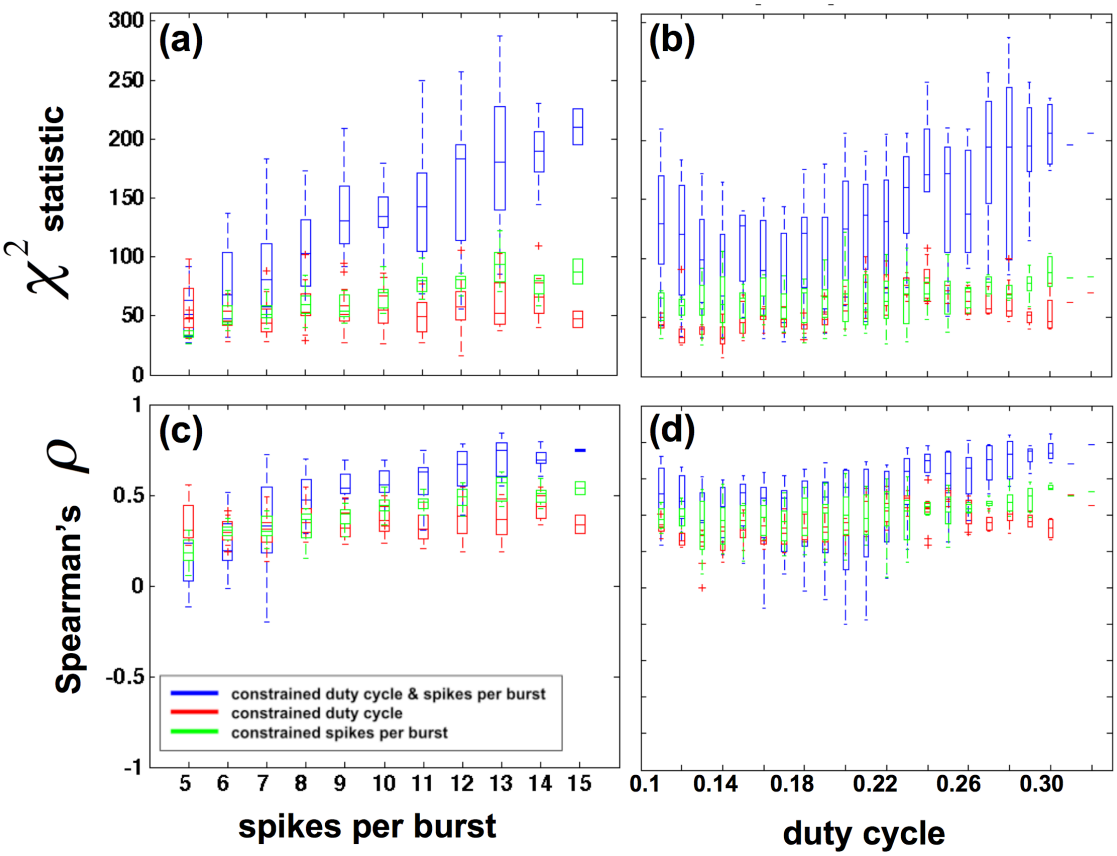

Figure 15. Chi-squared and Spearman's ρ values for the g_{Na}/g_{CaT} conductance correlation for the three population types, plotted by number of spikes per burst and duty cycle. The line bisecting each box indicates the median values for the statistic, and the ends of the boxes indicate the lower and upper quartiles. **(a)** As the number of spikes per burst is increased, stronger correlations are seen specifically for the population of bursters with both constrained duty cycle and spikes per burst. **(b)** Stronger correlations are also seen as the duty cycle is increased. **(c-d)** Spearman's ρ values are similar between all three population types for a range of values for duty cycle and spikes per burst. For the g_{Na}/g_{CaT} conductance pair, the population wherein the spike number and duty cycle are constrained (the "high phase maintenance" population) exhibits stronger correlations than the populations in which either parameter is constrained alone

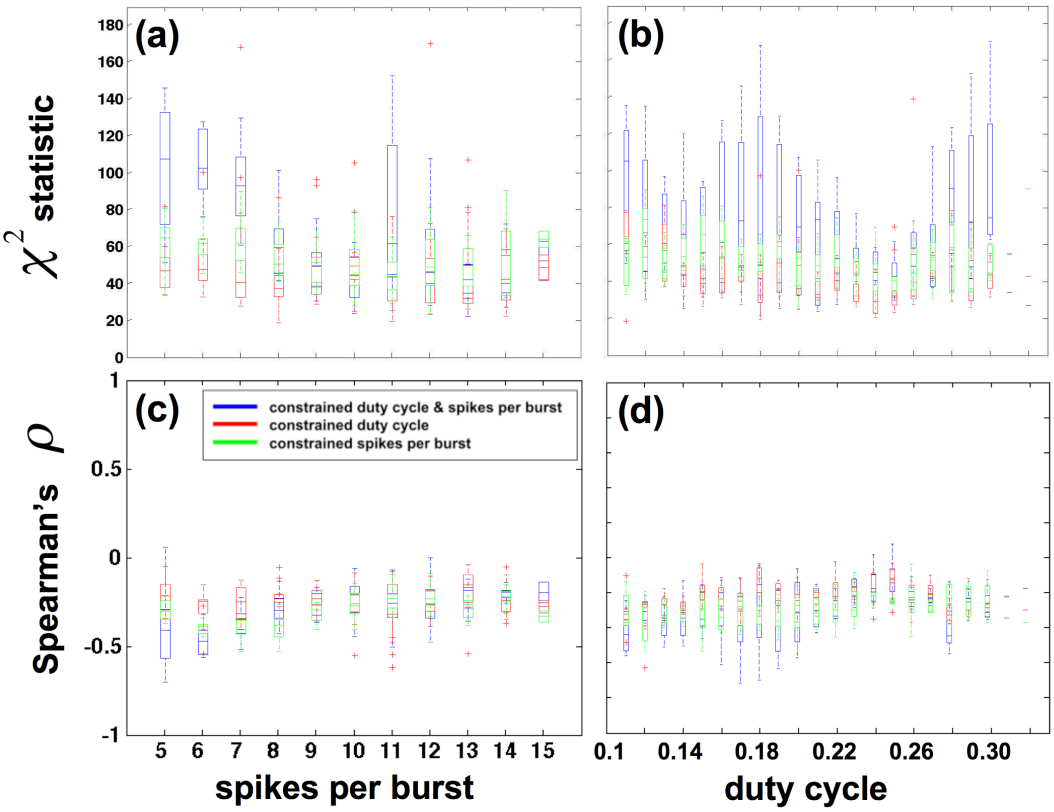

Figure 16. Chi-squared and Spearman's ρ values for the g_{CaT}/g_{CaS} conductance pair for the three populations, plotted by number of spikes per burst and duty cycle. The middle of the boxes indicates the mean values for the statistics, and the ends of the boxes indicate the lower and upper quartiles. **(a)** At lower numbers of spikes per burst, the population with both duty cycle and number of spikes per burst constrained (in blue) has higher chi-squared values than the populations in which either parameter is constrained alone . **(b)** For the majority of duty cycle ranges, the median chi-squared value is highest for the population with both parameters constrained. **(c-d)** The Spearman's ρ values are similar at all spike numbers and duty cycle ranges for the three populations. For the g_{CaT}/g_{CaS} conductance pair, the population with high phase maintenance exhibits stronger correlations than the populations in which either duty cycle or spike number is constrained alone

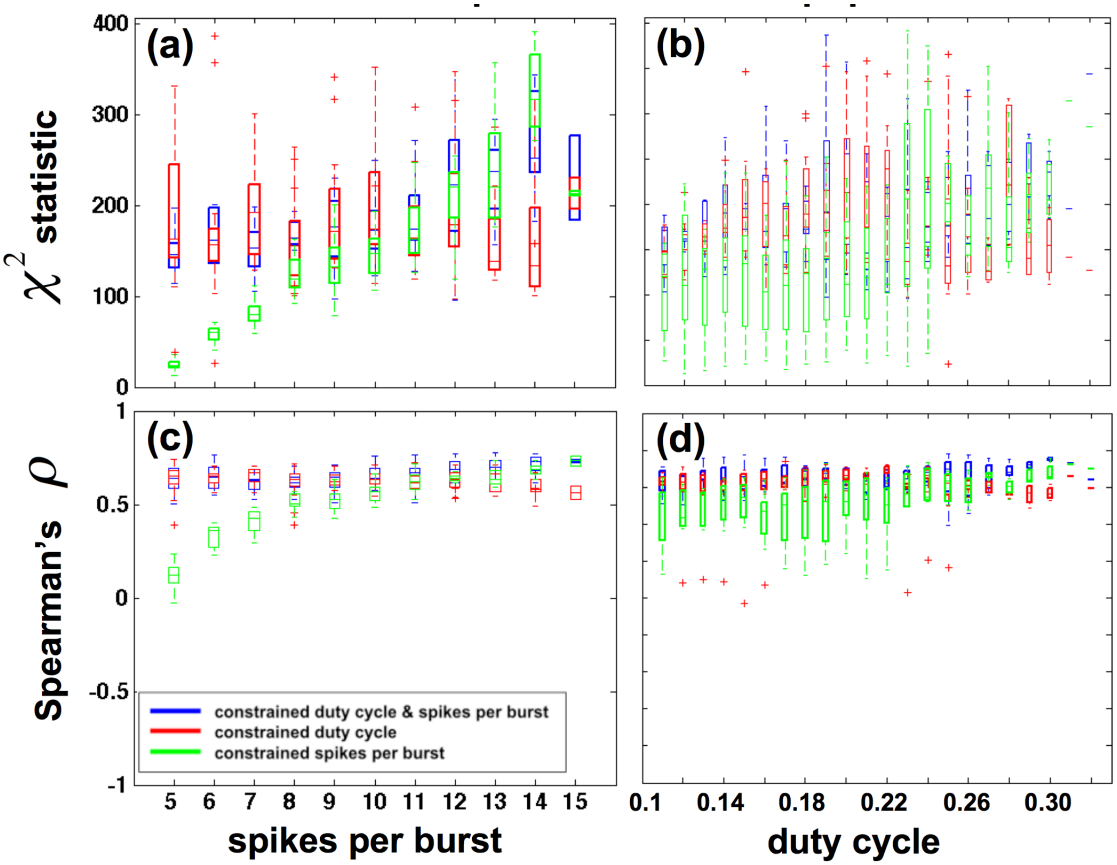

Figure 17 Chi-squared and Spearman's ρ values for the g_{CaS}/g_{KCa} conductance pair for the three populations, plotted by number of spikes per burst and duty cycle. The middle of the boxes indicates the median values for the statistic, and the ends of the boxes indicate the lower and upper quartiles. **(a)** As the number of spikes per burst is increased, stronger correlations are seen specifically for the population of bursters with only spikes per burst constrained. Average values for the chi-squared statistic are similar for all three population types. **(b)** Stronger correlations are seen as the duty cycle is increased, but average chi-squared values are again similar between all three populations. **(c-d)** Spearman's ρ values are similar between all three population types for a range of values for duty cycle and spikes per burst

2.4 Discussion

It is often assumed that for any nervous system to consistently produce behavior that is appropriate to the animal's environment, certain aspects of that nervous system must be held under tight neuromodulatory, cell-intrinsic, or synaptic control. In the present work, we observed through experiment that spike phase maintenance occurs in long-term recordings of some LP neurons as the period varies over time. We performed a series of

studies using a single-compartment neuron model to examine whether the experimentally observed activity could be emulated via the pairwise co-variation of conductances. We first studied the effect on phase maintenance of independently varying pairs of conductance values of a single, "canonical" model neuron. Next, we utilized a model neuron database to explore whether the distributions of the conductance values of model neurons are associated with spike phase maintenance. Conductance-based modeling studies implicated the correlation of specific conductance pairs as a possible mechanism by which the pyloric neurons accomplish spike phase maintenance.

The g_{Na}/g_{CaT} pair and the g_{CaS}/g_{KCa} conductance pair exhibited salient positive correlations in the single-burster and the population-based study. Of these pairs, g_{Na} and g_{CaT} appeared more specifically geared towards maintaining spike phase than maintaining other bursting properties, such as duty cycle or number of spikes per burst alone, while the g_{CaS}/g_{KCa} pair appears to support more general bursting properties. (Hudson and Prinz 2010) have also previously noted an association between g_{CaS}/g_{KCa} correlations and general bursting activity in model neurons.

Fig. 10 illustrates areas in g_{Na}/g_{CaT} conductance space that have both small (dark blue) and large (dark red) phase differences between bursters. Other conductance pairs in the single-burster study, such as g_A/g_{CaS} and g_{CaS}/g_{KCa}, had regions of bursters with low phase differences that transitioned sharply to regions of non-bursters. This suggests that g_{Na}/g_{CaT} co-regulation may exert a finer control over the intra-burst properties of the model neuron than other conductance pairs. The g_A/g_{CaS} and g_{CaS}/g_{KCa} pairs appear to be more involved in controlling overall activity type, perhaps because the g_{CaS} conductance reacts to changes in calcium on a slower time scale than the g_{CaT} conductance (Liu et al. 1998). The time constants of the various conductances, which determine the immediacy of activity-dependent conductance changes, could explain which conductances control which aspects of the model neuron's output; g_{Na} and g_{CaT} operate with fast time constants, which may enable their interplay to finely tune the spike times within bursts.

In the current body of literature, few studies have demonstrated that any calcium conductances are correlated with other conductances to regulate neuronal activity. A previous modeling study demonstrated that the g_A/g_{CaS} conductance pair resulted in tight regulation of crustacean cardiac motor neuron activity (Ball et al. 2010). This particular pair of conductances, along with the g_{CaS}/g_{KCa} pair, is also strongly correlated in several types of STG model neuron activity (Hudson and Prinz 2010), including general bursting activity. In our population study, the correlation between g_{CaS} and g_{KCa} was notably stronger in the model neuron populations with high phase maintenance than in those with low phase maintenance. While calcium currents have proven difficult to measure experimentally, the evidence from computational studies suggests that they may be involved in maintaining certain aspects of neuronal activity, including spike phase of bursting neurons.

The correlations we found in the population study apply only to bursters with periods, duty cycles, and numbers of spikes per burst within the examined ranges. Therefore, it is possible that other conductance correlations exist for bursting neurons that did not meet our criteria for analysis in this study, such as the nonlinear, concave g_{Na}/g_{Kd} correlation found in model neurons classified as bursters with only one spike per burst (Golowasch et al. 2002).

So far all conductance correlations that have been experimentally found to preserve neuronal activity in stomatogastric neurons have been positive. However, negative correlations have been seen to maintain bursting activity in large model neuron databases, including a strong negative correlation between g_A and g_{KCa} (Hudson and Prinz 2010). The present study similarly found a negative g_A/g_{KCa} correlation to be stronger in populations with highly maintained spike phases than those exhibiting a lack of phase maintenance. Hudson and Prinz also showed that a negative g_{Na}/g_{Kd} correlation preserves activity type in model neurons (2010); we saw regions of both positive and negative correlations for this conductance pair in our single-burster study (Fig. 10). From a

biological perspective, we expect a positive correlation between g_{Na} and g_{Kd} to support spike phase maintenance; because g_{Na} controls a depolarizing (inward) current and g_{Kd} controls a repolarizing (outward) current, it would seem that increasing (or decreasing) one conductance would require a compensatory increase (or decrease) in the other conductance to preserve neuronal activity. For similar reasons, one might have expected g_{Na} and g_{CaT} to be inversely rather than positively correlated. We currently do not know how a positive correlation between two depolarizing currents might be useful to the neuron. Overall, the negative correlations found in the present study were fewer in number and generally weaker than the positive correlations. Indeed, the only two conductance correlations that appeared in both the single-burster and population-based studies were positive.

Modifying conductances in the biological neuron involves several layers of cellular machinery; it thus may not occur quickly enough to explain the instantaneous spike phase maintenance that is seen over time in a single neuron (Fig. 9). However, the spike phase also is maintained across different animals, despite large differences in the average burst period (Bucher et al. 2005). Thus, pairwise co-variation of conductances may, at the least, provide a plausible explanation for maintenance in spike phase across animals. Possible mechanisms for this conductance co-variation include ion channel co-localization on the cell membrane or translation from mRNA strands with correlated copy numbers (Schulz et al. 2007). Alternatively, the ability of pyloric neurons to maintain spike phase over time may be "built into" the electrical activity of the circuit through adjustments to synaptic strength (Bucher et al. 2005). As with conductance-based mechanisms, a method for maintaining spike phase that relies on the electrical organization of the network is most likely not trivial and would require further investigation.

Both theoretical and experimental studies have shown that a variety of conductance relationship types can preserve neuronal activity. Linearly co-varying a potassium and a

calcium conductance preserved tonic activity in both the ventricular dilator (VD) neuron of the STG and in a conductance-based model neuron (Goldman et al. 2001). Modeling studies have also demonstrated that nonlinear conductance relationships may preserve one-spike burster activity (Golowasch et al. 2002). Our single-burster modeling study, involving pairwise conductance co-variation, demonstrated phase-preserving relationships that were both linear (such as g_{CaT}/g_{Kd}) and non-linear (such as g_{Kd}/g_{leak}), and it is possible that the neuron employs both types of relationships to preserve its activity. Additionally, previous studies have revealed three- and four-way linear correlations between mRNA levels in specific STG cell types (Schulz et al. 2007). A more thorough analysis of the model neuron database may also reveal conductance relationships residing in higher dimensions for model neuron populations with specific activity constraints.

A clear future aim is to verify through experiment whether the mechanisms for phase maintenance explored in the present study are being employed by real neurons. Previous experiments have used mRNA levels to quantify channel expression, but a linear relationship between mRNA abundance and conductance value has only been found for one conductance pair: g_A and g_{KCa} (Baro et al. 1997; Schulz et al. 2006). Since mRNA injection may not reliably control the values of all conductances examined here, such an approach might not be useful as experimental verification of our results. However, multiple membrane conductances can be simulated in real time using the dynamic clamp technique. One potential future direction is to utilize dynamic clamp to modulate pairs of membrane conductances in a biological neuron while monitoring intra-burst activity to determine whether phase maintenance can be achieved via the mechanisms explored here.

Notably, the results presented above examined only spontaneous activity and do not examine the effects of synaptic input on the relationship between conductance correlations and phase maintenance. If the model neuron here were receiving regular

inhibitory synaptic input, as in a network model, its steady-state activity may be altered (Prinz et al. 2003b). We have seen in the present study that altering neuronal activity may result in different patterns of conductance co-regulation (Fig. 15); the specific conductance correlations that preserve intra-burst activity may be altered by the addition of synaptic input. As an example, the present study saw no pairwise conductance correlations involving g_H. Co-regulation of the g_A/g_H pair has experimentally been shown to preserve neuronal activity, including number of spikes per burst (Khorkova and Golowasch 2007; MacLean et al. 2005). Our model may be operating in a voltage regime that does not engage the hyperpolarization-activated current, so that the value of g_H plays little role in its activity. If we were to perform a similar analysis on a model neuron receiving extra inhibitory synaptic input from other neurons, the g_H conductance might play a greater role in controlling neuronal output.

It has been hypothesized that the presence of conductance correlations has certain benefits. The fact that there are many combinations of conductances that allow the neuron to arrive at the same activity type aids in the robustness of that activity. These correlations may provide protection against drastic and potentially harmful changes to neural activity as a result of a relatively small change in one or more ionic currents.

2.5 Acknowledgements

We thank Amber Hudson for informative discussions and valuable comments on the manuscript. We also thank the reviewers of the manuscript for their constructive criticism. This work was supported by grants from the National Institute of Health/National Institute of Neurological Disorders and Stroke (1F31NS071834-01 to SA and R01 NS054911 to AP), two National Science Foundation IGERT awards (to SA and WS), and a National Science Foundation Graduate Research Fellowship (to WS).

CHAPTER 3

DIFFERENTIAL EFFECTS OF CONDUCTANCES ON THE PHASE RESETTING CURVE OF A NEURONAL OSCILLATOR

3.1 Introduction

Computational and experimental studies in both vertebrate and invertebrate neuronal networks have indicated that the densities of membrane ion channels in individual neurons can vary several-fold (Goaillard et al. 2009; Goldman et al. 2001; Golowasch et al. 1999; Golowasch et al. 2002; Marder and Goaillard 2006; Schulz et al. 2006; Swensen and Bean 2005). Specific conductances can affect certain aspects of neuronal activity; for example, the A-type potassium current (I_A) influences firing rate (Connor et al. 1977), and the hyperpolarization-activated mixed ion current (I_H) affects burst duration and duty cycle in bursting neurons (Ouyang et al. 2007). However, we cannot always predict whether altering these intrinsic neuronal properties will result in meaningful changes to network output (Prinz et al. 2003b). Recent work suggests that modifying intrinsic cellular properties alone, without altering synaptic properties, can result in a wide range of network behaviors (Prinz et al. 2004b). However, a neuron's individual conductances may have very different effects on activity depending on whether the neuron is isolated or connected to a functional network (Wolfart et al. 2005).

It is therefore of interest to rigorously examine how a neuron's response to synaptic input is influenced by its ionic conductances. This topic has been studied in multiple contexts; various ion channel types have been shown to influence neuronal response to input in invertebrate neurons (Prinz et al. 2003a; Prinz et al. 2003b) as well as mammalian neurons (Day et al. 2005; Vervaeke et al. 2006); the H current, in particular, has been implicated in inducing network-level hyperexcitability, leading to febrile seizure (Chen et al. 2001). We chose to investigate the effect of specific conductances on neuronal response to input in a well-studied central pattern generator (CPG) - the pyloric

circuit, found in the stomatogastric ganglion (STG) of the decapod crustacean. This circuit produces a triphasic rhythm with a cycle period that reliably falls between 0.5 and 2 seconds, and the cellular and synaptic properties of the system have been well-characterized (Marder and Bucher 2007; Stein 2009). The circuit consists of a pacemaker kernel that includes the anterior burster (AB) and pyloric dilator (PD) neurons, in addition to two types of follower neurons, the lateral pyloric (LP) and pyloric (PY) neurons.

The effect of synaptic input on a neuronal oscillator, such as the AB/PD complex, can be conveniently summarized with the phase resetting curve, or PRC, which describes the change in oscillator period as a function of the phase at which an input perturbation was received (Pinsker 1977). Here, we use a combination of computational and experimental approaches to systematically examine the effect of individual conductances on the PRC of the pacemaker kernel in the pyloric circuit. We first use an existing single-compartment model neuron database to catalogue the sensitivity of various PRC attributes to specific conductances. We then tabulate PRCs in the PD neuron of *Cancer borealis* while dynamic-clamp-injecting the neuron with ionic currents using maximal conductances of varying magnitudes, then determine how each of the currents affects PRC shape. We further investigate the effects of the H and leak conductances by examining them in a four-compartment model of the pacemaker kernel. Finally, we report the effect of endogenous I_H on the neuronal response to synaptic input by tabulating the PRC of the PD neuron while pharmacologically blocking I_H.

3.2 Methods

3.2.1 The phase resetting curve

The response of an oscillating neuron to synaptic input is dependent, in part, upon when that input was received relative to the oscillation (Brown and Eccles 1934). One method of summarizing this effect is by plotting the phase response curve, or the phase resetting

curve (PRC) (Pinsker 1977; Pinsker and Kandel 1977). The PRC is a plot of the change in the period of the oscillator, normalized by the intrinsic burst period, as a function of the phase of the oscillation at which the input perturbation was received (Figure 18). If we indicate the intrinsic bursting period as P, and the ith period that was altered due to an input perturbation as P_i', then the phase response (plotted on the y-axis) is defined as $(P_i'-P)/P$. If we indicate the time at which the ith perturbed period begins as T_i, and the time at which the ith input was received as S_i, then the stimulus phase (plotted on the x-axis) is defined as $(S_i-T_i)/P$. Reductions in the burst period ($P_i'<P$) are indicated as negative values, and increases in the burst period ($P_i'>P$) are indicated as positive values. Figure 18 illustrates the response of a typical PD neuron to a stimulus S_n, where n is a particular instance of i. All PRCs tabulated in this study are *immediate* PRCs; they describe the change in the period that occurs due to the advance or delay of the burst immediately following the input perturbation. Three salient attributes of the PRC are indicated in Figure 18b, including the minimum phase response, the maximum phase response, and the neutral phase point (defined as the greatest stimulus phase that produces a phase response of zero).

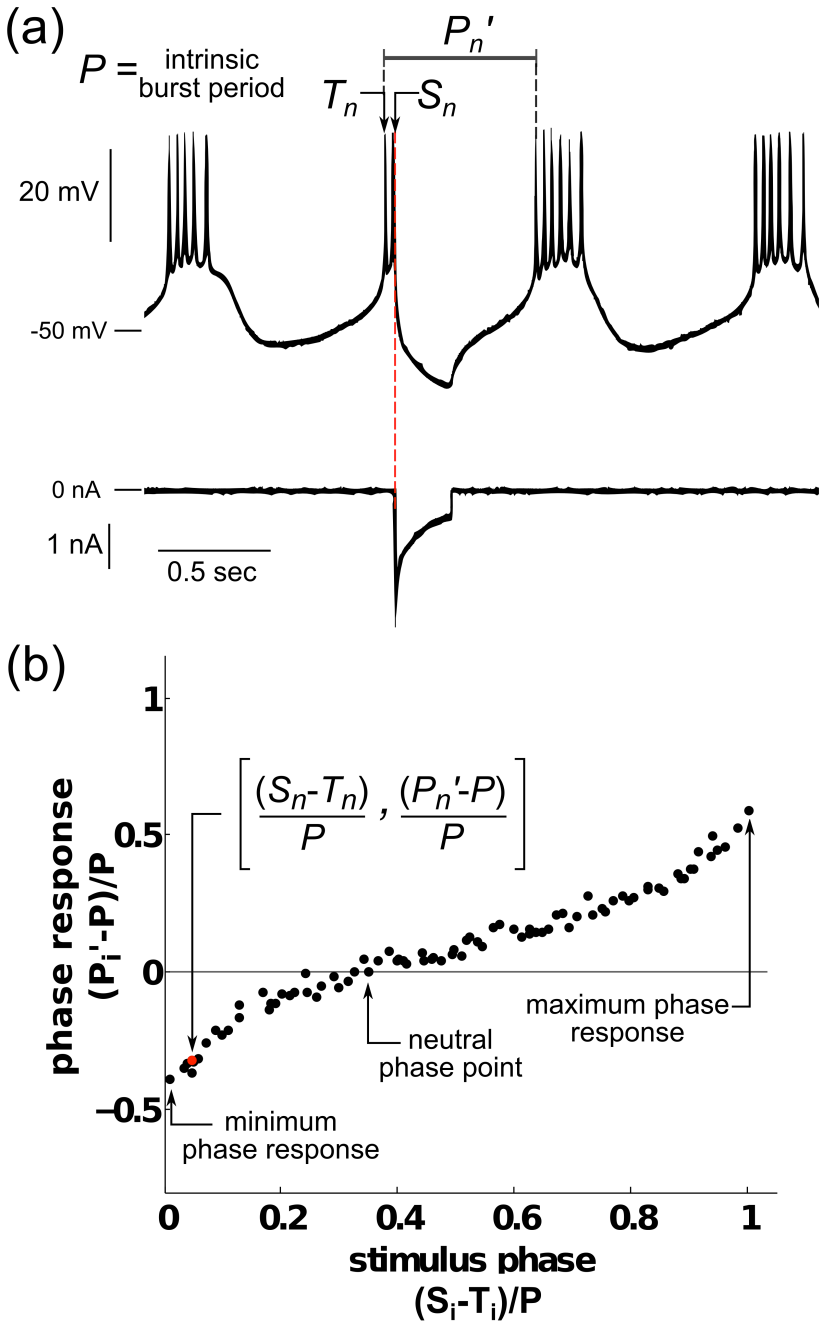

Figure 18. The phase resetting curve in a regular bursting neuron. (a) Voltage trace (top) of a biological PD neuron with intrinsic burst period *P*, and current trace (bottom) of injected artificial synaptic input. At time S_n, a pulse of artificial inhibitory synaptic input (100 nS) is given, resulting in the perturbed period P_n'. (b) PRC obtained from the PD neuron shown in (a). The *i*th stimulus phase, defined as the time from the beginning of the last burst, T_i, to the stimulus time, S_i, normalized by P, is plotted on the x-axis. The phase response, defined as the difference between the perturbed period P_i' and P, normalized by P, is plotted on the y-axis. The phase response at $i=n$ is highlighted in red. The minimum and maximum phase responses and the neutral phase point are labeled on the plot.

3.2.2 Classifying model neurons

To examine the effect of conductances on the PRCs of single-compartment model neurons, an existing model neuron database was used (Prinz et al. 2003a). This database was constructed by independently varying the maximal conductances (hereafter referred to simply as "conductances") of eight separate Hodgkin-Huxley-type currents. The currents modeled were: fast sodium (I_{Na}), fast and slow calcium (I_{CaT} and I_{CaS}), fast potassium (I_A), calcium-dependent potassium (I_{KCa}), delayed rectifier (I_{Kd}), hyperpolarization-activated (I_H), and leak (I_{leak}). The currents were modeled as by Liu et al. (1998) with the exception of I_H, which was modeled as by Huguenard and McCormick (1992). The currents from Liu et al. (1998) were based on experiments on stomatogastric neurons in lobster (Turrigiano et al. 1995), and the I_H current was based on guinea pig thalamic relay cells (Huguenard and McCormick 1992; McCormick and Pape 1990). The equations that describe the model currents, including the voltage dependences of the activating and inactivating time constants and the steady-state activation and inactivation variables, are described in full in Prinz et al. (2003a). Each of the eight conductances was assigned one of six equally spaced values within a conductance-specific range. For simplicity, here we use normalized conductance values rather than absolute values when referring to conductance levels. We call these normalized values *M*, where *M* can have a value of 0, 1, 2, 3, 4, or 5, with 5 indicating the conductance-specific maximum level. Voltage traces were then simulated for every conductance combination. The total number of model neurons in the database was thus 6^8, or 1,679,616 model neurons. In the original model neuron database, 1,065,225 of these model neurons were classified as regular bursting neurons, and their corresponding PRCs were simulated (Prinz et al. 2003a). Within this set of simulated PRCs, certain bursters had extreme delays. Those bursters with maximum PRC values not between 0 and 1 (0.3% of the population) were excluded from analysis, as were those that had been misclassified as a result of

alternating burst attributes (Hudson and Prinz 2010). We restricted our analysis to multi-spike bursters alone, as classified in Hudson and Prinz (2010). Of the multi-spike bursters, we only included model bursters for which a majority of the spikes rose beyond 0 mV (in the case of two-spike bursters) or 20 mV (in the case of multi-spike bursters). This classification resulted in 292,313 model neurons that we term "PD-like" bursters (Figure 19).

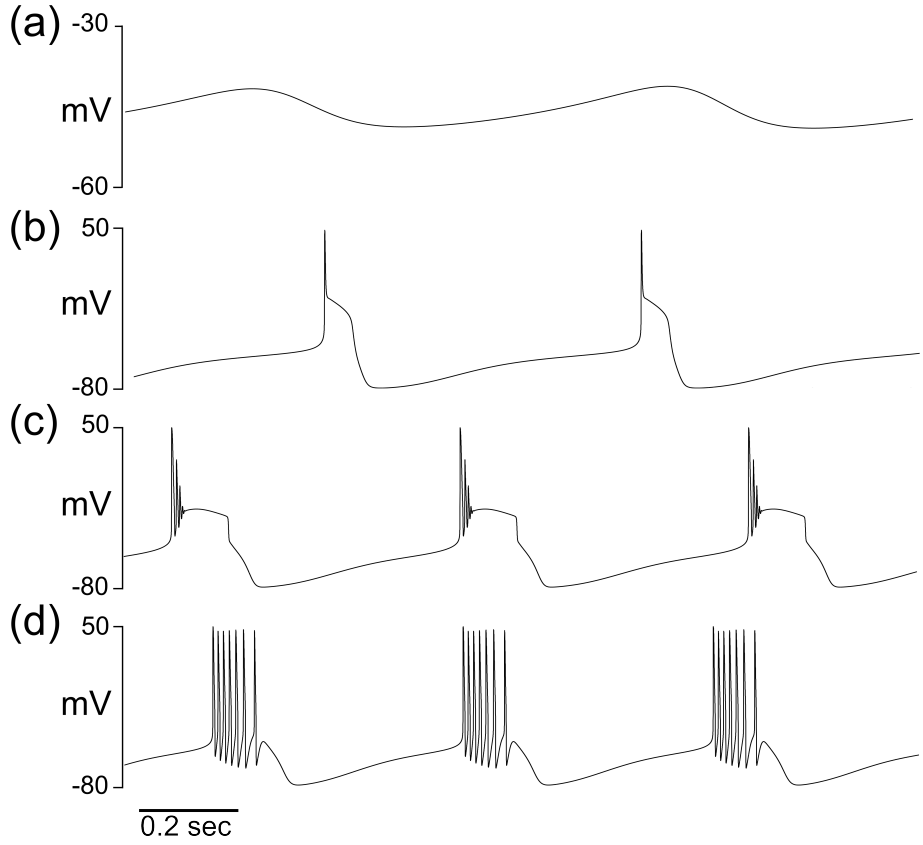

Figure 19. PD-like bursters were chosen from the model neuron database. (a) Voltage trace of a model neuron with rhythmic, nonbursting activity. Maximal conductances in mS/cm^2: Na 0, CaT 0, CaS 8, A 40, KCa 10, Kd 100, H 0.04, leak 0.05. (b) Voltage trace of a model neuron classified as a one-spike burster. Maximal conductances in mS/cm^2: Na 100, CaT 12.5, CaS 2, A 0, KCa 15, Kd 25, H 0, leak 0.01. (c) Voltage trace of a model neuron that is classified as a multispike burster, but has a majority of spikes with peak amplitude below 20 mV. Maximal conductances in mS/cm^2: Na 400, CaT 0, CaS 10, A 50, KCa 10, Kd 0, H 0.01, leak 0.01 (d) Voltage trace of a model neuron that is classified as a multispike burster and has a majority of spikes with peak amplitude above 20 mV. Maximal conductances in mS/cm^2: Na 500, CaT 2.5, CaS 6, A 10, KCa 20, Kd 50, H 0.05, leak 0.01. Only model neurons that met the criteria of (d) were analyzed.

3.2.3 Investigating effect of conductances on specific PRC attributes in burster populations

For all "PD-like" bursters, we determined the effect of each of the 8 conductances ($\bar{g}_{Na}$, $\bar{g}_{CaT}$, $\bar{g}_{CaS}$, $\bar{g}_{A,}$ $\bar{g}_{KCa}$, $\bar{g}_{Kd}$, $\bar{g}_{H}$, $\bar{g}_{leak}$) on the distribution of three specific attributes of the PRC. These attributes included: 1) the maximum phase response (i.e. the greatest y-value of the PRC), 2) the neutral phase point (defined as the largest stimulus phase (x-value) at which the PRC has a phase response of zero), and 3) the minimum phase response (i.e. the lowest y-value of the PRC). The analysis was performed as follows: For each conductance $\bar{g}_{x,}$ where *x* indicates Na, CaT, CaS, A, KCa, Kd, H, or leak, we separated the "PD-like" model neurons into 6 subpopulations, each of which had the conductance $\bar{g}_{x}$ constrained to one of the six possible values and all other conductances unconstrained. We then generated a set of 6 histograms, one for each subpopulation, indicating the distribution of values of the maximum phase response. This was done for all 8 conductances, resulting in 8 sets of 6 histograms of maximum phase responses. These histograms, separated by conductance identity, are shown in Figure 21. Similar sets of histograms showing the distributions of neutral phase points and minimum phase responses in each subpopulation are shown in Figures 22 and 23, respectively.

We then calculated the sensitivity of the maximum phase response to each conductance by finding the change in the mean value of each subpopulations' maximum phase response relative to the change in each conductance value, normalized by the range of those conductance values in the database (Figure 24a). The histograms for zero conductance values were not included in the calculation of sensitivity. Similar sensitivity analyses were performed for the neutral phase point and minimum phase response (Figure 24b, c).

3.2.4 Investigating conductance effects on specific PRC attributes in burster families

To determine the effects of changing an individual conductance on a single neuron in the database, we also searched for "families" of PRCs within the set of PD-like bursters. Families were defined as sets of model neurons for which seven of the eight conductance values were identical and the eighth conductance was allowed to vary. Model neurons with a zero value for the eighth conductance were not analyzed, since the behavior of the model neuron with that zero conductance was often drastically different from the others in the family. Thus, each family could have a maximum of five members. Only families with at least three members that were classified as "PD-like" bursters were analyzed.

For each of the analyzed families, the value of the maximum phase response was plotted against the normalized value of the single, unconstrained conductance. The slope of this plot indicates the sensitivity of the maximum phase response to the conductance. The sensitivities of all analyzed families' maximum phase responses were plotted in a box-and-whisker format for each of the eight conductances. The above procedure was repeated for the neutral phase point and minimum phase response (Figure 25).

3.2.5 Dissection

All experiments were performed at Emory University. Live Jonah crabs (*Cancer borealis*) were purchased, shipped from The Fresh Lobster Company LLC (Gloucester, MA), and kept in artificial seawater (~12-13°C) until use. Animals were anesthetized in ice for 30-45 minutes before dissection. The stomach was removed from the animal and pinned flat in a large dish lined with Sylgard® (Dow Corning, Midland, MI). The stomatogastric nervous system was dissected from the stomach and pinned in a Sylgard®-lined plastic Petri dish. The STG was desheathed with a sharp pin and forceps, and the sheath was pinned to the Sylgard® on either side of the STG to expose the cell bodies and neuropil. During dissections, the preparation was immersed in saline (11 mM KCl, 440 mM NaCl, 13 mM $CaCl_2$•2H20, 26 mM $MgCl_2$•$6H_20$, 11.2 mM Trizma® base,

5.1 mM maleic acid, pH 7.45±0.03). The saline was changed every 15-20 minutes while in the large dish, and every 10 minutes while in the small dish.

3.2.6 Electrophysiology

To obtain extracellular recordings of the PD, LP, and PY neurons, wells of petroleum jelly (Vaseline®) were built around the *lvn*s and tested for impermeability. After the dissection, the preparation was moved to an electrophysiology rig. Fresh saline was chilled with a thermoelectric (Peltier) SC-20 Dual Inline Solution Heater/Cooler controlled by a CL-100 Bipolar Temperature Controller (Harvard Apparatus/Warner Instruments) and perfused onto the nervous system at a temperature of ~12-13°C. Temperature of the saline in the dish was continuously monitored using a BAT-12 Microprobe thermometer (Physitemp Instruments, Clifton, NJ). The extracellular activity was monitored from the *lvn* by placing a stainless steel wire electrode inside one of the wells and a second electrode outside the well. The signal from the wires was amplified using an A-M Systems Model 1700 Differential AC Amplifier. Before beginning intracellular injections, the extracellular trace was examined; any preparations that did not exhibit consistent, rhythmic bursting activity were excluded from analysis. To make sharp microelectrodes for intracellular recordings, borosilicate glass capillary tubes (OD 1 mm, ID 0.78 mm) were pulled with a P-97 Flaming/Brown Micropipette Puller (Sutter Instruments, Novato, CA). Electrodes were filled with 0.6 M K_2SO_4 and 20 mM KCl. Microelectrode resistances were between 10-25 MΩ. Intracellular electrodes were placed in a headstage and controlled with Leitz mechanical manipulators. An Axoclamp-2B amplifier (Axon Instruments, Foster City, CA) in discontinuous current clamp (DCC) mode was used to amplify the intracellular signal. The signal was digitized using a Digidata 1200A board (Axon Instruments) and recorded with Clampex 9.2 on a PC running Windows XP. Experimental files were analyzed with Spike2 (Cambridge

Electronic Design, Cambridge, UK) and MATLAB (The Mathworks, Natick, MA) using a combination of in-built functions and custom-made scripts.

The PD neuron was identified by its intracellular voltage waveform and the timing of its bursts within the pyloric rhythm (visible in the *lvn* extracellular recording). After one of the PD neurons was found, the single chemical synapse (LP-to-PD) onto the pacemaker kernel was blocked by perfusing the bath with 10^{-5} M picrotoxin, resulting in pharmacological isolation of the pacemaker kernel from the rest of the circuit. To obtain PRCs with I_H under pharmacological blockade, we first obtained several PRCs while perfusing the preparation with crab saline that contained only picrotoxin, then switched to blocker saline containing picrotoxin and 5 mM CsCl (Sigma-Aldrich, St. Louis, Missouri). The preparation was perfused with blocker saline for approximately 25 minutes before rerunning PRC protocols.

3.2.7 Dynamic clamp

We used the Real Time Linux Dynamic Clamp Controller (RTLDC) (Dorval et al. 2001) to add artificial membrane currents and synaptic input to the PD neuron (Prinz et al. 2004a; Sharp et al. 1993a; b). The voltage waveform was amplified via the amplifier headstage, sent to a DAQ board (National Instruments, Austin, Texas) through a rack-mounted BNC terminal block (BNC-2090, National Instruments), and digitized at 20 kHz. A program was written in C++ (partially adapted from code described in (Sieling et al. 2009)) to read the voltage waveform and calculate intrinsic membrane currents and synaptic currents. The intrinsic membrane currents were calculated using the general formula

$$I_x = \bar{g}_x m_x^{p_x} h_x (V_m - E_x)$$

where $\bar{g}_x$ indicates one of the conductances (Na, A, Kd, H, or leak), $m_x^{p_x}$ is the activation variable with exponent p_x, h_x is the inactivation variable, V_m is the membrane voltage, and E_x is the reversal potential. The values for each parameter are identical to those used

to construct the model neuron database (Huguenard and McCormick 1992; Liu et al. 1998; Prinz et al. 2003a). The currents I_{CaT}, I_{CaS}, and I_{KCa} were not simulated due to the inability to accurately measure calcium concentrations inside the PD neuron in real time. The synaptic input was modeled with an instantaneously activating synaptic conductance using the formula

$$I_{syn} = \bar{g}_{syn}(V_m - E_{syn})$$

where $\bar{g}_{syn}$ was 100 nS (when the synapse was active) and E_{syn} was -90 mV, as used in previous studies (Prinz et al. 2003b; Thirumalai 2002). Voltage traces were shifted and scaled to a standard slow-wave envelope at which the injected model currents were active. All injected currents were scaled relative to the measured input resistance of each neuron. For each of the five conductance types, a range of conductance values was chosen that produced visually detectable alterations of the membrane voltage waveform when injected into the PD neuron,. During each experiment, an RTLDC program was run that dynamic-clamp-injected one of the five membrane currents into the PD neuron, using a specific maximal conductance value within the chosen range. While injecting this intrinsic membrane current, the intrinsic burst period P_{init} was calculated by determining the average period over 20 bursts. Bursts were detected by isolating the slow-wave portion of the voltage waveform with a low-pass filter and detecting the rising phase of each oscillation with a simple voltage threshold (Sieling et al. 2009). After P_{init} was established, the program began to deliver periodic synaptic pulses (I_{syn}) to tabulate the PRC; this was done by setting $\bar{g}_{syn}$ to 100 nS when the artificial synaptic stimulus was being injected and 0 nS at all other times. To obtain each PRC, 100 synaptic pulses were injected that began at specified stimulus times S_i after a burst was detected. The ith stimulus time S_i was defined as $S_i = P_{init}k$ where $k = \{0, 0.01, 0.02 \ldots 0.99\}$. The pulse phases were delivered in a random order. One injection was given every 3 to 4 cycles.

For certain experiments, the stimulus duration was set at a constant 250 ms; for others, it was set at 25% of P_{init}.

For certain experiments, we injected membrane currents at 6 or 7 different maximal conductance levels within the chosen range and tabulated one PRC at each conductance level. For other experiments, we injected currents at only 3 different maximal conductance levels within the chosen ranges and tabulated 2 or 3 PRCs at each conductance level. The maximal conductance levels were injected in a random order (rather than in ascending or descending order) to ensure that any changes in the PRCs were indeed due to the injected membrane current and not to other, unknown changes in the system over time. Since the protocol was performed using DCC mode, the same electrode was used to inject current and record the membrane voltage.

In two cases, both PD neurons were clamped and had intrinsic membrane conductances added to them, and in one case, one PD was photoinactivated using Alexa 568 dye (Invitrogen, Carlsbad, CA) (Miller and Selverston 1982).

3.2.8 Tabulating PRCs

PRCs were tabulated *post hoc* using MATLAB. The intrinsic bursting period that was used to calculate the PRC, P, was calculated as the average value of all unperturbed periods, including the initial 20 bursts recorded prior to beginning synaptic perturbations as well as the periods between those cycles that received artificial synaptic input. (Note that P may be slightly different from P_{init} due to the inclusion in the average of the burst periods between perturbed periods.) As in the model neuron database, the ith phase response was calculated with the formula $(P_i' - P)/P$, where P_i' is the length of the perturbed period. The time at which the first spike in a burst crossed a user-defined threshold (usually approximately -30 mV) was defined as the reference point where the phase equaled zero.

In certain cases, the neuron would generally burst consistently but had transitory intervals of unusually slow or fast activity. Burst periods that were greater or less than 2.5 times the absolute deviation around the median (Leys et al. 2013) were considered outliers and were excluded from the analysis. Any phase responses that were measured during (or one period length before or after) these outlier intervals were similarly excluded. All PRCs and voltage traces were also visually examined for outliers; any outliers that occurred as a result of unusual PD activity (such as neuromodulatory events that caused a failure to spike), as a rare failure of the algorithm to properly detect the perturbed period, or as a result of artifacts in the voltage trace were removed.

We statistically determined whether each membrane conductance significantly affected the PRC by finding the "extra sums of squares" (Draper and Smith 1981; Sober and Sabes 2003). This technique is used to measure the reduction of the residual sum of squares when a particular variable (or variables) is added to a regression model. The data are fit using a reduced model (R), which does not include the set of additional variables, and a full model (F), which includes all variables. An F-test is then used to determine whether the additional variable (or variables) is significantly predictive of the output. We fit each set of PRCs to these two polynomial regression models, defining the phase response as the output (Y_i) and the stimulus phase and membrane conductance levels as predictors X_{i1} and X_{i2}, respectively. The reduced model only includes the stimulus phase X_{i1} as a predictor and is defined with the following equation:

$$Y_i = \beta_0 + \beta_1 X_{i1} + \beta_2 X_{i1}^2 + \beta_3 X_{i1}^3 + \varepsilon$$

where β is a vector of parameters and ε is a vector of errors. The full model includes both the stimulus phase X_{i1} and membrane conductance X_{i2} levels as predictors and is defined with the following equation:

$$Y_i = \beta_0 + \beta_1 X_{i1} + \beta_2 X_{i1}^2 + \beta_3 X_{i1}^3 + \beta_4 X_{i2} + \varepsilon$$

The relationship between the phase response and the stimulus phase is assumed to follow a cubic polynomial, and the relationship between the phase response and the membrane conductance level is assumed to be linear. For the purposes of statistically determining effects of conductances on the PRC shape, any points on the PRC that occurred as a result of a "missed cycle" (Oprisan et al. 2004) were not included in the cubic fit. To determine significant differences between PRCs, a Bonferroni correction was applied; the critical value for each conductance was based upon the number of tests that were performed for that conductance. This analysis was performed in MATLAB by adapting code that was written and graciously provided by Dr. Samuel J. Sober (Emory University).

3.2.9 Four-compartment model

To determine how the locations of specific ion channels influence their effect on the PRC, we modified an existing multi-compartment model described in (Maran et al. 2011). This model consists of four compartments that simulate: (1) the soma of one PD neuron, (2) a PD primary neurite, (3) a PD axon, and (4) the fine dendrites of both PDs and the AB neuron. To determine the effect of the leak current location within the four-compartment model on the PRC shape, $\bar{g}_{\text{leak}}$ for either: (a) the soma compartment alone ($\bar{g}_{\text{leak,soma}}$), or (b) each of the four compartments ($\bar{g}_{\text{leak,soma}}$, $\bar{g}_{\text{leak,primneur}}$, $\bar{g}_{\text{leak,axon}}$, $\bar{g}_{\text{dend}}$) was altered to take on a value of 0%, 33%, 67%, 100%, 133%, 167%, or 200% of its original value. The original, published version of the model does not include an H current. Thus, to determine the effect of the H current location within the four-compartment model on the PRC shape, we created two new versions of the model, one that had a model H current added to the soma compartment, and another that had a model H current added to the fine dendritic compartment (Figure 20). The H current was identical to that used to construct the model neuron database (Prinz et al. 2003a) and was based on experimental studies from (Huguenard and McCormick 1992).

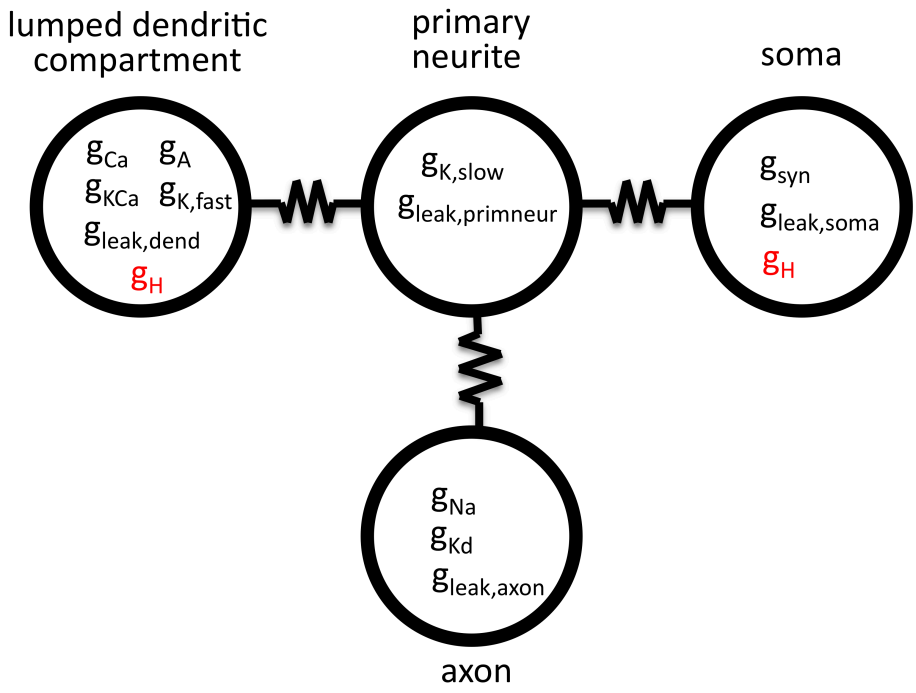

Figure 20. Four-compartment model of the pacemaker kernel. To investigate the effect of leak current location on the PRC, the leak current was altered in either all four compartments or in the soma compartment alone of a model from Maran et al. (2011). To investigate the effect of H current location on the PRC, two versions of the model were constructed in which $\bar{g}_H$ (shown in red) was either added to the lumped dendritic compartment *or* the soma compartment.

3.3 Results

3.3.1 Specific conductances have varying effects on PRC shape in PD-like burster populations

All PRCs tabulated in this study were Type II (Hansel et al. 1995); each PRC had a regime in which the subsequent burst was advanced by an inhibitory stimulus and another regime in which the subsequent burst was delayed.

Figures 21-23 demonstrate that the eight conductances of the single-compartment model have varying effects on the PRCs in the PD-like burster populations. Figure 21 shows eight sets of six histograms; each set corresponds to a specific conductance $\bar{g}_x$, and each histogram within the set indicates the distribution of the maximum phase response

for all PD-like bursters with a specific value for maximal conductance $\bar{g}_x$. The histograms indicate that the maximum phase response is generally reduced in PD-like burster populations with successively greater values of $\bar{g}_{leak}$. A similar effect is seen as $\bar{g}_H$ is increased. The calcium conductances $\bar{g}_{CaT}$ and $\bar{g}_{CaS}$, the calcium-dependent conductance $\bar{g}_{KCa}$, and the relatively fast-activating currents associated with $\bar{g}_{Na}$, $\bar{g}_{A,}$ and $\bar{g}_{Kd}$ have weaker effects on the distribution of the maximum phase response than do $\bar{g}_H$ and $\bar{g}_{leak}$.

Histograms in Figure 22 indicate that the neutral phase point generally increases in PD-like burster populations with successively greater values of $\bar{g}_H$ and $\bar{g}_{leak}$. Similarly, Figure 23 demonstrates that the PD-like burster populations exhibit decreasing minimum phase responses as $\bar{g}_H$ and $\bar{g}_{leak}$ increase.

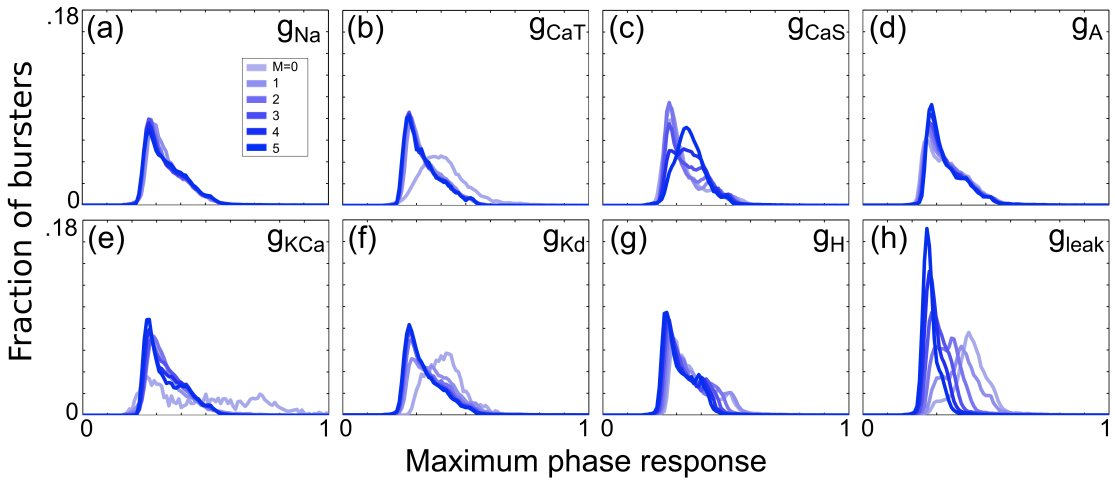

Figure 21. Conductances have varying effects on the maximum phase response by type. Histograms (bin width = 0.01) of the PRC maximum phase response were generated for 6 subpopulations of the 292,313 bursters that were analyzed. Subpopulations were created by constraining one of the 8 conductances to one of its 6 possible values. Histograms for each of the 8 sets of 6 subpopulations are plotted in (a-h) for the maximal conductances $\bar{g}_{Na}$, $\bar{g}_{CaT}$, $\bar{g}_{CaS}$, $\bar{g}_{A,}$ $\bar{g}_{KCa}$, $\bar{g}_{Kd}$, $\bar{g}_H$, and $\bar{g}_{leak}$, respectively.

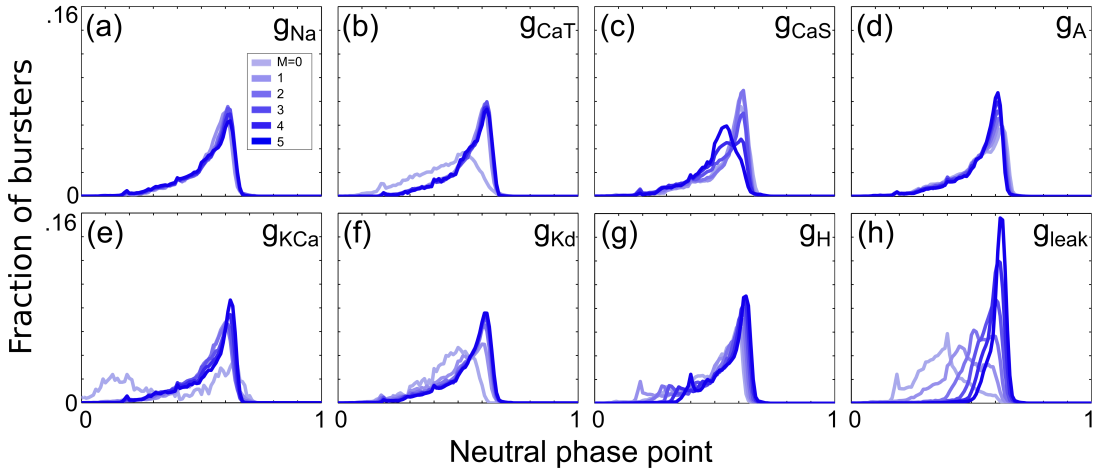

Figure 22. Conductances have varying effects on the neutral phase point by type. Histograms (bin width = 0.01) of the PRC neutral phase point were generated for 6 subpopulations of all analyzed bursters. Subpopulations were created by constraining one of the 8 conductances to one of its 6 possible values. Histograms for each of the 8 sets of 6 subpopulations are plotted in (a-h) for the maximal conductances $\bar{g}_{Na}$, $\bar{g}_{CaT}$, $\bar{g}_{CaS}$, $\bar{g}_{A}$, $\bar{g}_{KCa}$, $\bar{g}_{Kd}$, $\bar{g}_{H}$, and $\bar{g}_{leak}$, respectively.

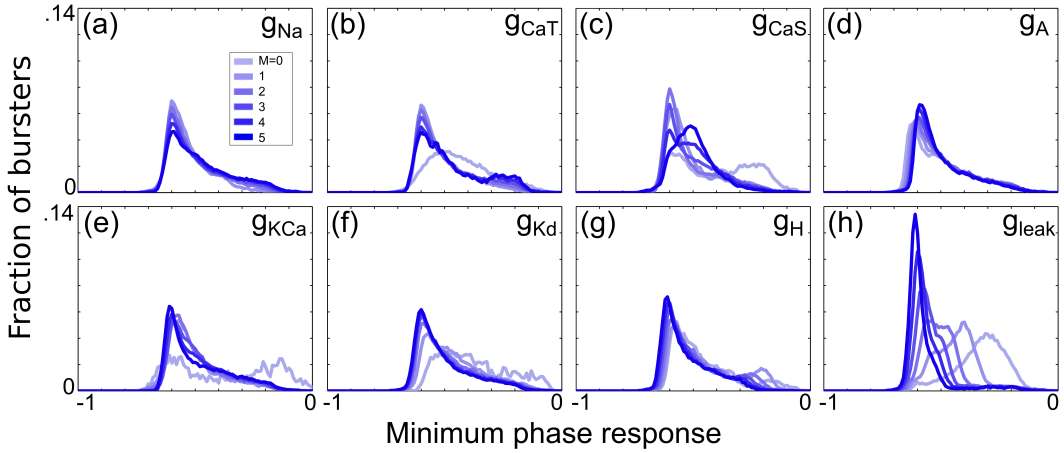

Figure 23. Conductances have varying effects on the minimum phase response by type. Histograms (bin width = 0.01) of the PRC minimum phase response were generated for 6 subpopulations of all analyzed bursters. Subpopulations were created by constraining one of the 8 conductances to one of its 6 possible values. Histograms for each of the 8 sets of 6 subpopulations are plotted in (a-h) for the maximal conductances $\bar{g}_{Na}$, $\bar{g}_{CaT}$, $\bar{g}_{CaS}$, $\bar{g}_{A}$, $\bar{g}_{KCa}$, $\bar{g}_{Kd}$, $\bar{g}_{H}$, and $\bar{g}_{leak}$, respectively.

The sensitivities of the PRC attributes to each of the eight conductances are summarized in Figure 24. The PD-like bursters in the model neuron database were most sensitive to the $\bar{g}_{\mathrm{H}}$ and $\bar{g}_{\mathrm{leak}}$ conductances. The negative sensitivity of the maximum and minimum phase responses to $\bar{g}_{\mathrm{H}}$ and $\bar{g}_{\mathrm{leak}}$, and the positive sensitivity of the neutral phase point to $\bar{g}_{\mathrm{H}}$ and $\bar{g}_{\mathrm{leak}}$, indicate that the entire PRC advances as either of these conductances is increased. In terms of the oscillator's activity, this means that the burst occurring immediately after the input perturbation is likely to occur sooner when greater amounts of I_{H} and I_{leak} are present in the model neuron.

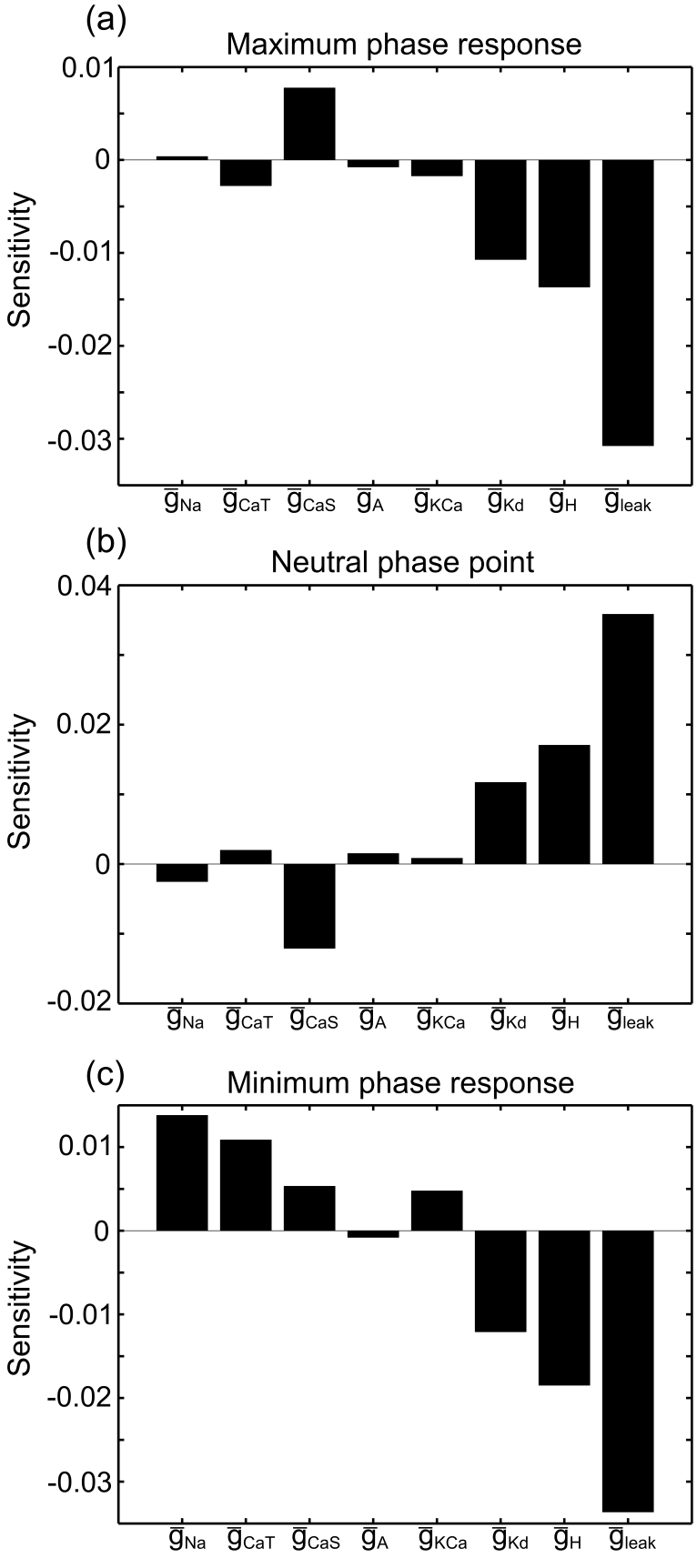
(a)
Maximum phase response
0.01
0
-0.01
-0.02
-0.03
Sensitivity
$\bar{g}_{Na}$ $\bar{g}_{CaT}$ $\bar{g}_{CaS}$ $\bar{g}_{A}$ $\bar{g}_{KCa}$ $\bar{g}_{Kd}$ $\bar{g}_{H}$ $\bar{g}_{leak}$
(b)
Neutral phase point
0.04
0.02
0
-0.02
Sensitivity
$\bar{g}_{Na}$ $\bar{g}_{CaT}$ $\bar{g}_{CaS}$ $\bar{g}_{A}$ $\bar{g}_{KCa}$ $\bar{g}_{Kd}$ $\bar{g}_{H}$ $\bar{g}_{leak}$
(c)
Minimum phase response
0.01
0
-0.01
-0.02
-0.03
Sensitivity
$\bar{g}_{Na}$ $\bar{g}_{CaT}$ $\bar{g}_{CaS}$ $\bar{g}_{A}$ $\bar{g}_{KCa}$ $\bar{g}_{Kd}$ $\bar{g}_{H}$ $\bar{g}_{leak}$

Figure 24. PRCs appear most sensitive to the leak conductance. Sensitivity plots show the sensitivity of the PRC attributes (a) maximum phase response, (b) neutral phase point, and (c) minimum phase response to the maximal conductances $\bar{g}_{\mathrm{Na}}$, $\bar{g}_{\mathrm{CaT}}$, $\bar{g}_{\mathrm{CaS}}$, $\bar{g}_{\mathrm{A}}$, $\bar{g}_{\mathrm{KCa}}$, $\bar{g}_{\mathrm{Kd}}$, $\bar{g}_{\mathrm{H}}$, and $\bar{g}_{\mathrm{leak}}$.

3.3.2 Specific conductances have varying effects on PRC shape in families of PD-like bursters

In addition to examining the effect of conductances on the PRCs of burster populations, we examined their effect on burster "families," which we define as sets of bursters for which seven of the eight conductances are constrained to one value and the final conductance value is allowed to vary. Figure 25 shows two examples of distributions of minimum phase response sensitivities within burster families to the conductances $\bar{g}_{\mathrm{Na}}$ and $\bar{g}_{\mathrm{leak}}$. While the median sensitivity of the minimum phase response to $\bar{g}_{\mathrm{Na}}$ is near zero (Fig. 25a), there exist both families in which increasing $\bar{g}_{\mathrm{Na}}$ reduces the minimum phase response (Fig. 25b) and families in which increasing $\bar{g}_{\mathrm{Na}}$ increases the minimum phase response (Fig. 25c).

The median sensitivity of the minimum phase response to $\bar{g}_{\mathrm{leak}}$ was the strongest of the eight conductances (Fig 25d); most PRC families' minimum phase responses were reduced as $\bar{g}_{\mathrm{leak}}$ increased (Fig 25e). Notably, there still existed several examples of PRC families that had positive sensitivities to $\bar{g}_{\mathrm{leak}}$ (Fig. 25f).

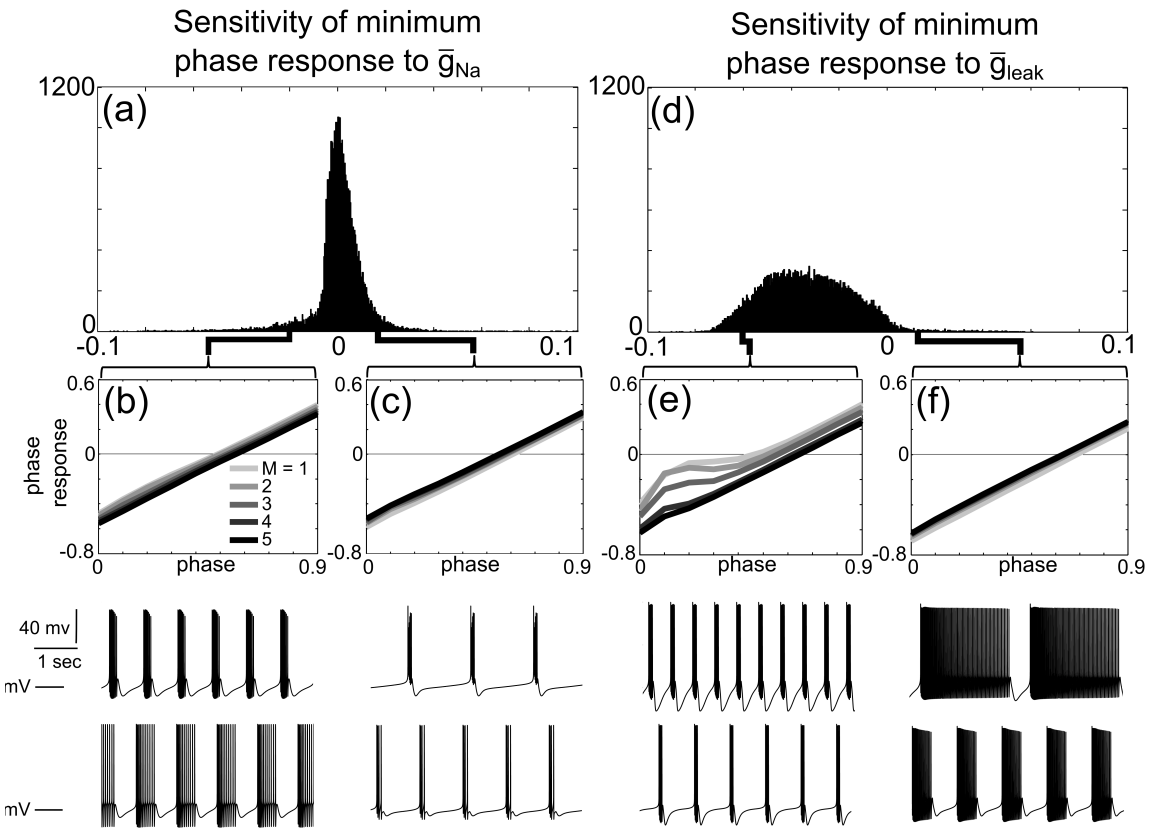

Figure 25. Conductances can either increase or reduce the PRC minimum phase response. (a) Histogram of sensitivities of minimum phase response of PRC families to $\bar{g}_{Na}$. (b) Example of a five-member PRC family with minimum phase responses that decrease with increasing $\bar{g}_{Na}$. All PRC family members are shaded from light to dark, with the lightest PRC having the lowest $\bar{g}_{Na}$ value and the darkest PRC having the highest $\bar{g}_{Na}$ value. $\bar{g}_{Na}$ values of the model neurons corresponding to each PRC are given by multiplying the integer M by 100 mS/cm^2. The spontaneous activity patterns of the model neurons with the smallest (M=1) and largest (M=5) maximal $\bar{g}_{Na}$ values in the family are shown below the PRCs. Maximal conductance values for M=1 model (in mS/cm^2): Na 100, CaT 2.5, CaS 2, A 10, KCa 5, Kd 125, H 0.03, leak 0.01. Maximal conductance values for M=5 model: Na 500, other conductances the same as for M=1 model. (c) Example of a five-member PRC family with minimum phase responses that increase with increasing $\bar{g}_{Na}$. Maximal conductance values for M=1 model (in mS/cm^2): Na 100, CaT 2.5, CaS 2, A 40, KCa 5, Kd 25, H 0.02, leak 0.02. Maximal conductance values for M=5 model: Na 500, other conductances the same as for M=1 model. (d) Histogram of sensitivities of minimum phase responses of PRC families to $\bar{g}_{leak}$. (e) Example of a five-member PRC family with minimum phase responses that decrease with increasing $\bar{g}_{leak}$. $\bar{g}_{leak}$ values of the model neurons corresponding to each PRC are given by multiplying the integer M by 0.01 mS/cm^2. The spontaneous activity patterns of the model neurons with the smallest (M=1) and largest (M=5) maximal $\bar{g}_{leak}$ values in the family are shown below the PRCs. Maximal conductance values for M=1 model (in mS/cm^2): Na 500, CaT 2.5, CaS 6, A 10, KCa 20, Kd 50, H 0.05, leak 0.01. Maximal conductance values for M=5 model: leak 0.05, all other conductances the same as for M=1 model. (f)

Example of a five-member PRC family with minimum phase responses that increase with increasing $\bar{g}_{\text{leak}}$. Maximal conductance values for M=1 model (in mS/cm^2): Na 200, CaT 2.5, CaS 10, A 40, KCa 10, Kd 100, H 0.01, leak 0.01. Maximal conductance values for M=5 model: leak 0.05, all other conductances the same as for M=1 model.

Figure 26 shows the sensitivities of PRC attributes to conductances for all families of PD-like bursters with at least three members. The sensitivities of the median families to each conductance are qualitatively similar to the sensitivities of the burster populations to each conductance (Figure 24). Notably, the effect of any specific conductance on the PRC families is highly variable: Examples of PRC families with both negative *and* positive sensitivities existed for each of the eight conductances, as well as for all three PRC attributes.

Examining the PRC families suggests that one cannot precisely predict the magnitude, or even the direction, of the sensitivity of a particular PRC attribute to a specific conductance without considering the model neurons' locations in conductance space.

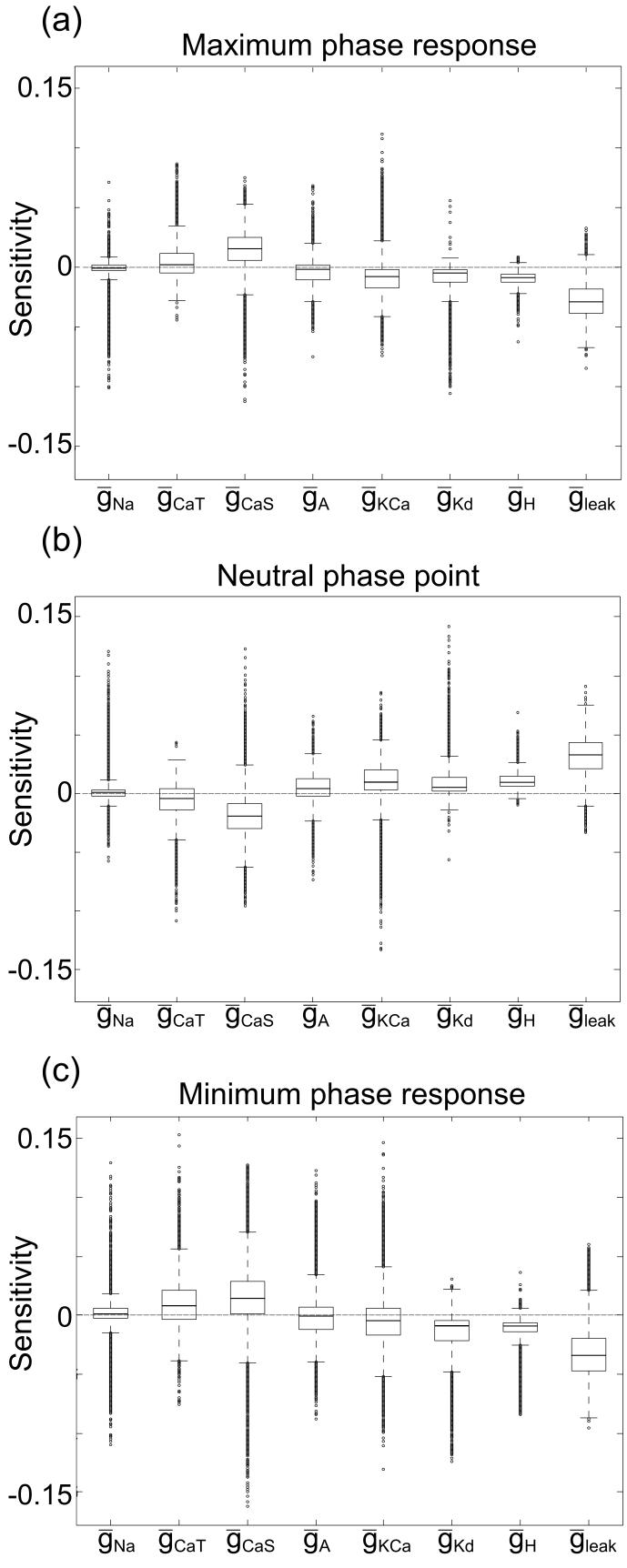
(a)
Maximum phase response
0.15
0
-0.15
Sensitivity
$\bar{g}_{Na}$ $\bar{g}_{CaT}$ $\bar{g}_{CaS}$ $\bar{g}_{A}$ $\bar{g}_{KCa}$ $\bar{g}_{Kd}$ $\bar{g}_{H}$ $\bar{g}_{leak}$
(b)
Neutral phase point
0.15
0
-0.15
Sensitivity
$\bar{g}_{Na}$ $\bar{g}_{CaT}$ $\bar{g}_{CaS}$ $\bar{g}_{A}$ $\bar{g}_{KCa}$ $\bar{g}_{Kd}$ $\bar{g}_{H}$ $\bar{g}_{leak}$
(c)
Minimum phase response
0.15
0
-0.15
Sensitivity
$\bar{g}_{Na}$ $\bar{g}_{CaT}$ $\bar{g}_{CaS}$ $\bar{g}_{A}$ $\bar{g}_{KCa}$ $\bar{g}_{Kd}$ $\bar{g}_{H}$ $\bar{g}_{leak}$

Figure 26. The sensitivity of PRC families to specific conductances varies throughout conductance space. (a) Box plots indicating the spread of the sensitivities for all families of PRCs for "PD-like" model neurons. The bold, central lines in each box plot indicate the median sensitivity of the minimum phase response to each conductance. The lower and upper edges of each box indicate the 25^{th} and 75^{th} percentiles, respectively, and the whiskers (dashed black lines) extend to the furthest data points that are within 1.5 times the interquartile range (the difference between the 75^{th} percentile and the 25^{th} percentile). All data points beyond 1.5 times the interquartile range are indicated as open ovals. Both negative and positive sensitivities exist for all conductances.

3.3.3 Dynamic-clamp-injected H conductance regularizes and advances the PRC in the isolated pacemaker kernel

The single-compartment model database provides a broad description of specific conductance effects on PRCs. Our results indicate that, within the conductance ranges spanned by the database, the specific conductances $\bar{g}_{\mathrm{H}}$ and $\bar{g}_{\mathrm{leak}}$ produce, on average, the effects of strongest magnitude on the PRC. In the biological PD neuron, certain ion channels associated with specific currents are found in distinct spatial regimes. This segregation of specific conductances may influence conductance effects on the PRC in a way that is not captured by the single-compartment model. We thus investigated the effects of $\bar{g}_{\mathrm{Na}}$, $\bar{g}_{\mathrm{A}}$, $\bar{g}_{\mathrm{Kd}}$, $\bar{g}_{\mathrm{H}}$, and $\bar{g}_{\mathrm{leak}}$ on a biological PRC by continuously injecting varying levels of these conductances into the PD neuron using the dynamic clamp, tabulating the PRCs at each conductance level, and determining whether the PRCs differed significantly from each other.

Adding increasing levels of $\bar{g}_{\mathrm{H}}$ to the PD neuron reliably caused the PRC to advance. In addition, the predictability of the phase response to consecutive stimulus phases was consistently increased. In other words, increasing $\bar{g}_{\mathrm{H}}$ reduced the error component in a low-order polynomial model of the PRC. Figure 27a shows one sample set of PRCs with varying $\bar{g}_{\mathrm{H}}$ tabulated using a stimulus duration proportional to the period. The PRC

taken while 0.5 μS $\bar{g}_H$ was injected into the PD neuron (shown in pink) exhibits more advanced phases (p = 0) and greater predictability than the PRC with 0 μS $\bar{g}_H$ injected (shown in black).

The addition of $\bar{g}_H$ produced a significant advancement of the PRC for all *n* under both types of stimuli tested, including a constant-duration 250 ms stimulus (n = 7) and a stimulus with a duration that was proportional to the intrinsic burst period (n = 4). Except in one case, all p-values were zero. Qualitatively, these experimental results are in agreement with the results from the model neuron database, which show that as $\bar{g}_H$ is increased in either a large population of PD-like bursters or in a set of PRC families, the PRC is most likely to advance.

The effect of increasing $\bar{g}_{leak}$ levels on the PD's PRC shape, in contrast, was inconsistent, lower in magnitude, and less significant than that of increasing $\bar{g}_H$. Figure 27b shows one of the four sets of PRCs with varying $\bar{g}_{leak}$, tabulated with a stimulus duration proportional to the period (p = .0003). While the PRCs within this set, taken with different levels of $\bar{g}_{leak}$, are significantly different from one another, no clear advance or delay of the curve is present. PRCs were significantly different in 2 of 7 animals using a constant stimulus duration and in 3 of 4 animals using a stimulus with a duration proportional to the intrinsic bursting period. The relatively weak effect of $\bar{g}_{leak}$ on the PRC is not consistent with the results from the single-compartment model neuron database, which had suggested that increasing $\bar{g}_{leak}$ would result in a larger advance than increasing the H conductance.

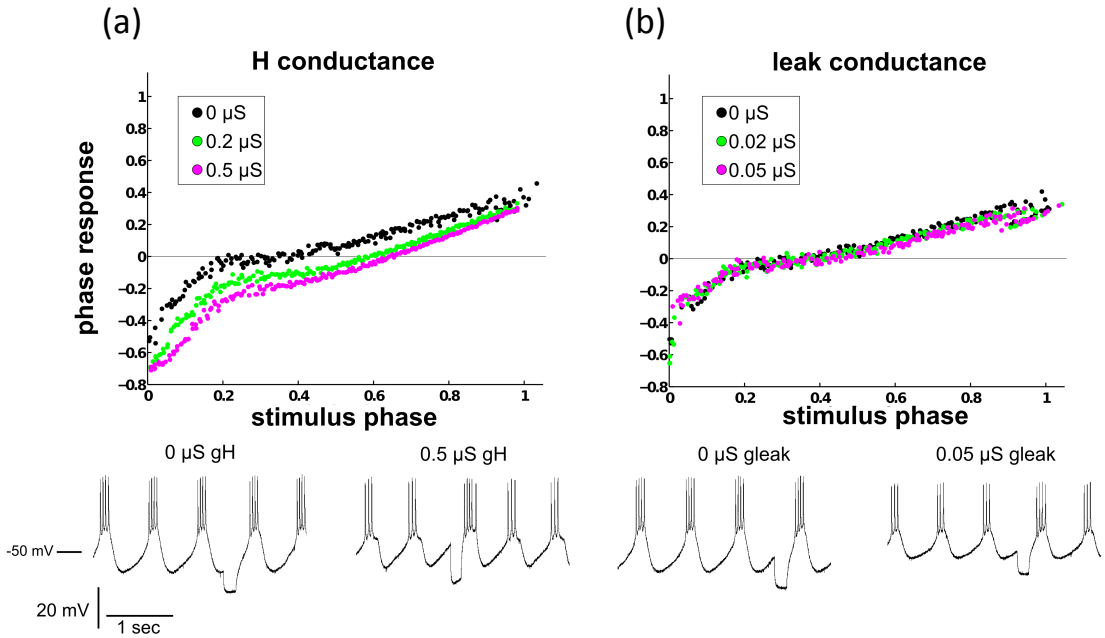

Figure 27. Dynamic-clamp-injected H current advances and regularizes the PRC. (a) As the H conductance is increased, the PRC is advanced and its variability is reduced. Voltage traces are shown for the lowest and highest levels of dynamic-clamp injected H current. In this example, $\bar{g}_{\mathrm{H}}$ was a significant factor in altering the PRC ($p = 0$). (b) Here, $\bar{g}_{\mathrm{leak}}$ was a significant factor in altering the PRC ($p = 0.0003$). However, the change in the phase response at any given stimulus phase as $\bar{g}_{\mathrm{leak}}$ is increased is relatively small. Voltage traces are shown for the lowest and highest levels of dynamic-clamp-injected leak current.

As with $\bar{g}_{\mathrm{leak}}$, $\bar{g}_{\mathrm{Na}}$, $\bar{g}_{\mathrm{A}}$, and $\bar{g}_{\mathrm{Kd}}$ exhibited relatively weak effects on the PRC. The effects of $\bar{g}_{\mathrm{A}}$ on the biological PRCs and the model PRCs were consistent with each other; in both cases, an effect was either weak or not present. However, the weak effects of $\bar{g}_{\mathrm{Na}}$ and $\bar{g}_{\mathrm{Kd}}$ in the biological neuron were again inconsistent with those from the single-compartment model neuron database, in which increasing $\bar{g}_{\mathrm{Na}}$ delayed the minimum phase response and $\bar{g}_{\mathrm{Kd}}$ advanced the entire PRC, though to a lesser degree than $\bar{g}_{\mathrm{H}}$ and $\bar{g}_{\mathrm{leak}}$. Results for all conductances tested are summarized in Table 1.

Table 1. Effects of dynamic-clamp-injecting conductances into PD neuron

	$\bar{g}_{Na}$		$\bar{g}_{A}$		$\bar{g}_{Kd}$		$\bar{g}_{H}$		$\bar{g}_{leak}$	
α	.005		.0055		.005		.0045		.0045	
Stim. Dur. (ms)	250	0.25**P*	250	0.25**P*	250	0.25**P*	250	0.25**P*	250	0.25**P*
Num. Sig.	1	0	0	1	3	0	7	4	2	3
n	5	5	5	4	5	5	7	4	7	4

The row "α" indicates the Bonferroni-corrected significance level used to determine whether each conductance type has a significant effect on PRC shape. For each *n*, the PRCs taken with varying levels of dynamic-clamp-injected conductances were considered statistically different from one another if the p-value was found to be less than α. The row "Stim. Dur. (ms)" indicates the duration of the stimulus pulse, which was either 250 ms or 25% the length of the intrinsic burst period P_{init}. The row "Num. Sig." indicates the number of experiments that showed significant differences between the PRCs for a particular conductance and stimulus type. The row "*n*" indicates the total number of experiments for a particular conductance and stimulus type.

3.3.4 Effects of $\bar{g}_H$ and $\bar{g}_{leak}$ on the PRC are dependent upon their location in a multi-compartment model

We were interested in further exploring the effects of $\bar{g}_{leak}$ and $\bar{g}_H$ on the PRC, given that these currents had the strongest effects on the PRC in the single-compartment model and have been shown elsewhere to have significant effects on the biological PRC (Prinz et al. 2003a; Prinz et al. 2003b). We suspected that the discrepancy between the effect of $\bar{g}_{leak}$ on PRCs in the model neuron database and its effect in the biological neuron partly arose from the fact that in the biological neuron, the locations of synaptic input, spike generation, and production of the voltage envelope are spatially separated. Injecting leak current solely into the soma may not adequately impact the mechanism that generates the slow-wave oscillation (Maran et al. 2011) and therefore may have little effect on the PRC. Conversely, in the single-compartment model neuron, all phenomena effectively occur at a single point in space. Thus, there is no attenuation of the leak current in the

single-compartment model, and it may therefore have a stronger effect on the PRC than it does in the biological neurons.

Since the H channels are commonly found in the neuropil rather than the soma of the PD biological neuron (Goeritz et al. 2011), similarly to other neuron types (Angelo and Margrie 2011), we also sought to determine whether increasing the H current in the neuropil would have a similar effect on the PRC as would increasing the H current in the soma (as was done with dynamic clamp injection).

We thus desired to resolve: (1) whether the discrepancy between $\bar{g}_{\text{leak}}$'s effects on the PRCs in the model and biological studies was indeed due to spatial segregation of the bursting mechanism and synaptic injection, and (2) whether the effect of $\bar{g}_{\text{H}}$ on the PRCs that we saw in both the model and biological studies would still be present if the H current was altered in the neuropil rather than in the soma. To investigate these questions, we further examined PRCs in a more biologically realistic, multi-compartment model.

We sought to determine whether altering the leak current solely in the soma (as is done when artificially adding currents to the PD neuron with dynamic clamp) has different effects on the PRC from altering the leak current throughout the entire pacemaker kernel (which we analogize to altering the leak current parameter in a single-compartment model). To do this, we utilized a four-compartment model from Maran et al. (2011). This model used multiple compartments to separate the location of synaptic input (soma), the location of spike generation (axon), and the location of the mechanisms underlying the production of the voltage envelope (lumped dendritic compartment).

We examined PRCs while altering: (1) $\bar{g}_{\text{leak}}$ in the soma compartment alone, and (2) $\bar{g}_{\text{leak}}$ in all compartments, including the soma, axon, primary dendrite, and lumped dendritic compartment. Modifying $\bar{g}_{\text{leak}}$ in the soma compartment alone had little effect on the PRC (Figure 28a), with most phase responses changing by < 0.01 as $\bar{g}_{\text{leak,soma}}$ was increased from 0% to 200% of its canonical value. Increasing $\bar{g}_{\text{leak}}$ to 4000% of its

canonical value, however, advanced the PRC, similarly to the model neuron database. Altering $\bar{g}_{\text{leak}}$ in every compartment from 0% to 200% of their canonical values had relatively strong effects on PRC shape (Figure 28b).

We see that doubling $\bar{g}_{\text{leak}}$ in the soma alone had almost no effect on the PRC, but doubling $\bar{g}_{\text{leak}}$ in every compartment had a substantial effect on PRC shape. This suggests that the lack of effect of the dynamic-clamp-injected leak current seen in the biological PRC may indeed be due to relatively weak electrical coupling between the dendritic compartment (where the slow wave is generated) and the soma (where synaptic inputs are applied).

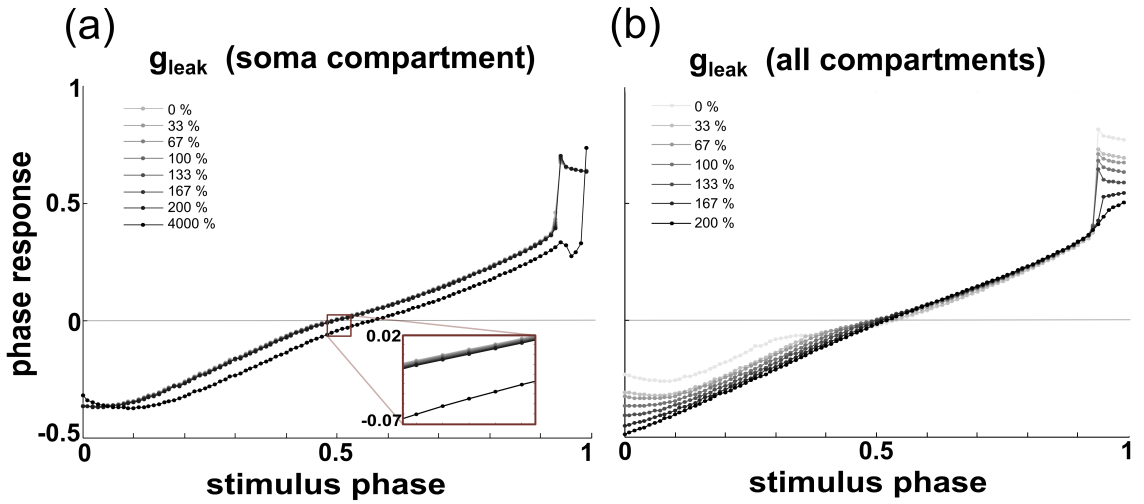

Figure 28. The leak current's effect on the PRC depends on its location in a 4-compartment model. (a) Altering $\bar{g}_{\text{leak}}$ in the soma compartment between 0% and 200% of its canonical value alters phase responses by less than 0.01. Increasing $\bar{g}_{\text{leak,soma}}$ to 4000% of its canonical value results in an advance of the PRC, an effect that is qualitatively similar to that seen in the single-compartment model neuron database when $\bar{g}_{\text{leak}}$ was increased by smaller increments. (b) Increasing $\bar{g}_{\text{leak}}$ in each compartment from 0% to 200% of its canonical value noticeably alters the PRC shape, decreasing both the minimum and maximum phase response.

We also sought to determine whether the location of the H current significantly affects its influence on the PRC. We added an H current (Huguenard and McCormick 1992) to either (1) the soma compartment or (2) the lumped dendritic compartment of the aforementioned four-compartment model. We then examined the effect of altering the

newly added H current on the PRC in both versions of the model. In the version of the model with the H current in the soma (which is the location at which we dynamic-clamp-injected the H current into the PD neuron), the phase responses advanced by approximately 0.06 as the H current was increased from 0% to 200% of its canonical value (Figure 29a). This result is qualitatively similar to that from the model neuron database and consistent with the results seen from the dynamic clamp studies. In the version of the model with the H current in the dendritic compartment, where the H channels exist in biological neurons, the phase responses generally advanced by less than 0.01 as $\bar{g}_{\mathrm{H}}$ was increased from 0 to 200% of its canonical value (Figure 29b).

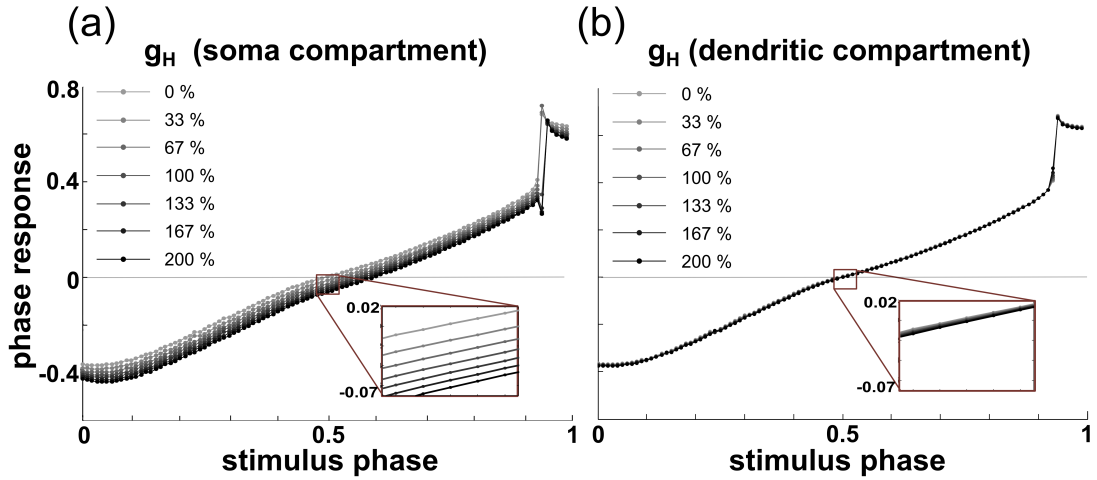

Figure 29. The H current's effect on the PRC depends on its location in a 4-compartment model. (a) Increasing $\bar{g}_{\mathrm{H}}$ in the soma compartment advances the entire PRC, similarly to the single-compartment model. As $\bar{g}_{\mathrm{H}}$ was increased from 0% to 200% of its canonical value, phases advanced by approximately 0.06. (b) Increasing $\bar{g}_{\mathrm{H}}$ in the lumped dendritic compartment from 0% to 200% of its canonical value caused phases to advance by approximately 0.01 or less.

The above results suggest that the strong advancing effect of the H current seen in both the single-compartment model and the dynamic-clamp studies is a result of both methods' simulating the H currents in a nonphysiological location. In both studies, the H currents are in the same compartment as that in which the synaptic current is received,

and this lack of spatial separation between the locations of slow-wave generation, spike generation, and synaptic input may again be exaggerating the effect of the H current.

We thus wanted to resolve whether the endogenous H current in the biological PD neuron has similar effects on the PRC to the dynamic clamp-injected H current. We additionally desired to know whether the regularizing effect of the injected H current was also produced by the endogenous H current. To investigate these questions, we recorded and compared PRCs before and after blocking endogenous H current in the PD neuron.

3.3.5 Phase response is delayed, and its predictability decreases, when I_H is blocked

We investigated whether altering the endogenous H current in the biological PD neuron via pharmacological blockade would have a differing effect on the PRC than the injection of artificial H current via dynamic clamp (Figures 30 and 31). Typical values for the endogenous H conductance of the PD neuron are near 0.01 to 0.05 μS (Temporal et al. 2012), approximately an order of magnitude lower than the level of H conductance injected into the soma using the dynamic clamp. Upon blocking the H conductance, the PD burst period increased and exhibited greater variability. We saw two notable effects of blocking the H current on the PRC of the PD neuron. PRCs exhibited small but significant *delays* in 1 of 2 animals when a 250 ms stimulus was applied and in 3 of 3 animals when a stimulus proportional to the intrinsic burst period was applied. In addition, the noisiness of the PRC consistently increased (in other words, the ability to predict the phase response for a particular phase stimulus with a cubic polynomial decreased) after the H current was blocked. As seen in previous studies, the effects of CsCl were rapidly reversible (Peck et al. 2001). The effect of blocking the H current on the PRC washed out in 2 of 3 cases, suggesting that the changes in the PRC were due to the addition of CsCl rather than other effects causing the PRC to change over time. Table 2 summarizes the results from all pharmacological experiments.

Table 2. Effect of blocking H current on the PRC.

	I_H Blocked	
α	0.01	
Stim. Dur. (ms)	250 ms	0.25*P
Num. Sig.	1	3
n	2	3

The row "α" indicates the Bonferroni-corrected significance level used to determine whether blocking the H current has a significant effect on PRC shape. For each *n*, the PRCs were considered statistically different from one another if the p-value was found to be less than α. The row "Stim. Dur. (ms)" indicates the duration of the stimulus pulse, and the row "Num. Sig." indicates the number of experiments that showed significant differences between the PRCs for each stimulus type. The row "*n*" indicates the total number of experiments for a particular stimulus type.

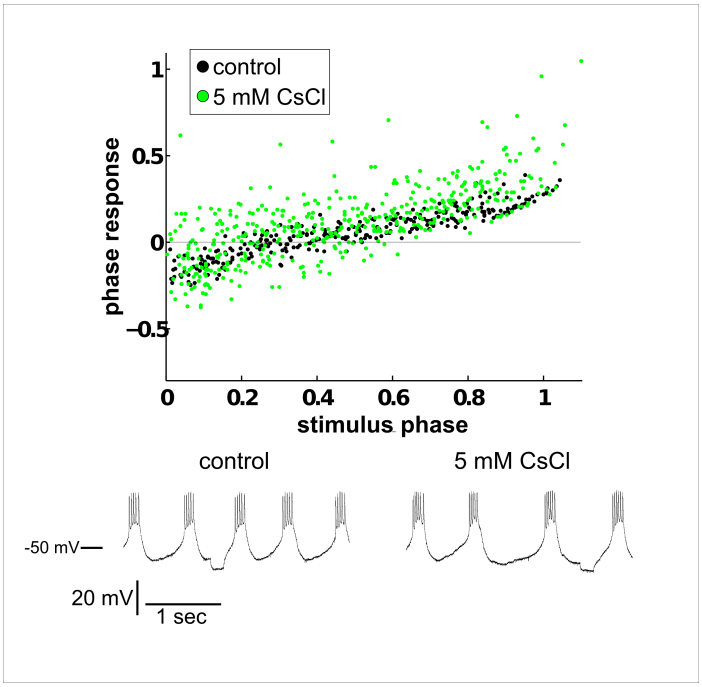

Figure 30. Pharmacological blockade of I_H increases noisiness in the PRC. Example set of PRCs tabulated before 5 mM CsCl was added to the PD neuron (shown in black) and afterward (shown in green). The noise in the PRC is increased when the H current is blocked. The mean squared error of the control PRC (when modeled with a cubic polynomial) is 0.0028, and that of the PRC with 5 mM CsCl is 0.0206. In this example, PRCs were tabulated using a stimulus with a duration proportional to the period.

To illustrate the quantitative difference between the PRCs taken with and without an active H current in the pacemaker kernel, Figure 31 shows a second example set of PRCs before and after pharmacological blockade overlaid by their respective cubic polynomial fits. The polynomial fit for the PRC taken after pharmacological blockade is delayed, and the error that is not accounted for by the fit is increased. In this example, the mean squared error of the control PRC is 0.0013, and that of the PRC with 5 mM CsCl is 0.0065, suggesting that the noisiness of the PRC has increased.

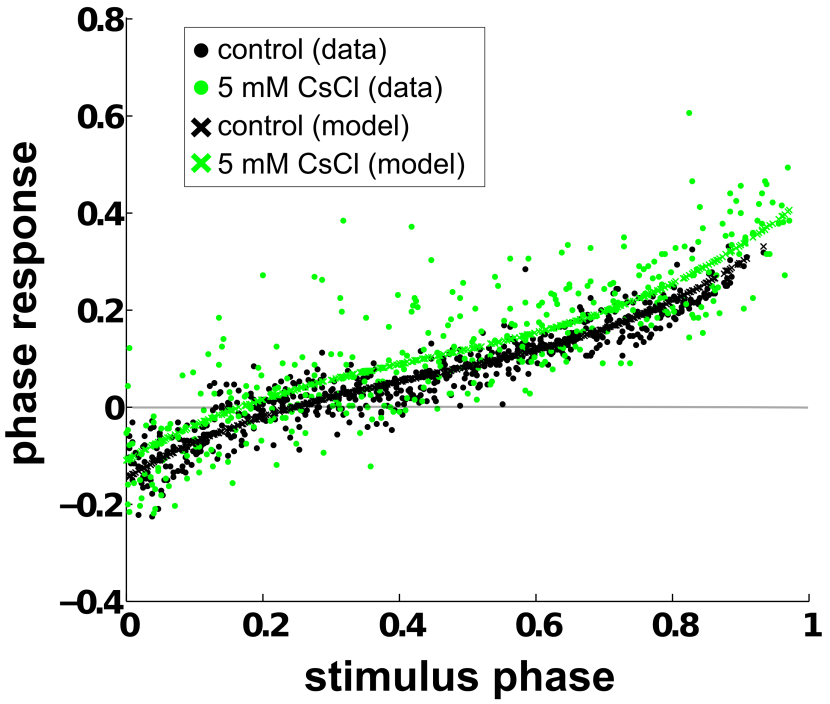

Figure 31. Pharmacological blockade of I_H delays the polynomial fit of the PRC. Example set of PRCs tabulated before 5 mM CsCl was added to the PD neuron (shown as black circles) and afterward (shown as green circles). The polynomial fits for the control and treated PRCs are shown as black and green 'x's, respectively. The polynomial fits indicate that the PRC is slightly delayed when the H current is blocked. Pharmacological blockade increases the mean squared error by a factor of approximately 5. PRCs were tabulated with a stimulus of 250 ms duration.

3.4 Discussion

The phase resetting curve is a convenient method to describe the effect of an input stimulus on a neuronal oscillator. The intrinsic parameters of the oscillator, including the maximal conductances of its membrane currents, have a profound influence on its activity type (Goldman et al. 2001; Hudson and Prinz 2010). We sought to determine whether these intrinsic membrane currents also produce specific effects upon the nature of the oscillator's response to synaptic input by computationally and experimentally examining the PRC of a well-characterized neuronal oscillator. In this study, we found that: (1) Specific conductances have varying effects on the PRC in a single-compartment model, with $\bar{g}_{\mathrm{H}}$ and $\bar{g}_{\mathrm{leak}}$ generally causing the PRC to advance, (2) both endogenous and dynamic-clamp-injected H current cause the PRC to advance, though this effect is exaggerated when the H current is injected into the soma (as is done in dynamic clamp), (3) $\bar{g}_{\mathrm{H}}$ increases predictability of the biological PRC when modeling it as a low order polynomial, and (4) the effects of $\bar{g}_{\mathrm{H}}$ and $\bar{g}_{\mathrm{leak}}$ on the PRC depend on their location in the pacemaker kernel.

3.4.1 PRCs in the single-compartment model neuron database

The analysis of PD-like burster populations in the model neuron database provides a synoptic view of the relationship between specific conductances and PRC shape. In particular, $\bar{g}_{\mathrm{H}}$ and $\bar{g}_{\mathrm{leak}}$ have average effects of the greatest magnitude on the PRC, both generally causing the entire curve to advance. The delayed rectifier conductance, $\bar{g}_{\mathrm{Kd}}$, has a similar effect, though to a lesser magnitude.

Previous studies exploring the effect of $\bar{g}_{\mathrm{H}}$ and $\bar{g}_{\mathrm{leak}}$ on the PRC have noted that their presence in a model neuron pacemaker does affect the nature of the response to synaptic input (Prinz et al. 2003b). Both currents cause the PRC to reach a "saturation point" at which it is no longer altered by further increasing the strength of the inhibitory synaptic input; without these currents, the model neuron's PRC does not saturate until the synaptic

input is strong enough to clamp V_m at the synaptic reversal potential. The leak current appears to affect PRC saturation more strongly than the H current (Prinz et al. 2003b). The fact that PRCs are more likely to saturate when the H currents and leak currents are present suggests that the PRCs of model neurons with large levels of leak and H currents may not be as sensitive to the other six conductances as would those PRCs of model neurons with low levels of leak and H currents. Our data suggest that this may be the case for the leak current: The minimum phase response histograms for varying levels of $\bar{g}_{leak}$ (Figure 23h) clearly indicate a greater negative shift in the mean minimum phase response between populations of model neurons with $\bar{g}_{leak}$ at levels M = 0 and M = 1 (the two lightest blue histograms) than between populations of model neurons with conductances at levels M = 4 and M = 5 (the two darkest blue histograms). A similar effect is seen in the maximum phase response (Figure 21h) and neutral phase point (Figure 22h). Within the ranges used to construct this database, $\bar{g}_{leak}$ may exhibit an effect on the PRC that overrides those of other currents.

The results from our examination of individual PRC families also compliment the findings from Prinz et al. (2003b) by indicating that when the synaptic strength is held constant and the conductance levels are varied (the converse of Prinz et al.'s protocol), the effects of increasing $\bar{g}_{leak}$ may also cause the PRC to saturate after a point. Figure 25e illustrates one family in which the differences between the PRCs at levels M = 4 and M = 5 are small compared to the PRCs in the same family with lower levels of leak current. This nonlinear relationship between the PRCs is not as evident in the families with altered gNa levels (Figure 25b, 25c).

Examining the PRC families' individual sensitivities to the conductances (Figure 26) indicates that although certain conductances may cause *most* PRCs to be shifted either positively or negatively (i.e. the middle quartile range of the sensitivities is entirely above or below zero, respectively), for all eight conductances and all three PRC attributes, there are cases of PRC families in which the PRCs are shifted positively, and other cases in

which the PRCs are shifted negatively, by increasing the value of one conductance. In other words, the effect of any specific conductance on the PRC cannot be determined without also examining the location of the respective model neuron in conductance space.

We have examined the general variability of three PRC attributes in PRC families throughout conductance space, but we have not attempted to determine whether there is a relationship between one conductance's effect on any particular PRC family and that PRC family's location within the other 7 dimensions of conductance space. The various sensitivities seen for each conductance in Figure 26 are likely not randomly distributed in conductance space. One possibility is that that the magnitude of the effect of any given conductance on the PRC is itself related to the total current produced by the other conductances, with any specific current producing an outsized effect on PRCs when all other currents are relatively small. Future work will explore this possibility. Another interesting avenue of exploration is whether certain pairs of conductances result in the preservation of PRC shape. Several studies have demonstrated that parameters at the mRNA (Schulz et al. 2007; Tobin et al. 2009), cellular (Ball et al. 2010; Hudson and Prinz 2010; Soofi et al. 2012), and synaptic (Goaillard et al. 2009) levels exhibit pairwise correlations within solution spaces. Examining whether pairwise correlations also preserve PRC shape is a natural extension of these studies, since the PRC provides a functional view of the neuron's role in determining network-level output.

3.4.2 Conductance location is a determinant of PRC shape

We used the dynamic clamp to examine the effects of specific conductances on PRC shape. We investigated five separate conductances but focused on $\bar{g}_{\mathrm{H}}$ and $\bar{g}_{\mathrm{leak}}$. These two currents were of particular interest because: (1) They are generally active over the entire burst period and therefore likely to affect the general shape of the PRC, which covers all phases of the burst cycle, (2) The single-compartment model neuron database indicated that they generally had the effect of highest magnitude on the PRC out of all

currents, and (3) These two currents influence the PRC's sensitivity to synaptic strengths (after the strength is increased beyond a certain level) (Prinz et al. 2003b).

We saw two major effects of increasing $\bar{g}_{\mathrm{H}}$ in the soma of the PD neuron: The PRCs advanced, and the noisiness of the PRC was reduced. That the PRC advances is a sensible result; the H current is activated by hyperpolarization, so higher levels of $\bar{g}_{\mathrm{H}}$ will result in more inward current in response to a strong hyperpolarizing pulse, resulting in a neuron that is more likely to burst immediately following perturbation. Unexpectedly, we saw inconsistent and weak effects of increasing $\bar{g}_{\mathrm{leak}}$ on the PRC. We investigated whether the spatial separation of slow-wave generation, spike generation, and input location in the biological PD neuron played a role in producing the discrepancy between the database and dynamic clamp results by examining the four-compartment model. This model was developed with a goal of reproducing biological PRCs in the pacemaker kernel of the pyloric circuit and is thus suited to exploring the effects of conductance location and magnitude on inhibitory PRCs (Maran et al. 2011). This model was previously used to demonstrate that the spatial separation of the mechanisms generating different aspects of the burst waveform (i.e. the slow wave and the spikes) plays an important role in shaping the PRC. Our findings indicate that conductance locations and magnitudes are crucial determinants of PRC shape, too. If we concentrate additional leak current in the soma compartment alone, we achieve a very different PRC shape than if we increase the general leakiness of the entire model neuron.

Much work has been done in the stomatogastric nervous system to understand how the myriad factors in complex neuronal networks affect the activity of a single neuron or the neuronal network as a whole. The converse problem – predicting how specific details of neuronal activity will translate to effects on network function – is difficult, and results are often nonintuitive. Brute-force techniques for determining neuronal (Golowasch et al. 2002; Prinz et al. 2003a; Taylor et al. 2009) and network (Doloc-Mihu and Calabrese 2011; Prinz et al. 2004b) output have emerged, in part, as a result of the difficulty in

predicting output from a set of inputs with nonlinear voltage dependence. In order to obtain an accurate picture of how a biological neuron's activity will influence network-level function, the initial neuron model and its ion channel distributions should thus be judiciously chosen.

Previous work has suggested that the H current has similar effects on the phase resetting curve as the leak current (Prinz et al. 2003b); this was used as justification for not including the H current in the four-compartment model described in Maran et al. (2011). Our results show that this is not the case; the H current and leak current have distinguishable effects on the PRC, and these effects are partly dependent on conductance location. Thus, both currents should be included in future models that are used to predict neuronal responses to synaptic input, and their locations within the model should be biologically motivated.

3.4.3 Effect of the H current on neuronal and network-level activity

Taken together, the experimental and modeling results involving manipulation of $\bar{g}_{\mathrm{H}}$ suggest that:

(1) The endogenous H current in the neuropil, when present, causes the PRC to advance slightly. Control PRCs are, on average, more advanced than those taken while the H current is blocked; additionally, adding H to the neuropil compartment of a pacemaker model results in a slight phase advance of less than 0.01.

(2) The endogenous H current in the neuropil, when present, increases the predictability of the PRC (see Figs. 30 and 31). The mean squared errors of the PRCs taken with CsCl were greater than those of the control PRCs when both were modeled with a cubic polynomial.

(3) The dynamic-clamp-injected H current has both an advancing and regularizing effect on the PRC (as does the endogenous current), but the effects are stronger than those of the endogenous current. The significance of the differences between the control

PRCs and those that were dynamic-clamp-injected with H current was generally greater (i.e. the p-value was lower) than the significance of the differences between the control PRCs and those that had the intrinsic H current blocked with CsCl. These exaggerated effects of the dynamic clamp-injected $\bar{g}_H$ may be due to two factors: (i) We injected greater levels of H current into the cell than is endogeneously present, and (ii) We injected H current into the soma, where it is not usually found in the biology; our results from the four-compartment model suggest that the PRC is more strongly advanced when the H current is modeled in the soma than in the dendrites where the I_H channels are endogenously located.

A notable deficiency in the four-compartment model is that since it does not include noise, we cannot ascertain whether the noisiness of the model PRC is also reduced with increasing levels of I_H. We will investigate this question in future work by adding Gaussian noise to the underlying current of the previously described four-compartment model. We can then use this model to explore whether the location of the H current influences the ability of the current to reduce noise, as well as advance the PRC.

A hyperpolarization-activated current is found in many neuron types (Angelo et al. 2007; Aponte et al. 2006; Dai et al. 2010), and its role has been examined at both the single-neuron (Ouyang et al. 2007) and network (Tohidi and Nadim 2009) levels. Angelo et al. (2011) has reported that mitral cells with high levels of I_H current exhibited greater spiking regularity (i.e. ISIs exhibited a lower CV) than did cells treated with ZD7288, an I_H blocker. This "deregularizing" effect of blocking I_H is consistent with our findings in PD. The level of I_H in a pacemaker neuron may also influence network-level activity: (Ermentrout et al. 2012) suggested that a higher level of I_H in a Golomb and Amitai conductance-based model of a two-cell network with reciprocal connections increases network synchrony (Golomb and Amitai 1997). In addition, the level of H current in the pacemaker kernel of the pyloric rhythm is correlated with overall pacemaker activity (Tohidi and Nadim 2009). Our report that the H current exhibits a regularizing effect on

the response to synaptic input thus aligns with reports from other studies that suggest the H current promotes stable or synchronous activity.

3.5 Acknowledgements

We gratefully acknowledge Wanlu Hu for her initial work on this project, Prof. Wolfgang Stein for verifying a subset of our results (Marine Biological Laboratory, Woods Hole, MA), Dr. Marie Goeritz for helpful discussion of experimental protocols, and Prof. Samuel J. Sober for helpful discussions about statistical analysis. This work was funded by an NSF IGERT Fellowship (WS), an NSF GRF (WS), and an NIH grant R01NS054281 (PI: C. Canavier).

CHAPTER 4

PHASE MAINTENANCE IN A RHYTHMIC MOTOR PATTERN DURING TEMPERATURE CHANGES *IN VIVO*

The majority of this chapter was submitted for publication to the *Journal of Neurophysiology* (American Physiological Society) in December 2013 under the name "Phase maintenance in a rhythmic motor pattern during temperature changes *in vivo*." Authors on the submitted manuscript were: Wafa Soofi, Marie L. Goeritz, Astrid A. Prinz, Eve Marder, Wolfgang Stein. Soofi and Goeritz contributed equally to the work. All *Cancer pagurus* data was collected by Soofi, and all *Cancer borealis* data was collected by Goeritz. Data was analyzed by Soofi and Goeritz, and the original manuscript was written by Soofi. All authors contributed to editing the manuscript. Minor revisions were suggested by the reviewers; a subset of these revisions has been included in the following text. A version of the manuscript with all revisions included was accepted in March 2014. Authors on the accepted version of the manuscript were: Wafa Soofi, Marie L. Goeritz, Tilman J. Kispersky, Astrid A. Prinz, Eve Marder, Wolfgang Stein.

4.1 Introduction

Every animal's nervous system must be able to function throughout life despite constant molecular turnover, developmental changes, and environmental perturbations. A notable challenge to the nervous systems of poikilotherms is the fluctuation in the ambient temperature, which causes corresponding fluctuations in body temperature. The voltage-dependent gating dynamics of the ion channels controlling synaptic and intrinsic membrane currents exhibit varying degrees of temperature dependence (Cao and Oertel 2005; Moran et al. 2004; Myers et al. 2009; Thompson et al. 1985), potentially leading to large variations in neuronal activities. Yet, the many components of poikilotherm nervous

systems work in concert and produce functional activity at a wide range of temperatures (Robertson and Money 2012; Tang et al. 2010).

The poikilotherm *Cancer borealis* inhabits the waters stretching from Florida to Nova Scotia (Haefner 1977; Rathbun 1930). It is most commonly found at depths of 61-400 meters (Haefner 1977) and at temperatures between 8 and 14°C (Haefner 1977; Stehlik et al. 1991), but it also frequents the inter-tidal and sub-tidal zones (Donahue et al. 2009; Rathbun 1930) to forage for food (Krediet and Donahue 2009). In these shallower waters, temperatures can reach nearly 24°C (Krediet and Donahue 2009). *Cancer pagurus*, a species closely related to *C. borealis*, is ordinarily found in the North Sea at temperatures between 4°C and 15°C; however, it will regularly recover from exposure to temperatures of up to 19°C in open air during commercial shipment (Barrento et al. 2010; Metzger et al. 2007). In order for the animals to feed properly, their nervous systems must retain functionality at temperatures that span these ranges.

Central pattern generators (CPGs) are a class of neuronal circuits that generate cyclic patterns controlling rhythmic behaviors such as breathing, locomotion, saccadic eye movements, vocalizations, and chewing (Berkowitz et al. 2010; Büschges et al. 2011; Chevallier et al. 2008; Doi and Ramirez 2008; El Manira et al. 2010; Harris-Warrick 2011; Katz 2007; Kiehn 2006; Marder and Calabrese 1996; Yamaguchi et al. 2008). Due to the predictability of their output under control conditions, CPGs are a convenient test bed for studying the effects of temperature perturbations on neuronal motor output. Certain features of CPG output, such as the cycle frequency, may vary widely (Tang et al. 2010); other features, such as the relative timing (i.e. phase relationships) of bursts or spikes within the rhythm, remain rather constant (Bucher et al. 2005; Cohen et al. 1992; Hooper 1997a; Skinner and Mulloney 1998; Soofi et al. 2012). Presumably, constraining these features is necessary for retaining functional behavior. The stomachs of decapod crustaceans such as *C. borealis* and *C. pagurus* are controlled by two CPGs, one of which is the pyloric circuit, which produces the pyloric rhythm and drives the musculature of

the pyloric filter. *In vitro*, the phase relationships of the neurons in the pyloric rhythm remain remarkably constant as the pyloric frequency changes (Bucher et al. 2005; Hooper 1997a; 1997b), indicating that phase maintenance is important for the filtering of food. Accomplishing this phase maintenance is nontrivial, requiring precise compensation of active conductances, synaptic dynamics, and other processes in the network (Greenberg and Manor 2005; Hooper 1997a; 1998; Manor et al. 2003; Nadim et al. 2003).

A recent study demonstrated that when saline temperatures are varied from 7°C to 23°C *in vitro*, the pyloric frequency increases 4-fold while the phases remain largely constant (Tang et al. 2010), despite the fact that many of the underlying intrinsic neuron properties and synaptic dynamics change dramatically with temperature (Johnson et al. 1992; 1991; Tang et al. 2010). However, this work raises a question: Are the temperature-dependent changes in the neuronal activity we observe *in vitro* comparable to those that would be observed *in vivo*? While STG fictive motor patterns are clearly present in isolated ganglion preparations, functional behavior also requires the activation of muscles and sensory feedback, as well as interactions with other neuronal circuits (Stein 2009). The pyloric rhythm is also heavily regulated by neuromodulators, which arise both from sensory driven descending input fibers to the STG and from the hemolymph (Nusbaum and Beenhakker 2002; Stein 2009). In the *in vitro* environment, neuromodulators from descending inputs are present (in non-decentralized preparations), but the hemolymph and sensory feedback are absent. Additionally, these influences are themselves temperature-dependent and may influence CPG activity *in vivo*. We hypothesize that phase constancy is important for functional behavior and should therefore be present *in vivo* as well as *in vitro*. To test this, we introduced a controlled temperature perturbation while measuring the pyloric rhythm in intact *C. borealis* and *C. pagurus*, and, subsequently, we exposed a subset of the *C. borealis* specimens to a similar temperature perturbation *in vitro*.

4.2 Methods

4.2.1 Dissection and experiments

4.2.1.1 In vivo experiments

All *C. borealis* experiments were performed at the Marine Biological Laboratory (MBL) in Woods Hole, MA. All *C. pagurus* experiments were performed at the University of Ulm in Ulm, Germany.

4.2.1.1.1 Animals

Live *C. borealis* were obtained from commercial sources through the Marine Resources Center (MRC) in Woods Hole and were acclimated at 11ºC for at least 4 weeks in circulating seawater tanks. All *C. borealis* were fed three times per week before and after electrode implantation. Live *C. pagurus* were obtained from a commercial provider (Feinfisch GmbH, Neu-Ulm, Germany) and kept in filtered, aerated, artificial seawater at 10-12°C.

4.2.1.1.2 Electrode implantation

Crabs were immobilized with rubber bands and anesthetized on ice for 30-45 minutes. In the case of *C. pagurus,* animals were restrained in a custom-built holder (courtesy of H.G. Heinzel, University of Bonn, Germany). Application of a thin layer of super glue at the implantation site dried the carapace. A wall of dental cement (Protemp, ESPE) was built around the surgery site. Using a Dremel tool, a ca. 2x2 cm (for *C. borealis*) or 3x3 cm (for *C. pagurus*) piece of carapace was removed from inside the wall, and a slow saline drip (440 mM NaCl, 11 mM KCl, 26 mM $MgCl_2$, 13 mM $CaCl_2$, 10 (for *C. pagurus*) or 11 (for *C. borealis*) mM Trizma® base, 5 mM maleic acid, pH 7.4-7.6) and suction were set up to prevent excess hemolymph spilling and coagulation. The lateral ventricular nerve (*lvn*), dorsal ventricular nerve (*dvn*), and/or the median ventricular nerve (*mvn*) were exposed, and a home-built hook electrode was cemented onto the

carapace and placed around the nerve. The contact between the hook electrode and the nerve was then insulated by encasing the contact point in a Vaseline®-filled (9 parts Vaseline® and 1 part mineral oil) plastic or silicone tube around the hook and wire. The surgery site was closed with a piece of Parafilm® fixed with dental cement to the wall on the carapace (Hedrich and Stein 2008). In the case of *C. borealis,* the surgery site and the wire connections were waterproofed with marine adhesive sealant (3M™ Marine Fast Cure 5200) and/or DeKhotinsky cement (gift from Dr. Harvey Fishman). A Styrofoam™ float was used to keep the ends of the wires out of the water. During recovery from surgery and subsequent experiments, *C. borealis* were placed into isolated circulating seawater tanks (11°C) to recover for at least one day, while *C. pagurus* were kept in a holding tank filled with artificial seawater (9°C). *C. pagurus* were allowed to recover from surgery for at least 5 hours before beginning experiments.

4.2.1.1.3 Electrophysiology and data acquisition

In the *C. borealis* experiments, animals were placed into an isolated tank of seawater and exposed to a series of increasing temperatures from 10°C to 26°C. To alter the tank temperature, chilled or pre-heated seawater was added, and excess water was siphoned out in between temperature steps. Before each recording, *C. borealis* was generally allowed to acclimate 5 – 10 minutes to the new temperature. When this was not possible, we analyzed data only after the temperature had settled and did not change by more than 1 degree Celsius for at least 60 seconds. Temperature was recorded with a thermistor probe (Warner Instruments) and a manual thermometer.

In the *C. pagurus* experiments, the animal was placed in a small tank (approx. 40 cm x 30 cm x 20 cm) of artificial seawater (baseline temperature 9°C). Warm artificial seawater (approx. 30°C) was piped into the small tank so that the temperature of the water in the tank continuously changed by approximately 0.5-1.3 °C/minute. Cold seawater (9°C) was then piped into the tank in a similar fashion to bring the temperature

back down to baseline. Between experiments, the animal was kept in the holding tank at 9°C. Temperature was continuously measured using a USB TEMPer1 thermometer (PCsensor).

Data from seven *C. borealis* were analyzed and averaged across trials, with one animal undergoing four trials, two animals undergoing two trials, and four animals undergoing one trial (12 trials total). Data from five *C. pagurus* were analyzed and averaged across trials, with two animals undergoing three trials, one animal undergoing two trials, and two animals undergoing one trial each (10 trials total). One *C. pagurus* trial was removed from the study due to high irregularity of the rhythm at all temperatures, leaving nine trials from five animals.

For both species, data were filtered and amplified through an A-M Systems amplifier (Model 1700, Carlsborg, WA, USA), then recorded with a micro 1401 AD board (Cambridge Electronic Design, Cambridge, UK) and Spike2, version 6 (CED) on a Windows PC.

4.2.1.2 In vitro experiments

In a subset of the *C. borealis* animals, we recorded pyloric and gastric activity *in vivo* and then subsequently also *in vitro*. Dissections were performed as previously described in chilled physiological saline (Gutierrez and Grashow 2009). The STNS was pinned down in a Sylgard®-coated dish. Extracellular activity was first recorded with stainless steel pin electrodes that were placed into petroleum jelly wells on the motor nerves, then amplified and filtered with a differential amplifier (A-M Systems). During the recording, the STNS was continuously superfused with (11-26 ºC) saline. The temperature was monitored and controlled with a bipolar temperature controller (Warner Instruments, Model CL-100). Data were acquired using a Digidata 1200 data acquisition board (Axon Instruments).

To determine whether the tank temperature is an accurate proxy for the temperature of the STNS, we separately recorded the internal temperature of a *C. borealis* with a temperature probe while step-wise altering the tank temperature from 10 to 13º C and from 13 to 19 ºC, comparable to the *in vivo C. borealis* experiments. We found that the lag between the tank temperature and the internal temperature of the animal is small and the internal temperature equilibrated with the surrounding tank water at a rate of ~1ºC/minute. The slow rate of temperature change in the *in vivo* experiments thus allowed adequate time for the internal temperature of the animal to equilibrate to the recorded tank temperature.

4.2.2 Data analysis

C. borealis and *C. pagurus* were analyzed in a similar fashion. At tank temperatures of 11°C, 15°C, 19°C, 23°C, and 26°C, we extracted the average frequency, PD offset phase, LP onset phase, and LP offset phase from *lvn* or *dvn* recordings of five animals from each species. Pyloric frequency was defined as the reciprocal of the pyloric cycle period, which was calculated as the elapsed time between the start of one PD burst and the start of the subsequent PD burst. PD offset phase was defined as the elapsed time between the beginning and the end of a single PD burst, normalized by the current cycle period. Similarly, LP onset phase and offset phase were defined as the elapsed time between the beginning of a PD burst and the beginning and end (respectively) of the next LP burst, normalized by the cycle period. The PY phases were not examined due to difficulty in extracting the smaller spikes from the *lvn*/*dvn* recordings. From two additional specimens of *C. borealis*, the *mvn* activity was recorded, and the pyloric inferior cardiac neuron (IC), which fires in phase with LP, and the ventricular dilator neuron (VD), which fires in phase with PY (Weigeldt et al. 2002), were used to calculate pyloric frequency.

For analysis, segments of data were chosen for which the average temperature was within +/- 1 degree of the target temperature. We then calculated the Q_{10} of the

frequencies and phases to determine their relationship with temperature (Tang et al. 2010). The Q_{10} is the factor by which the rate of a process changes with a 10°C increase in temperature. By plotting the parameter of interest (frequency or phase) against temperature in a semi-log format, performing a linear regression analysis, and finding the slope *m* of the best-fit line, the Q_{10} can be calculated with the following formula:

$$Q_{10} = 10^{10m}$$

All data were analyzed using Clampex and Clampfit (Axon Instruments), Spike2 (Cambridge Electronic Design) and/or MATLAB (Mathworks). Statistical analyses were performed using the SigmaPlot 10 and SigmaStat software packages (Jandel Scientific) and Excel (Microsoft). Figures were generated with Adobe Illustrator (Adobe), Inkscape, CorelDRAW (Corel), and Excel (Microsoft).

4.3 Results

4.3.1 Recording the pyloric rhythm *in vivo*

The pyloric rhythm, which controls food filtration in the stomach, is one of two patterns generated by neuronal circuits found in the stomatogastric ganglion (STG) of the stomatogastric nervous system (Marder and Bucher 2007; Maynard and Dando 1974; Maynard and Selverston 1975; Selverston and Miller 1980). It is driven by a pacemaker kernel consisting of the electrically coupled anterior burster (AB) and two pyloric dilator (PD) neurons (Fig. 32A). The pacemaker kernel neurons inhibit the single lateral pyloric (LP) and the 4-5 electrically coupled pyloric (PY) neurons, which then rebound to produce a triphasic burst pattern (Fig. 32B). The pyloric cycle starts with the burst of the PD neuron (mid-sized spikes), followed by bursts of LP (large spikes) and PY (small spikes).

The recordings of the pyloric rhythm from the intact, freely behaving crab (*in vivo*) are similar in appearance to those obtained from *in vitro* recordings (Fig. 32B and 32C).

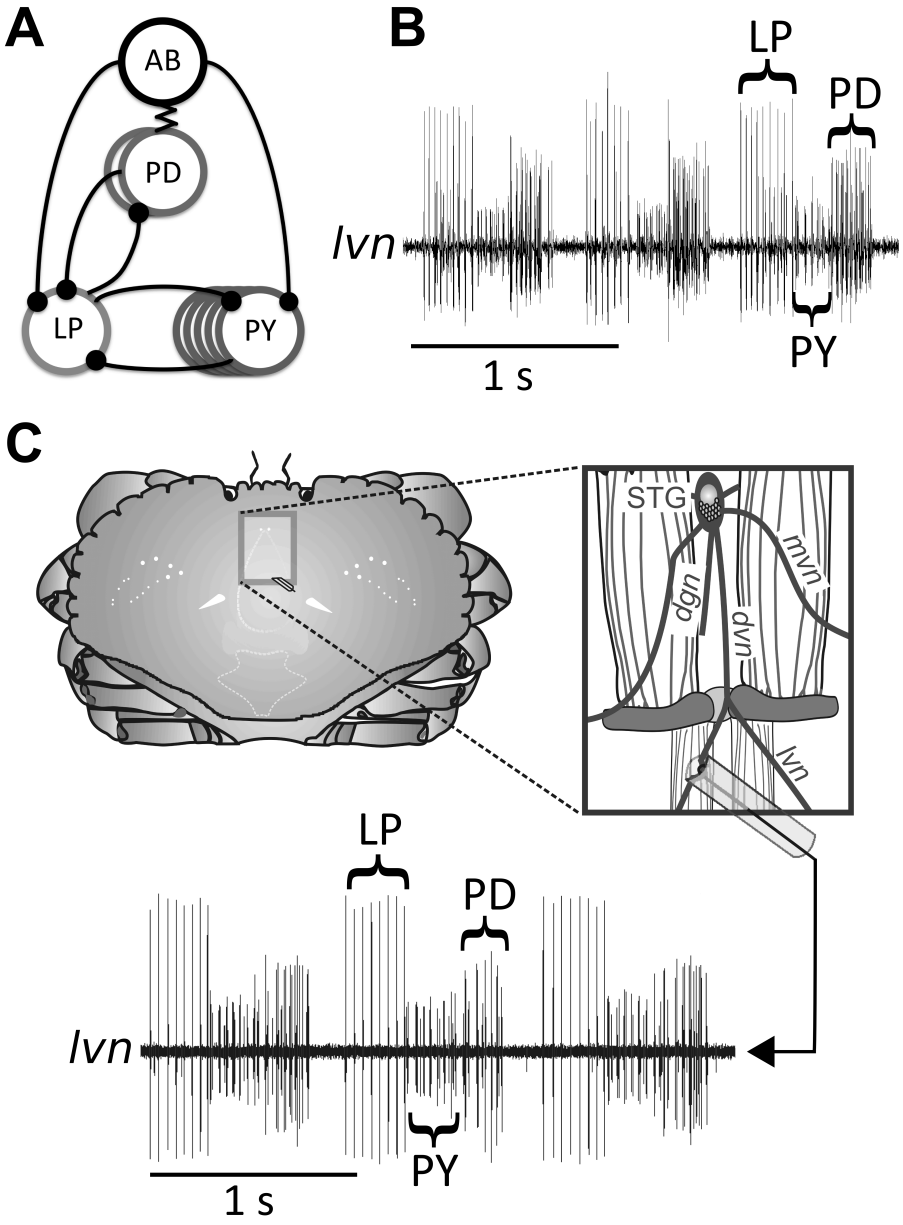

Figure 32. The pyloric circuit produces a triphasic rhythm. (A) Schematic diagram of the pyloric circuit. Inhibitory synapses are indicated by a line and black dot, and a zigzag line indicates electrical couplings. The electrically coupled AB and PD neurons together serve as the pacemaker complex, inhibiting the LP and PY neurons. (B) Sample *in vitro* extracellular trace of the triphasic pyloric rhythm, with PD, LP, and PY bursts indicated. (C) The part of the carapace and hypodermis surrounded by the box on the diagram of the crab (left) was cut away, revealing the major afferent nerves of the STNS and the GM muscles (right). A single hook electrode was anchored around the *dvn* or *lvn* (shown), and the nerve and hook were gently pulled into a polythene tube filled with Vaseline® to insulate the contact point between the nerve and electrode from the surrounding hemolymph. A reference electrode was anchored within the body cavity. The signal from the *dvn* or *lvn* was then recorded and analyzed.

4.3.2 Effects of temperature on the in vivo pyloric frequency

We studied the effect of increasing tank water temperature on the pyloric rhythm in intact *C. borealis* and *C. pagurus*. All animals (n = 12) responded with an increase in pyloric frequency to acutely raised tank temperatures. Figure 33 shows sample traces of the pyloric rhythm from each species as the temperature was increased. In this example, the frequency in *C. borealis* increased from 0.8 Hz at 11°C to 2.3 Hz at 26°C, and in *C. pagurus* from 0.9 Hz to 2.5 Hz.

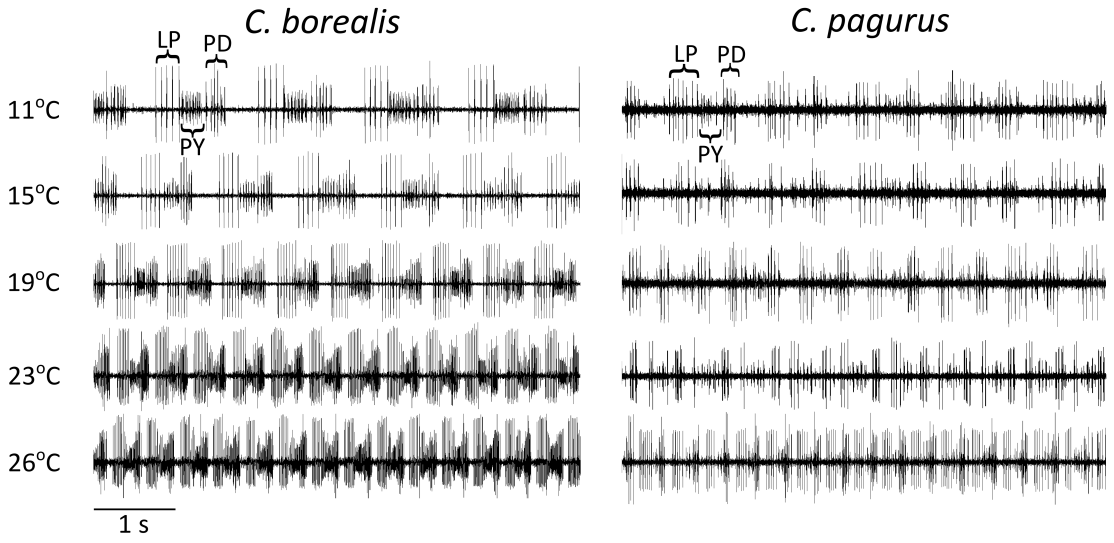

Figure 33. Sample extracellular traces from *C. borealis* and *C. pagurus* at 11, 15, 19, 23 and 26°C. In both species, recordings were made from either the *dvn* or *lvn*.

Figure 34 summarizes the effect of temperature on pyloric frequency for both species. Q_{10} analysis (Table 5) revealed the temperature dependence of the pyloric frequency between 11°C and 26°C. *C. borealis* and *C. pagurus* exhibited a Q_{10} of 2.08 and 2.41 respectively; these numbers fall near the same range as those of many biological processes (Lenz et al. 2005). The average maximum frequencies at 26°C were 2.3 ± 0.29 Hz (SD) for *C. pagurus* and 2.4 ± 0.48 Hz for *C. borealis*.

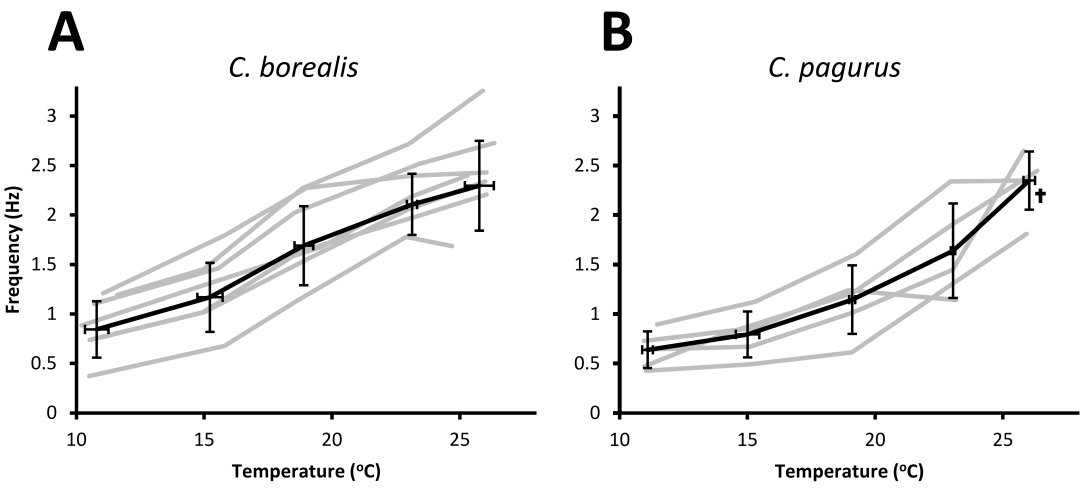

Figure 34. Pyloric frequency increases with temperature in *C. borealis* and *C. pagurus*. Gray lines indicate individual animals (n = 7 for *C. borealis* at all temperatures, and n = 5 for *C. pagurus* for all temperatures except where indicated by a single dagger, where n = 4). Thick black lines indicate the mean for all animals. Error bars indicate standard deviation.

4.3.3 The *in vitro* and *in vivo* pyloric frequencies at high temperatures are different in *C. borealis*

The *in vivo* frequencies in Figure 34 were generally slower than those previously reported for *in vitro* preparations of *C. borealis* (Tang et al. 2010). To examine this difference more closely, the stomatogastric nervous systems (STNS) of four of the seven *C. borealis* whose pyloric rhythms were recorded *in vivo* were subsequently subjected to a similar temperature ramp *in vitro*. Sample traces in Figure 35A show the increase in pyloric frequency both *in vivo* and *in vitro*. Comparison of the temperature dependence of the pyloric frequencies *in vivo* and *in vitro* across all four animals revealed a trend of higher *in vitro* frequencies compared to data from the same animals *in vivo*, and was statistically significant at 26ºC (Fig. 35B). The average maximum frequency reached a value of 3.5 Hz *in vitro*, or about 0.9 Hz faster than the frequency *in vivo*.

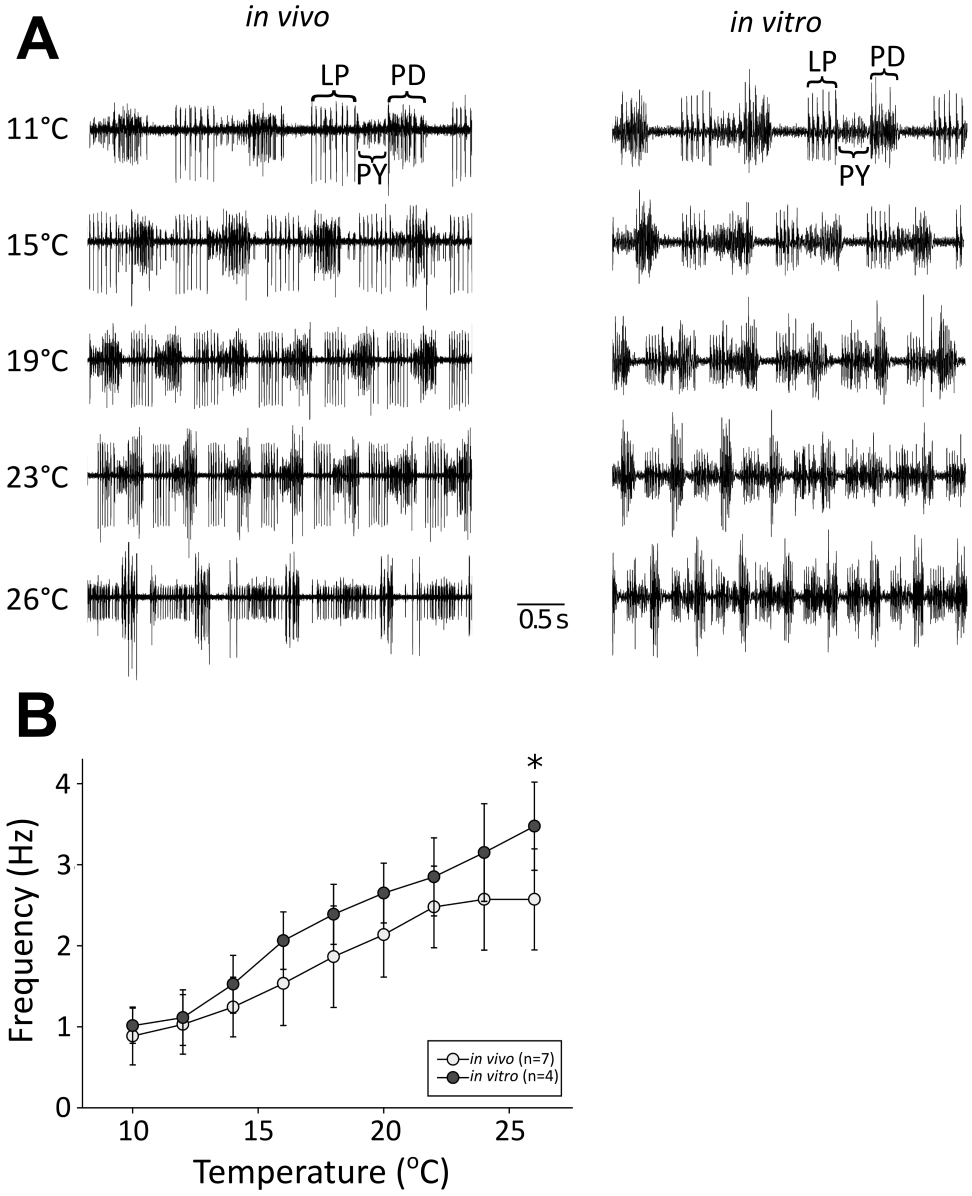

Figure 35. *In vivo* preparations exhibit slightly lower pyloric cycle frequencies than *in vitro*. (A) Sample traces of the *in vivo* and *in vitro* pyloric rhythms at 11, 15, 19, 23, and 26°C. (B) Average frequencies of the pyloric rhythm over a range of temperatures from 10°C to 26°C for both *in vivo* (n = 7) and *in vitro* (n = 4) preparations. Frequencies were divided into bins with widths of 2 degrees Celsius. Light gray dots indicate data from *in vivo* preparations, and dark gray dots indicate data from *in vitro* preparations. The x-values of the data points represent the average temperature for each bin. Bars indicate standard deviation. An asterisk (*) indicates significantly different groups at a significance level of $\alpha = 0.05$. Figure created by Marie Goeritz.

4.3.4 The pyloric rhythm is less reliable at higher temperatures

As had been seen in previous *in vitro* studies (Tang et al. 2012), at higher temperatures the rhythm often became irregular. For a 100-second window of time at each temperature, network activity was visually classified as follows: (i) LP, PD, and PY are bursting, (ii) LP is bursting unreliably or not at all, and (iii) activity is arrhythmic (Fig. 36). While the activity of *C. pagurus* was generally less robust than that of *C. borealis*, increasing temperatures lead to more disrupted motor patterns in both species.

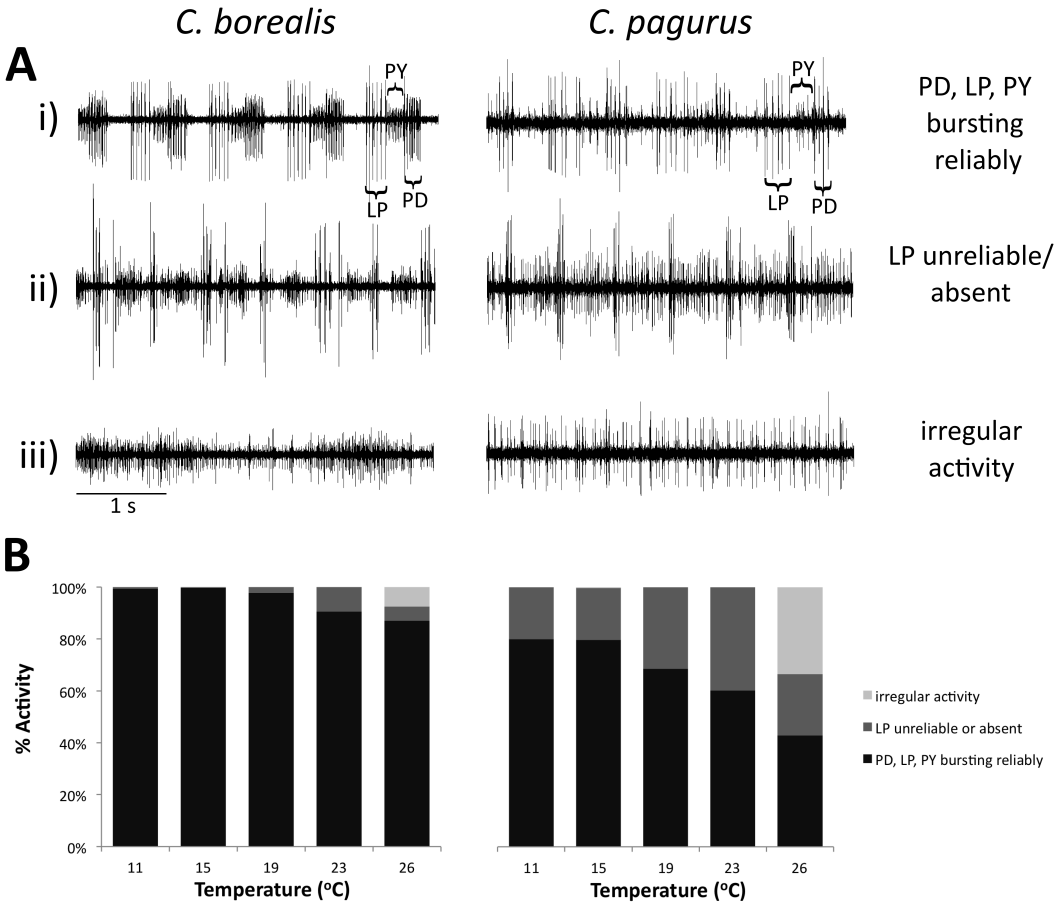

Figure 36. Burst reliability decreased at high temperatures. (A) Example recordings from *C. borealis* and *C. pagurus*, demonstrating bursting reliability, or the absence thereof, of LP. (B) Qualitative *in vivo* pyloric activity of *C. borealis* and *C. pagurus* at 11, 15, 19, 23, and 26°C. At each temperature, a 100-second window of activity was visually analyzed and the pyloric rhythm classified as having all three neurons bursting reliably (shown in black), having unreliable or absent LP activity (shown in dark gray), or having irregular or arrhythmic activity (shown in light gray).

4.3.5 Motor neuron phase relationships are maintained during temperature changes

Despite clear changes in pyloric cycle frequency with increasing temperature, the PD offset, LP onset, and LP offset phases were relatively well preserved across temperatures (Fig. 37). None of the burst phases in *C. pagurus* exhibited a Q_{10} significantly different from 1, suggesting that they are independent of temperature. Similarly, the PD offset and LP onset phases of *C. borealis* showed no significant temperature dependence. The LP offset phase in *C. borealis*, however, exhibited a slightly negative relationship with temperature (Fig. 37A). Previous *in vitro* findings saw a similar decrease in LP offset phase with temperature, though the effects were not statistically significant (Tang et al. 2010).

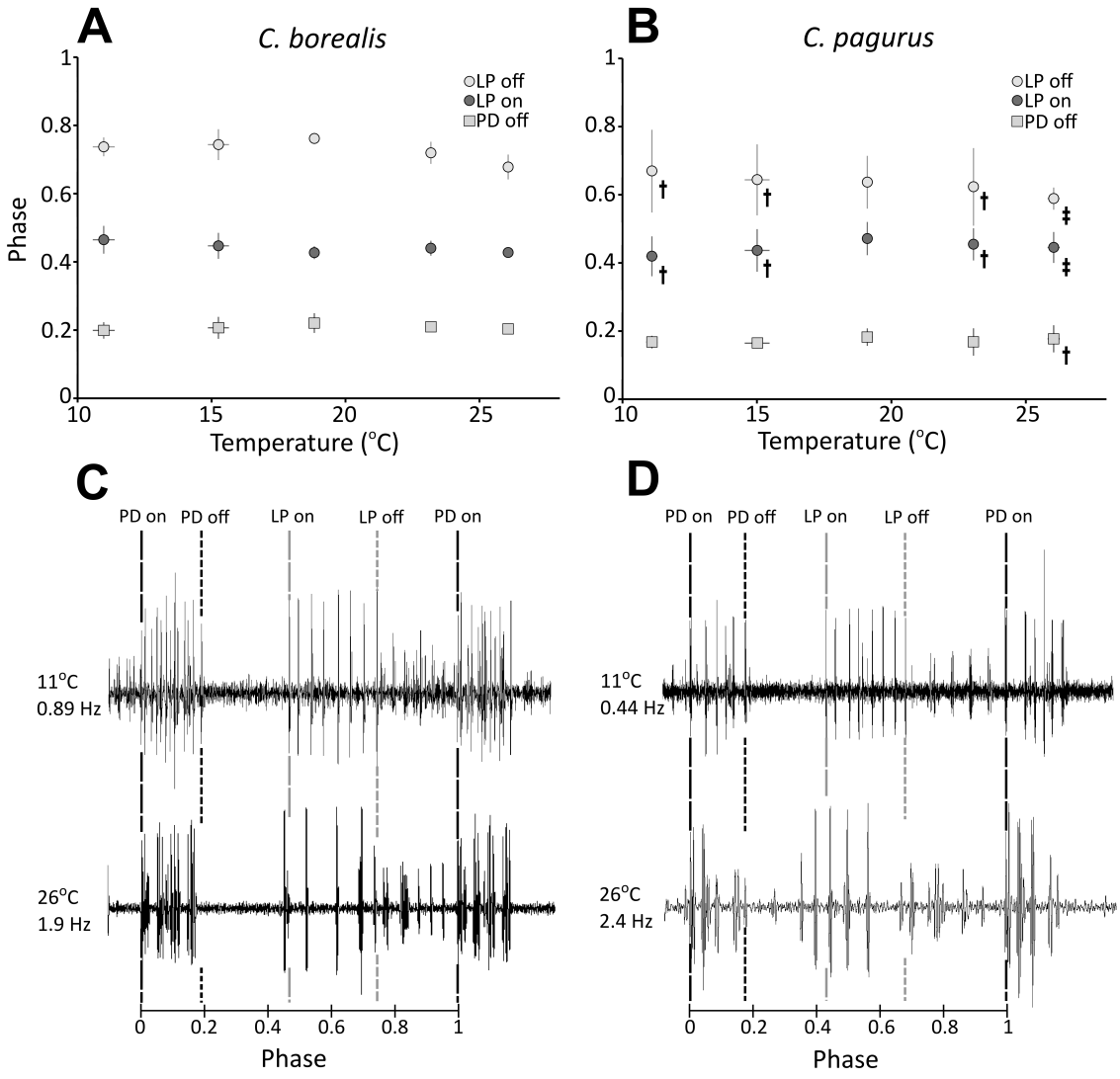

Figure 37. Pyloric phase relationships are maintained across temperatures. Squares, dark circles, and light circles indicate the mean PD offset phases, LP onset phases, and LP offset phases (respectively) at 11, 15, 19, 23, and 26°C for (A) *C. borealis* and (B) *C. pagurus*. $n = 5$ for *C. borealis* at all temperatures, and $n = 5$ for *C. pagurus* except where indicated by a single or double dagger. Single daggers indicate data points obtained using an n of 4, and double daggers indicate data points obtained using an n of 3. Error bars (not always visible) indicate standard deviation. Sample traces at 11°C and 26°C (not from the same trials) are shown for (C) *C. borealis* and (D) *C. pagurus*, normalized by period to indicate the motor neuron phases at different temperatures.

While in general, motor neuron phasing was well maintained during slow frequency changes, limits to this phase maintenance were unmasked during rapid changes in frequency. The studied temperature changes were rather slow, and the observed changes in frequency were correspondingly slow as well. As shown in Figure 37, most phases were well conserved during these temperature perturbations. However, this was not true on occasions where we saw rather sudden bouts of increased pyloric frequency, seemingly independent of temperature changes. Figure 38 shows an instance in *C. pagurus* in which the frequency rapidly increased from 0.6 Hz to 0.9 Hz within 20 seconds. Interestingly, during this increase in frequency, the phases were not well maintained. This lack of phase maintenance has been documented previously in *in vitro* preparations (Bucher et al. 2005).

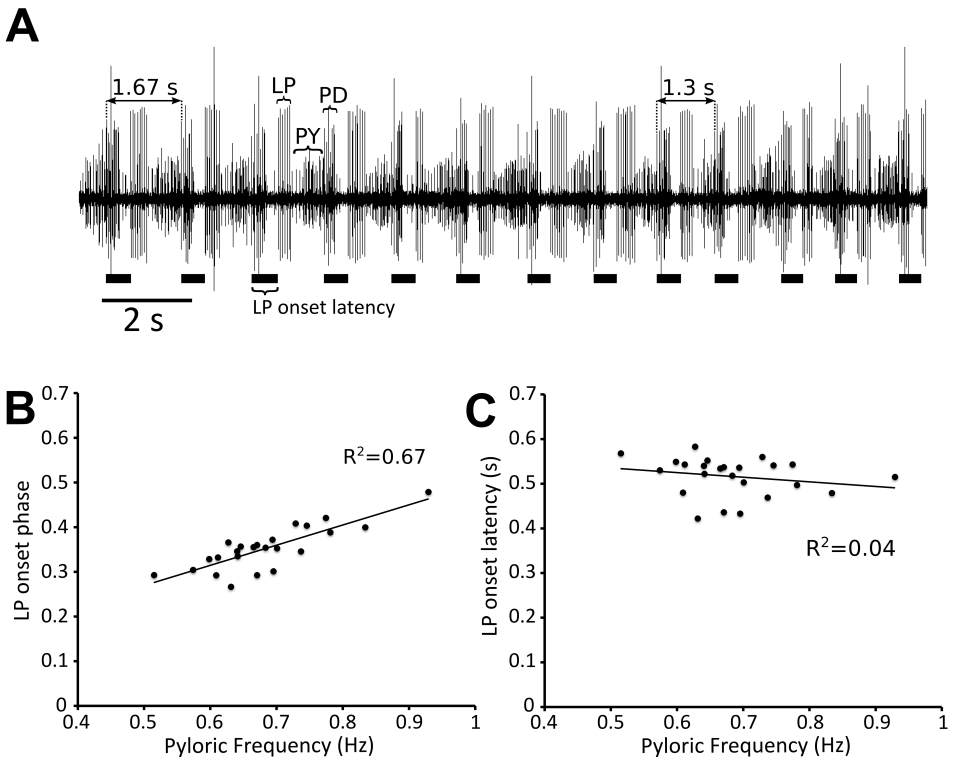

Figure 38. Example of a lack of phase maintenance during a rapid change in frequency. (A) Excerpt from a *C. pagurus dvn* or *lvn* recording during which the frequency rapidly increases without concurrent phase compensation. The lack of phase maintenance in this segment of the recording is relatively pronounced. Black bars indicate length of LP onset latency. (B) LP onset phase vs. frequency during the time over which pyloric frequency changed rapidly and the phase was not maintained. The phase-frequency relationship is relatively strong, suggesting that phase is not independent of frequency. (C) LP onset latency vs. frequency during the time over which pyloric frequency changed rapidly and the phase was not maintained. The latency-frequency relationship is relatively weak. Each pyloric cycle provides one data point. A linear fit of the data is indicated with a solid black line.

4.4 Discussion

Temperature compensation is found in many oscillatory and highly diverse systems (Izumo et al. 2003; Rinberg et al. 2013; Thuma et al. 2013; Zhurov and Brezina 2005). In poikilotherms, which have little or no control over their body temperature, temperature-dependent components of the neural circuitry are particularly affected by changing environmental conditions. These animals must thus compensate for

temperature-dependent changes to prevent disruption of vital functions such as breathing and chewing.

4.4.1 Temperature influences on the pyloric frequency.

Increasing temperature elicited a significant increase in the *in vivo* pyloric frequency of both *C. pagurus* and *C. borealis*. This effect of temperature on pyloric frequency was previously shown *in vitro* (Tang et al. 2010). Our results show a similar temperature dependence of the pyloric rhythm in the intact animal and that this effect is thus robust to sensory feedback, neuromodulators, and input from other components of crustacean neuronal circuitry that are not present in the *in vitro* preparation.

Two interesting observations arise from the experiments that directly compared the *in vivo* and *in vitro* pyloric response in *C. borealis* to temperature perturbations. First, at low temperatures the pyloric network activity *in vivo* was virtually indistinguishable from *in vitro*. These results are consistent with previous findings that recordings from STG neurons in intact crustaceans are generally similar to those from *in vitro* preparations at control temperatures (Hartline and Maynard 1975) and respond similarly to neuromodulator application (Heinzel et al. 1993) and, to an extent, neuromodulatory release from projection neurons (Diehl et al. 2013; Hedrich et al. 2011). The present experiments demonstrate that, to a point, the *in vitro* and *in vivo* preparations also respond similarly to temperature perturbations.

Our second observation, however, is that at higher temperatures, the pyloric network oscillates more slowly *in vivo* than *in vitro.* This trend became apparent at temperatures of 15°C and higher, although it was only statistically significant at the highest temperature tested. One reason for the lower frequencies *in vivo* could be restrictions imposed by the musculoskeletal system. At typical experimental temperatures of 10 - 13°C, the pyloric musculature in crustaceans exhibits pyloric-timed phasic contractions (Hooper et al. 1986; Jorge-Rivera and Marder 1996; Morris and Hooper 2001; Thuma et

al. 2003), and muscle activity patterns recorded *in vivo* are consistent with the *in vitro* pyloric rhythm (Morris and Maynard 1970; Rezer and Moulins 1983). Small-amplitude tooth movements in crabs are timed to the pyloric rhythm (Diehl et al. 2013; Weigeldt et al. 2002), indicating that the muscular and mechanical systems are well-tuned to the neuronal signals they receive. This makes sense because it is energetically favorable for the rhythmicity of a neuronal system to be similar to the resonant frequency of the mechanical body that it controls (Goodman et al. 2000). Studies in lobsters, however, suggest that at faster pyloric frequencies (above ~1 Hz), the temporal dynamics of certain pyloric muscles are too slow to allow them to fully relax between cycles (Morris et al. 2000). Similarly, the pyloric musculature in the shrimp is unable to follow rhythmic motor neuron stimulation at all frequencies without the presence of certain neuromodulators (Meyrand and Marder 1991). Temperature perturbation in isolated muscle preparations in the spiny lobster *Panulirus interruptus* also demonstrated that muscle contractions at higher temperatures are reduced and virtually absent at 16°C (Thuma et al. 2013), suggesting that the upper limit of the speed of the pyloric musculature is lower than that of the underlying neuronal circuitry, and the *in vivo* pyloric rhythm may be restricted to lower frequencies at high temperatures.

What mechanism could lead to reduced pyloric cycle frequency *in vivo*? The STNS is sensitive to sensory feedback and neuromodulators (both of which are largely absent *in vitro*) that may be involved in modifying pyloric frequencies *in vivo* at high temperatures. The effects of sensory feedback in *in vivo* closed-loop conditions on CPG activity are not easily generalizable. In biological CPGs, the removal of sensory feedback can either increase or decrease cycle frequency, depending on the system in question. Stimulating afferent nerves in cats reduces stepping frequency during walking (Whelan and Pearson 1997). Conversely, the frequency of the locust flight pattern generator is reduced when sensory afferents are removed (Pearson and Wolf 1987), and feedback strength can modulate wing beat frequency (Ausborn et al. 2007). There are myriad complex

interactions between sensorimotor pathways in the intact animal, making it difficult to discern the specific effect of any particular pathway on CPG output.

The frequency and phase relationships of STG motor patterns are influenced by several types of sensory and neuromodulatory inputs (Daur et al. 2009; Eisen and Marder 1984; Flamm and Harris-Warrick 1986; Harris-Warrick et al. 1998; Katz et al. 1989; Marder and Weimann 1992; Rezer and Moulins 1992; Smarandache et al. 2008; Weimann et al. 1993). While the effects of neuromodulators and sensory feedback have been closely examined under typical control temperatures, their intersection with temperature effects has not been closely examined. Preliminary *in vitro* studies indicate that the influence of neuromodulators on the pyloric frequency and phases is temperature-dependent (Haddad and Marder). Potentially, temperature-related changes in neuromodulatory input may modify motor neuron activity at high temperatures.

Recent modeling studies have shown that varying the underlying parameters of a neuronal oscillator can result in large differences in pyloric rhythm output at extreme temperatures (Rinberg et al. 2013). Our findings indicate that greater variability in the pyloric rhythm at high temperature is also seen *in vivo* (Fig. 36). It is thus likely that the intrinsic cellular properties of the pyloric rhythm, sensory feedback, and presence of neuromodulators all significantly contribute to determining the pyloric activity across a large range of temperatures.

4.4.2 Temperature influences on the phasing of the pyloric motor neurons

Between temperatures of 11°C and 26°C, phases were generally temperature-independent, as indicated by Q_{10} values which were not significantly different from 1. These results indicate that phase constancy, widely known to be present *in vitro*, is also present in the intact animal over a wide temperature and frequency range and is therefore robust to the presence of sensory feedback and neuromodulators. Previous *in vitro* studies have shown that the LP neuron is particularly susceptible to a failure to fire at

temperatures approaching 27°C (Tang et al. 2012) even as the PD and PY neurons remain active. We see a similar occurrence *in vivo*; the LP offset phase advances at temperatures nearing 26°C.

At the temperatures analyzed, pyloric frequency generally increased at a steady rate with temperature (Fig. 34). However, we also witnessed more than one instance in *C. pagurus* in which the frequency changed rapidly but the phases were not well maintained. A prominent example of this lack of phase maintenance is shown in Figure 38. Interestingly, previous *in vitro* studies show that when the pyloric frequency is altered via current injection (Hooper 1997a), or undergoes natural cycle-to-cycle variability (Bucher et al. 2005), phases are largely, but not perfectly, compensated. Similarly, when the large cell (LC) in the crustacean cardiac ganglion is subjected to pharmacological blockade, the excitability of the cell is rapidly increased, but returns to baseline levels via compensatory changes in the potassium currents I_A and I_{KCa} (Ransdell et al. 2012). Transient phase changes have previously been seen under *in vitro* decentralized conditions when the sensory gastropyloric receptors (GPRs) were stimulated, inducing a nearly 3-fold increase in pyloric frequency within 15 seconds (Katz and Harris-Warrick 1990). Serotonin directly excites the AB neuron (Eisen and Marder 1984; Marder and Eisen 1984); Katz and Harris-Warrick (1990) suggested that GPRs influence the pyloric network via an enhancement of bursting in AB, but not in the PDs to which AB is electrically coupled. Transient increases in frequency without concomitant phase compensation may happen because the neuromodulator-induced increase in AB cycle frequency occurs with faster dynamics than do the changes in synaptic and membrane properties necessary for phase compensation. It may be that the upper physiological limit of the rate of change in pyloric frequency is greater than the upper physiological limit of the rate of phase adaptation, and this difference in the time scale between frequency change and phase compensation is only unmasked during rapid changes in frequency.

Temperature dependence of cellular and network properties also has implications for the behaviors controlled by those networks. Our present results raise the question of how temperature affects the stomatogastric musculature. Proper phasing of the motor neurons is crucial for the pyloric filter to function; our results demonstrate that at temperatures in the range at which crabs may feed in the wild, a proper pyloric rhythm is often present. These findings align with recent results demonstrating that the ability of the lobster (*Panuliris interruptus*) to digest food is not impaired at higher temperatures (Thuma et al. 2013). Evidence is also mounting that previous exposure to extreme temperatures improves the ability of neuronal circuits to withstand wide temperature ranges (Robertson and Money 2012; Tang et al. 2012). Many rhythmic behaviors in other poikilotherms are significantly affected by temperature, including the goldfish startle-escape response (Preuss and Faber 2003) and the chirping frequency of cricket song (Doherty 1985). Other motor behaviors, such as the flight CPG in the deafferented locust, display robust temperature compensation (Foster and Robertson 1992; Robertson and Money 2012; Robertson et al. 1996) which may result from underlying processes with similar Q_{10}s but converse effects (Robertson and Money 2012).

It is difficult to predict *a priori* the effect of temperature on any particular neuronal circuit, since each has its own unique set of temperature-sensitive subcellular elements. However, temperature modulation has been used as a tool to trace the mechanisms of temperature dependence of complex behaviors in both poikilotherms and warm-blooded animals. Selective cooling of specific brain structures in the songbird (Fee and Long 2011; Long and Fee 2008) and frog (Yamaguchi et al. 2008), for example, has aided in locating brain regions that are involved in vocalization. Precise temperature control can thus serve as a method for deconstructing a neuronal network and gaining further insight into its function (Robertson and Money 2012).

4.5 Conclusion

In this study, we found that the pyloric cycle frequencies in intact *C. borealis* and *C. pagurus* exhibited a significantly positive relationship with temperature, while phases were generally maintained. Additionally, at elevated temperatures, the pyloric frequency of *C. borealis* was higher *in vitro* than it was *in vivo.*

Proper motor neuron phasing is necessary for rhythmic motor systems to function correctly. One strategy to ensure proper phasing at all times during an animal's lifetime could be to restrict CPG frequencies to a narrow range, so that motor neuron phasing is maintained by the uniform delays between bursts from each neuron type. An alternative strategy, employed by the STG, is to allow the frequency and burst delays to vary while keeping the phases of each neuron type constant. Such a strategy may provide greater versatility to the nervous system, allowing it to function properly in a wide range of environmental conditions.

4.6 Acknowledgements

Dr. Wolfgang Stein is currently assistant professor in the School of Biological Sciences at Illinois State University, Normal, IL 61790.

This work was supported by a National Science Foundation GRF and IGERT (to Soofi), NIH grant NS 81013 (to Marder), a Grass Fellowship (to Goeritz) and DFG STE 937/7-1 and STE 937/8-1 (to Stein). We thank Ulm University for the use of their facilities.

CHAPTER 5

CONCLUSIONS

5.1 Summary

Functional nervous systems are continuously performing two conflicting tasks. They must faithfully maintain crucial aspects of behavior, such as respiration, while simultaneously remaining amenable to developmental change and constant adaptation to the environment. To understand the mechanisms underlying the nervous system's ability to cope with this complex situation, it is best to study model systems for which the structure and output are known. At the time of this writing, we have at our disposal only a few systems well-characterized enough to fulfill this criterion, each of which consists of a relatively small number of neurons and synapses.

The work pioneered by Hodgkin and Huxley (Hodgkin and Huxley 1952) has enabled us to make sense of single-neuron activity and small neuronal networks by providing a mathematical model that relates various inputs of each neuron to its output. Once these aspects of any given system have been precisely quantified, we can use tools from the engineering realm, such as control theory, to further characterize the system. By essentially treating the network as a control system, we can create a simplified view of the relationships between network input, structure, and output.

In this thesis, we used the pyloric circuit in the stomatogastric ganglion of the decapod crustacean, a system for which the connectivity is fully known, to investigate the mechanisms of activity regulation at three levels of complexity – the single-neuron, network, and systems levels.

Functional and non-functional network activities are especially recognizable in central pattern-generating neuronal circuits such as the pyloric circuit, which exhibits a well-defined "set point" that is amenable to quantitative analysis. Observation of the pyloric rhythm has shown that specific parameters of pyloric activity can vary while

allowing the system to remain in a functional regime. Cycle period, for example, can vary between approximately 0.5 and 3 seconds in a given animal, while the relative timing of the bursts is generally well-maintained (though the degree of maintenance can vary between preparations (Bucher et al. 2005)). What dictates the shape of these "preferred" regions of activity? Do intrinsic parameters such as membrane conductances need to be tightly constrained to keep the network activity at a set point? Or, if these parameters are allowed to vary, are there "rules" that govern their variability? Brute force modeling techniques are increasingly being used to analyze the relationships between input and output in neuronal networks with several variable parameters, and several studies have suggested that pairwise parameter co-variation preserves specific types of activity, such as duty cycle or the shape of the slow wave (Ball et al. 2010; Hudson and Prinz 2010; Prinz et al. 2003a). However, intra-burst properties, such as the timing of spikes with the burst, may also hold functional significance to a neuronal network (Latorre et al. 2006); thus, there may be critical conductance regimes that control these properties as well. In **Aim 1** of this dissertation, described in Chapter 2, I discussed the observation of spike phase maintenance, wherein spike delays relative to the beginning of the cycle period vary proportionally with period. I used a conductance-based model neuron to determine whether co-varying conductance pairs can produce spike phase maintenance. I additionally used a model neuron database (Prinz et al. 2003a) to determine if conductance correlations exist in populations of neurons with constrained spike phases. Some conductance pairs, including the fast sodium and transient calcium pair, do support maintenance of spike phase patterns. Our work adds to a body of literature suggesting that intrinsic cellular parameters do follow a set of rules, which has not yet been fully elucidated, in order to preserve cellular output.

Membrane conductances affect not only the output pattern of a single neuron (Goldman et al. 2001; Hudson and Prinz 2010; Soofi et al. 2012), as discussed in Chapter 2, but also its response to biological or artificial synaptic input (Marder and Goaillard

2006; Prinz et al. 2003a; Taylor et al. 2009). In **Aim 2**, described in Chapter 3, I extend my analysis of input-output relationships to a network level by determining the effect of individual membrane conductances on neuronal response to synaptic input using the phase resetting curve (PRC). I examine conductance effects on the PRC with a single-compartment model neuron database and then determine the effects of a subset of these conductances on biological neurons with dynamic clamp. I further explored the effects of the leak and H conductances on the PRC by examining a 4-compartment model and by pharmacologically blocking the endogenous H current in PD. This work indicates that the H current, when present, advances the phase response. In addition, it has a regularizing effect on the PRC: When the H current is present, the phase responses can be predicted more accurately with a low order polynomial, suggesting that the PD neuron more reliably produces a particular phase response given a stimulus at a specific burst phase. This work builds on existing knowledge that conductances are crucial determinants of output and that the H current, in particular, promotes spiking reliability (Angelo and Margrie 2011) and synchrony (Ermentrout et al. 2012) in small networks. This work also highlights the importance of conductance location relative to the locations of spiking mechanisms, slow-wave generation, and synaptic input in a neuron model, as spatial differentiation can strongly affect PRC shape. We have extended the present understanding of how changes in a single conductance can alter network-level activity.

To properly regulate activity at the cellular and synaptic levels, CPGs must also adapt to environmental perturbations. Poikilotherms, such as the decapod crustacean, do not metabolically regulate their internal body temperatures and may experience temperature changes as great as 16^{o}C within a single day (Tang et al. 2010). The ability of the nervous system to cope with these temperature changes is not trivial because the ion channels that control cellular activity have a specific temperature dependence that can range by several fold (Robertson and Money 2012). Temperature has previously been shown to affect the period of the pyloric rhythm *in vitro*, while the rhythmic pattern is

largely maintained (Tang et al. 2010). However, in *in vitro* experiments, both the neuromodulators that bathe the STG in the intact animal and the sensory feedback from the musculature are absent. In **Aim 3**, described in Chapter 4, we surgically implanted electrodes in the intact decapod crustacean and monitored the pyloric rhythm while altering ambient water temperature to determine whether the *in vivo* environment alters the influence of temperature on the pyloric rhythm. Temperature increases led to a faster pyloric rhythm in all cases, though the effect was not as strong as seen *in vitro*. In addition, as is seen *in vitro*, phases were generally preserved as temperature was increased *in vivo*, suggesting that the phase maintenance of the pyloric rhythm is robust to extreme changes in the neuromodulatory and neuromuscular environments.

5.2 A look ahead

The work detailed in this thesis furthers our understanding of activity regulation in small neuronal networks on three fronts. We described mechanisms for preserving spike phase patterns, we related intrinsic neuronal parameters to cellular response to synaptic input, and we described the effect of the *in vivo* environment on the CPG's response to external perturbations. This work, and, more generally, the field of neuroscience following Hodgkin and Huxley's work, has been made possible through the synergistic use of experimentation and computational modeling. We live in an era in which computational power is expanding at a nearly incomprehensible pace. At the same time, we are constantly rediscovering the extent of the complexity of nervous systems – including the small networks described in this work. As we and others in the field have shown, neuromodulators play a major role in controlling network activity (Stein 2009), and sensory feedback alters network activity, as well. Recent work from the Prinz research group has elucidated a novel chloride-dependent mechanism for homeostatically regulating synaptic strength (Archila et al. 2012). In addition, recent evidence suggests that chondroitin sulfate proteoglycans (CSPGs), found in the crustacean extracellular

matrix, may also play a role in homeostatic recovery following decentralization (i.e. removal of input from the commissural ganglia and esophageal ganglion) of the STG (Hudson et al. 2012). Our work has detailed the role of specific conductances on responses to synaptic input and has shown that spatial separation of the conductances in a model neuron is a determinant of network output. With this information in hand, the time is ripe to begin to develop a morphologically accurate mechanistic model that includes multiple dimensions of mechanisms for activity regulation. Analysis of the mechanisms of STG activity is, for logistical reasons, a highly fragmented process, with related work divvied between several research groups. To gain a holistic insight into network function, our individual efforts must eventually coalesce.

Currently, various political and funding bodies are eagerly envisaging the impending development of a "connectome", or a complete map of synaptic connectivities, for various mammalian neuronal networks, including (ambitiously) the human brain. But the data contained within a connectome is a small fraction of that which we need to truly understand nervous system activity, as has been demonstrated through numerous studies on the STNS and other small neuronal networks. If we hope to achieve a bottom-up understanding of activity in complex nervous systems, including those of humans, such work must include physiological studies at the cellular and synaptic levels in small neuronal networks such as the STG, whose properties we still cannot claim to fully understand.

APPENDIX A

SUPPLEMENTARY TABLES

Table 3. Conductance values for the "canonical" bursting model and ranges over which they were varied in the single-burster modeling study

Conductance	"Canonical" conductance value (mS/cm^2)	Conductance range (mS/cm^2)
g_{Na}	200	0-600
g_{CaT}	5	0-15
g_{CaS}	4	0-12
g_{A}	40	0-120
g_{KCa}	5	0-15
g_{Kd}	125	0-375
g_{H}	0.01	0-0.03
g_{leak}	0.02	0-0.06

Table 4. Correlation strength of conductances from the single-burster and population studies for all conductance pairs

	Single-burster study		Population study	
Conductance Pair (g_x)	Spearman's ρ	p-value	Spearman's ρ	X^2
g_{CaT} vs. g_{Kd}	*0.98 (+)*	*1.36×10^{-46}*	0.47	60.1
g_A vs. g_{CaS}	*0.92 (+)*	*7.27×10^{-89}*	0.04	37.7
g_{Na} vs. g_{CaT}	*0.69 (+)*	*2.04×10^{-07}*	*0.8*	*264.2*
g_{CaS} vs. g_{leak}	*0.51 (+)*	*3.91×10^{-14}*	0.2	34.4
g_{CaS} vs. g_{KCa}	*0.44 (+)*	*$< 1 \times 10^{-90}$*	*0.67*	*177.7*
g_{CaT} vs. g_H	0.36	0.00	-0.03	25.7
g_{Kd} vs. g_{leak}	*0.62 (+,R)*	*0.00*	-0.15	40.4
	-0.87 (-,L)	*9.95×10^{-19}*		
g_A vs. g_{CaT}	0.3	0.01	0.24	38.2
g_{KCa} vs. g_{Kd}	0.2	0.01	0.12	40.4
g_{Na} vs. g_{leak}	*0.53 (+,BR)*	*1.39×10^{-11}*	-0.18	23.0
	0.94 (+,TL)	*6.75×10^{-51}*		
g_{Na} vs. g_{KCa}	0.16	0.03	-0.36	62.7
g_{CaS} vs. g_{Kd}	-0.26	0.04	-0.2	23.0
	0.98 (+,T)	*4.34×10^{-12}*		
g_A vs. g_H	0.02	0.64	0.11	22.4
g_{KCa} vs. g_H	0	0.95	-0.07	19.6
g_{CaS} vs. g_H	0	1.00	0	18.5
g_H vs. g_{leak}	0	1.00	-0.05	45.1
g_{Na} vs. g_H	-0.03	0.58	-0.13	25.1
g_{Na} vs. g_{CaS}	-0.06	0.65	-0.27	37.6
g_{Na} vs. g_A	*0.94 (+,TL)*	*1.15×10^{-14}*	0.27	31.5
	0.07	0.50		
g_{KCa} vs. g_{leak}	-0.07	0.09	-0.09	26.3
g_{CaT} vs. g_{KCa}	-0.12	0.16	*-0.52*	*81.8*
g_{CaT} vs. g_{leak}	*0.89 (+,L)*	*1.65×10^{-07}*	-0.02	40.0
	-0.55 (-,R)	*4.42×10^{-07}*		
g_A vs. g_{Kd}	0.24	0.02	-0.16	34.3
	-0.57 (-,B)	*0.00*		
g_A vs. g_{KCa}	-0.27	2.90×10^{-09}	*-0.37*	*78.2*
g_{CaT} vs. g_{CaS}	-0.37	0.01	*-0.47*	*71.7*
g_{Kd} vs. g_H	-0.39	2.27×10^{-06}	-0.11	16.9
g_{Na} vs. g_{Kd}	*0.94 (+,TR)*	*1.94×10^{-45}*	0.22	31.8
	-0.90 (-,BL)	*3.92×10^{-20}*		
g_A vs. g_{leak}	*-0.55 (-)*	*0.00*	-0.16	41.9

Columns 2 and 3 show the statistical output from the single-burster study, in which

conductances were varied pairwise by a multiplicative factor of 0 to 3 from a canonical value. Pairs are sorted by their Spearman's ρ values (column 2). For those conductance pairs with relationships that were examined piecewise, statistical output is shown from each portion of the data. To indicate which portion is being referred to, the relative locations of the respective portions of data are indicated in parentheses (L = left, R = right, T = top, B = bottom, TL = top left, BL = bottom left, TR = top right, BR = bottom right). Columns 4 and 5 show the statistical output from the population study, in which a population of model neurons constrained to have a duty cycle of 0.2784 ± 0.005 and 13 spikes per burst was examined for conductance correlations. Values are italicized if both criteria for correlation are met ($|\rho| \geq 0.4$, $p < 0.05$ for the single-burster study, and $|\rho| \geq 0.3$ and $X^2 \geq 70$ for the population study)

Table 5. Temperature dependence of pyloric frequencies and phases.

Species	Pyloric rhythm characteristic	Q_{10}	Standard error of Q_{10}	*m* (*pos.*, *neg.* , 0)
C. borealis	Frequency	2.08	0.18	*pos.* ($p < 0.001$)
	PD offset	1.02	0.042	0 ($p = 0.57$)
	LP onset	0.96	0.022	0 ($p = 0.064$)
	LP offset	0.95	0.019	*neg.* ($p = 0.018$)
C. pagurus	Frequency	2.41	0.25	*pos.* ($p < 0.001$)
	PD offset	1.02	0.066	0 ($p = 0.76$)
	LP onset	1.06	0.054	0 ($p = 0.29$)
	LP offset	0.94	0.059	0 ($p = 0.31$)

The slope of the best-fit line associated with the Q_{10} (*m*) is indicated as positive (*pos.*), negative (*neg.*), or not significantly different from zero (0) at a significance level of $\alpha = 0.05$. Positive and negative values indicate that the characteristic has a positive or negative relationship (resp.) with temperature. Slope values marked with 0 indicate that the associated characteristic has no temperature dependence.

REFERENCES

Achard P, De Schutter E. Complex parameter landscape for a complex neuron model. *PLoS Comput Biol* 2: e94, 2006.

Akil H, Martone ME, Van Essen DC. Challenges and opportunities in mining neuroscience data. *Science* 331: 708-712, 2011.

Anderson JR, Jones BW, Watt CB, Shaw MV, Yang JH, Demill D, Lauritzen JS, Lin Y, Rapp KD, Mastronarde D, Koshevoy P, Grimm B, Tasdizen T, Whitaker R, Marc RE. Exploring the retinal connectome. *Mol Vis* 17: 355-379, 2011.

Angelo K, London M, Christensen SR, Hausser M. Local and global effects of I(h) distribution in dendrites of mammalian neurons. *J Neurosci* 27: 8643-8653, 2007.

Angelo K, Margrie TW. Population diversity and function of hyperpolarization-activated current in olfactory bulb mitral cells. *Sci Rep* 1: 50, 2011.

Aponte Y, Lien CC, Reisinger E, Jonas P. Hyperpolarization-activated cation channels in fast-spiking interneurons of rat hippocampus. *J Physiol* 574: 229-243, 2006.

Archila S, Wenner P, Prinz AA. Experimental and computational evidence suggest possible regulation of synaptic conductance via graded post-synaptic chloride homeostasis. Program No. 46.17. 2012 Neuroscience Meeting Planner. New Orleans, LA: Society for Neuroscience, 2012.

Ausborn J, Stein W, Wolf H. Frequency control of motor patterning by negative sensory feedback. *J Neurosci* 27: 9319-9328, 2007.

Ball JM, Franklin CC, Tobin AE, Schulz DJ, Nair SS. Coregulation of ion channel conductances preserves output in a computational model of a crustacean cardiac motor neuron. *J Neurosci* 30: 8637-8649, 2010.

Baro DJ, Levini RM, Kim MT, Willms AR, Lanning CC, Rodriguez HE, Harris-Warrick RM. Quantitative single-cell-reverse transcription-PCR demonstrates that A-current magnitude varies as a linear function of shal gene expression in identified stomatogastric neurons. *J Neurosci* 17: 6597-6610, 1997.

Barrento S, Marques A, Vaz-Pires P, Nunes ML. Live shipment of immersed crabs *Cancer pagurus* from England to Portugal and recovery in stocking tanks: stress parameter characterization. *ICES J Mar Sci* 67: 435-443, 2010.

Berkowitz A, Roberts A, Soffe SR. Roles for multifunctional and specialized spinal interneurons during motor pattern generation in tadpoles, zebrafish larvae, and turtles. *Front Behav Neurosci* 4: 36, 2010.

Brochini L, Carelli PV, Pinto RD. Single synapse information coding in intraburst spike patterns of central pattern generator motor neurons. *Journal of Neuroscience* 31: 12297-12306, 2011.

Brown GL, Eccles JC. The action of a single vagal volley on the rhythm of the heart beat. *J Physiol* 82: 211-241, 1934.

Bucher D, Prinz AA, Marder E. Animal-to-animal variability in motor pattern production in adults and during growth. *J Neurosci* 25: 1611-1619, 2005.

Büschges A, Scholz H, El Manira A. New moves in motor control. *Curr Biol* 21: R513-524, 2011.

Cajal SR. Estructura de los centros nerviosos de las aves. *Rev Trim Histol Norm Patol* 1: 1-10, 1888.

Calabrese RL, Prinz AA. Realistic modeling of small neuronal networks. In: *Computational Modeling Methods for Neuroscientists*, edited by Schutter ED. Cambridge, MA: MIT Press, 2009.

Cao XJ, Oertel D. Temperature affects voltage-sensitive conductances differentially in octopus cells of the mammalian cochlear nucleus. *J Neurophysiol* 94: 821-832, 2005.

Chen K, Aradi I, Thon N, Eghbal-Ahmadi M, Baram TZ, Soltesz I. Persistently modified h-channels after complex febrile seizures convert the seizure-induced enhancement of inhibition to hyperexcitability. *Nat Med* 7: 331-337, 2001.

Chevallier S, Jan Ijspeert A, Ryczko D, Nagy F, Cabelguen JM. Organisation of the spinal central pattern generators for locomotion in the salamander: biology and modelling. *Brain Res Rev* 57: 147-161, 2008.

Cohen AH, Ermentrout GB, Kiemel T, Kopell N, Sigvardt KA, Williams TL. Modelling of intersegmental coordination in the lamprey central pattern generator for locomotion. *Trends Neurosci* 15: 434-438, 1992.

Connor JA, Walter D, McKown R. Neural repetitive firing: modifications of the Hodgkin-Huxley axon suggested by experimental results from crustacean axons. *Biophys J* 18: 81-102, 1977.

Craddock RC, Jbabdi S, Yan CG, Vogelstein JT, Castellanos FX, Di Martino A, Kelly C, Heberlein K, Colcombe S, Milham MP. Imaging human connectomes at the macroscale. *Nat Methods* 10: 524-539, 2013.

Dai A, Temporal S, Schulz DJ. Cell-specific patterns of alternative splicing of voltage-gated ion channels in single identified neurons. *Neuroscience* 168: 118-129, 2010.

Daur N, Nadim F, Stein W. Regulation of motor patterns by the central spike-initiation zone of a sensory neuron. *Eur J Neurosci* 30: 808-822, 2009.

Day M, Carr DB, Ulrich S, Ilijic E, Tkatch T, Surmeier DJ. Dendritic excitability of mouse frontal cortex pyramidal neurons is shaped by the interaction among HCN, Kir2, and Kleak channels. *J Neurosci* 25: 8776-8787, 2005.

Dayan P, Abbott LF. *Theoretical Neuroscience*. Cambridge, MA: MIT Press, 2001.

DeFelipe J. From the connectome to the synaptome: an epic love story. *Science* 330: 1198-1201, 2010.

Diehl F, White RS, Stein W, Nusbaum MP. Motor circuit-specific burst patterns drive different muscle and behavior patterns. *J Neurosci* 33: 12013-12029, 2013.

Doherty JA. Temperature coupling and 'trade-off' phenomena in the acoustic communication system of the cricket, *Gryllus bimaculatus* De Geer (Gryllidae). *J Exp Biol* 114: 17-35, 1985.

Doi A, Ramirez JM. Neuromodulation and the orchestration of the respiratory rhythm. *Respir Physiol Neurobiol* 164: 96-104, 2008.

Doloc-Mihu A, Calabrese RL. A database of computational models of a half-center oscillator for analyzing how neuronal parameters influence network activity. *J Biol Phys* 37: 263-283, 2011.

Donahue MJ, Nichols A, Santamaria CA, League-Pike PE, Krediet CJ, Perez KO, Shulman MJ. Predation risk, prey abundance, and the vertical distribution of three brachyuran crabs on gulf of Maine shores. *J Crustacean Biol* 29: 523-531, 2009.

Dorval AD, Christini DJ, White JA. Real-Time linux dynamic clamp: a fast and flexible way to construct virtual ion channels in living cells. *Ann Biomed Eng* 29: 897-907, 2001.

Draper N, Smith H. *Applied regression analysis*. New York: Wiley, 1981.

Eisen JS, Marder E. A mechanism for production of phase shifts in a pattern generator. *J Neurophysiol* 51: 1375-1393, 1984.

El Manira A, Kyriakatos A, Nanou E. Beyond connectivity of locomotor circuitry-ionic and modulatory mechanisms. *Prog Brain Res* 187: 99-110, 2010.

Ermentrout B, Beverlin B, Netoff T. Phase response curves to measure ion channel effects on neurons. In: *Phase response curves in neuroscience*, edited by Schultheiss N, Prinz AA, and Butera RJ. New York: Springer, 2012.

Fee MS, Long MA. New methods for localizing and manipulating neuronal dynamics in behaving animals. *Curr Opin Neurobiol* 21: 693-700, 2011.

Flamm RE, Harris-Warrick RM. Aminergic modulation in lobster stomatogastric ganglion. I. Effects on motor pattern and activity of neurons within the pyloric circuit. *J Neurophysiol* 55: 847-865, 1986.

Foster JA, Robertson RM. Temperature dependency of wing-beat frequency in intact and deafferented locusts. *J Exp Biol* 162: 295-312, 1992.

Goaillard JM, Taylor AL, Schulz DJ, Marder E. Functional consequences of animal-to-animal variation in circuit parameters. *Nat Neurosci* 12: 1424-1430, 2009.

Goeritz ML, Ouyang Q, Harris-Warrick RM. Localization and function of Ih channels in a small neural network. *J Neurophysiol* 106: 44-58, 2011.

Goldman MS, Golowasch J, Marder E, Abbott LF. Global structure, robustness, and modulation of neuronal models. *J Neurosci* 21: 5229-5238, 2001.

Golomb D, Amitai Y. Propagating neuronal discharges in neocortical slices: computational and experimental study. *J Neurophysiol* 78: 1199-1211, 1997.

Golowasch J, Abbott LF, Marder E. Activity-dependent regulation of potassium currents in an identified neuron of the stomatogastric ganglion of the crab Cancer borealis. *J Neurosci* 19: RC33, 1999.

Golowasch J, Buchholtz F, Epstein IR, Marder E. Contribution of individual ionic currents to activity of a model stomatogastric ganglion neuron. *J Neurophysiol* 67: 341-349, 1992.

Golowasch J, Goldman MS, Abbott LF, Marder E. Failure of averaging in the construction of a conductance-based neuron model. *J Neurophysiol* 87: 1129-1131, 2002.

Goodman L, Riley MA, Mitra S, Turvey MT. Advantages of rhythmic movements at resonance: minimal active degrees of freedom, minimal noise, and maximal predictability. *J Mot Behav* 32: 3-8, 2000.

Grashow R, Brookings T, Marder E. Compensation for variable intrinsic neuronal excitability by circuit-synaptic interactions. *J Neurosci* 30: 9145-9156, 2010.

Graubard K. Synaptic transmission without action potentials: input-output properties of a nonspiking presynaptic neuron. *J Neurophysiol* 41: 1014-1025, 1978.

Greenberg I, Manor Y. Synaptic depression in conjunction with A-current channels promote phase constancy in a rhythmic network. *J Neurophysiol* 93: 656-677, 2005.

Guckenheimer J, Gueron S, Harris-Warrick RM. Mapping the dynamics of a bursting neuron. *Philos Trans R Soc Lond B Biol Sci* 341: 345-359, 1993.
Gutierrez GJ, Grashow RG. *Cancer borealis* stomatogastric nervous system dissection. *J Vis Exp* 2009.
Haddad SA, Marder E. Modulator induced changes in motor patterns are temperature compensated. Program No. 559.08. 2013 Neuroscience Meeting Planner. San Diego, CA: Society for Neuroscience, 2013. Online.
Haefner PA. Aspects of the biology of the jonah crab, *Cancer borealis* Stimpson, 1859 in the mid-Atlantic Bight. *J Nat Hist* 11: 303-320, 1977.
Hansel D, Mato G, Meunier C. Synchrony in Excitatory Neural Networks. *Neural Computation* 7: 307-337, 1995.
Harris-Warrick RM. Neuromodulation and flexibility in Central Pattern Generator networks. *Curr Opin Neurobiol* 21: 685-692, 2011.
Harris-Warrick RM, Johnson BR, Peck JH, Kloppenburg P, Ayali A, Skarbinski J. Distributed effects of dopamine modulation in the crustacean pyloric network. *Ann N Y Acad Sci* 860: 155-167, 1998.
Hartline DK, Maynard DM. Motor patterns in the stomatogastric ganglion of the lobster *Panulirus argus*. *J Exp Biol* 62: 405-420, 1975.
Hedrich UB, Diehl F, Stein W. Gastric and pyloric motor pattern control by a modulatory projection neuron in the intact crab *Cancer pagurus*. *J Neurophysiol* 105: 1671-1680, 2011.
Hedrich UBS, Stein W. Characterization of a descending pathway: activation and effects on motor patterns in the brachyuran crustacean stomatogastric nervous system. *J Exp Biol* 211: 2624-2637, 2008.
Heinzel HG, Weimann JM, Marder E. The behavioral repertoire of the gastric mill in the crab, *Cancer pagurus*: an *in situ* endoscopic and electrophysiological examination. *J Neurosci* 13: 1793-1803, 1993.
Helmstaedter M. Cellular-resolution connectomics: challenges of dense neural circuit reconstruction. *Nat Methods* 10: 501-507, 2013.
Hodgkin AL, Huxley AF. A quantitative description of membrane current and its application to conduction and excitation in nerve. *J Physiol* 117: 500-544, 1952.
Hooper SL. Phase maintenance in the pyloric pattern of the lobster (*Panulirus interruptus*) stomatogastric ganglion. *J Comput Neurosci* 4: 191-205, 1997a.
Hooper SL. The pyloric pattern of the lobster (*Panulirus interruptus*) stomatogastric ganglion comprises two phase-maintaining subsets. *J Comput Neurosci* 4: 207-219, 1997b.
Hooper SL. Transduction of temporal patterns by single neurons. *Nat Neurosci* 1: 720-726, 1998.
Hooper SL, O'Neil MB, Wagner R, Ewer J, Golowasch J, Marder E. The innervation of the pyloric region of the crab, *Cancer borealis*: homologous muscles in decapod species are differently innervated. *J Comp Physiol A* 159: 227-240, 1986.
Hooper SL, Weaver AL. Motor neuron activity is often insufficient to predict motor response. *Curr Opin Neurobiol* 10: 676-682, 2000.
Hudson AE, Prinz AA. Conductance ratios and cellular identity. *PLoS Comput Biol* 6: e1000838, 2010.

Hudson AE, Tang C, Prinz AA. Degradation of chondroitin sulfate proteoglycans in an invertebrate central pattern generator alters homeostatic maintenance of rhythmic activity. 2012 Neuroscience Meeting Planner New Orleans, LA: Society for Neuroscience, 2012.

Huguenard JR, McCormick DA. Simulation of the currents involved in rhythmic oscillations in thalamic relay neurons. *J Neurophysiol* 68: 1373-1383, 1992.

Izumo M, Johnson CH, Yamazaki S. Circadian gene expression in mammalian fibroblasts revealed by real-time luminescence reporting: temperature compensation and damping. *Proc Natl Acad Sci U S A* 100: 16089-16094, 2003.

Johnson BR, Peck JH, Harris-Warrick RM. Elevated temperature alters the ionic dependence of amine-induced pacemaker activity in a conditional burster neuron. *J Comp Physiol A* 170: 201-209, 1992.

Johnson BR, Peck JH, Harris-Warrick RM. Temperature sensitivity of graded synaptic transmission in the lobster stomatogastric ganglion. *J Exp Biol* 156: 267-285, 1991.

Jorge-Rivera JC, Marder E. TNRNFLRFamide and SDRNFLRFamide modulate muscles of the stomatogastric system of the crab *Cancer borealis*. *J Comp Physiol A* 179: 741-751, 1996.

Kandel ER, Schwartz JH, Jessell TM. *Principles of Neural Science*. New York: McGraw-Hill, 2000., 2000.

Katz PS. Evolution and development of neural circuits in invertebrates. *Curr Opin Neurobiol* 17: 59-64, 2007.

Katz PS, Eigg MH, Harris-Warrick RM. Serotonergic/cholinergic muscle receptor cells in the crab stomatogastric nervous system. I. Identification and characterization of the gastropyloric receptor cells. *J Neurophysiol* 62: 558-570, 1989.

Katz PS, Harris-Warrick RM. Neuromodulation of the crab pyloric central pattern generator by serotonergic/cholinergic proprioceptive afferents. *J Neurosci* 10: 1495-1512, 1990.

Khorkova O, Golowasch J. Neuromodulators, not activity, control coordinated expression of ionic currents. *J Neurosci* 27: 8709-8718, 2007.

Kiehn O. Locomotor circuits in the mammalian spinal cord. *Annu Rev Neurosci* 29: 279-306, 2006.

Krediet CJ, Donahue MJ. Growth-mortality trade-offs along a depth gradient in *Cancer borealis*. *J Exp Mar Bio Ecol* 373: 133-139, 2009.

Lago-Fernandez LF. Spike Alignment in Bursting Neurons. *Neurocomputing* 70: 1788-1791, 2007.

Latorre R, Rodriguez FB, Varona P. Neural signatures: multiple coding in spiking-bursting cells. *Biol Cybern* 95: 169-183, 2006.

LeMasson G, Marder E, Abbott LF. Activity-dependent regulation of conductances in model neurons. *Science* 259: 1915-1917, 1993.

Lenz PH, Hower AE, Hartline DK. Temperature compensation in the escape response of a marine copepod, *Calanus finmarchicus* (Crustacea). *Biol Bull* 209: 75-85, 2005.

Levitan IB. Modulation of ion channels in neurons and other cells. *Annu Rev Neurosci* 11: 119-136, 1988.

Leys C, Ley C, Klein O, Bernard P, Licata L. Detecting outliers: Do not use standard deviation around the mean, use absolute deviation around the median. *Journal of Experimental Social Psychology* 49: 764-766, 2013.

Liu Z, Golowasch J, Marder E, Abbott LF. A model neuron with activity-dependent conductances regulated by multiple calcium sensors. *J Neurosci* 18: 2309-2320, 1998.

Long MA, Fee MS. Using temperature to analyse temporal dynamics in the songbird motor pathway. *Nature* 456: 189-194, 2008.

Lu J, Tapia JC, White OL, Lichtman JW. The interscutularis muscle connectome. *PLoS Biol* 7: e32, 2009.

MacLean JN, Zhang Y, Goeritz ML, Casey R, Oliva R, Guckenheimer J, Harris-Warrick RM. Activity-independent coregulation of IA and Ih in rhythmically active neurons. *J Neurophysiol* 94: 3601-3617, 2005.

MacLean JN, Zhang Y, Johnson BR, Harris-Warrick RM. Activity-independent homeostasis in rhythmically active neurons. *Neuron* 37: 109-120, 2003.

Manor Y, Bose A, Booth V, Nadim F. Contribution of synaptic depression to phase maintenance in a model rhythmic network. *J Neurophysiol* 90: 3513-3528, 2003.

Maran SK, Sieling FH, Demla K, Prinz AA, Canavier CC. Responses of a bursting pacemaker to excitation reveal spatial segregation between bursting and spiking mechanisms. *J Comput Neurosci* 31: 419-440, 2011.

Marder E. Computational Dynamics in Rhythmic Neural Circuits. *Neuroscientist* 3: 295-302, 1997.

Marder E. Variability, compensation, and modulation in neurons and circuits. *Proc Natl Acad Sci U S A* 108 Suppl 3: 15542-15548, 2011.

Marder E, Abbott LF. Theory in motion. *Curr Opin Neurobiol* 5: 832-840, 1995.

Marder E, Bucher D. Understanding circuit dynamics using the stomatogastric nervous system of lobsters and crabs. *Annu Rev Physiol* 69: 291-316, 2007.

Marder E, Calabrese RL. Principles of rhythmic motor pattern generation. *Physiol Rev* 76: 687-717, 1996.

Marder E, Eisen JS. Electrically coupled pacemaker neurons respond differently to same physiological inputs and neurotransmitters. *J Neurophysiol* 51: 1362-1374, 1984.

Marder E, Goaillard JM. Variability, compensation and homeostasis in neuron and network function. *Nat Rev Neurosci* 7: 563-574, 2006.

Marder E, Taylor AL. Multiple models to capture the variability in biological neurons and networks. *Nat Neurosci* 14: 133-138, 2011.

Marder E, Weimann J. Modulatory control of multiple task processing in the stomatogastric nervous system. In: *Neurobiology of Motor Programme Selection: New Approaches to the Study of Behavioural Choice*, edited by Kien J, McCrohan C, and Winlow W. New York: Pergamon Press, 1992.

Maynard DM, Dando MR. The structure of the stomatogastric neuromuscular system in *Callinectes sapidus*, *Homarus americanus* and *Panulirus argus* (Decapoda Crustacea). *Philos Trans R Soc Lond B Biol Sci* 268: 161-220, 1974.

Maynard DM, Selverston AI. Organization of the stomatogastric ganglion of the spiny lobster IV: The pyloric system. *J Comp Physiol* 100: 161-182, 1975.

McCormick DA, Huguenard JR. A model of the electrophysiological properties of thalamocortical relay neurons. *J Neurophysiol* 68: 1384-1400, 1992.
McCormick DA, Pape HC. Properties of a hyperpolarization-activated cation current and its role in rhythmic oscillation in thalamic relay neurones. *J Physiol* 431: 291-318, 1990.
Metzger R, Sartoris FJ, Langenbuch M, Portner HO. Influence of elevated CO(2) concentrations on thermal tolerance of the edible crab *Cancer pagurus*. *J Therm Biol* 32: 144-151, 2007.
Meyrand P, Marder E. Matching neural and muscle oscillators: control by FMRFamide-like peptides. *J Neurosci* 11: 1150-1161, 1991.
Miller JP, Selverston AI. Mechanisms underlying pattern generation in lobster stomatogastric ganglion as determined by selective inactivation of identified neurons. IV. Network properties of pyloric system. *J Neurophysiol* 48: 1416-1432, 1982.
Moran MM, Xu H, Clapham DE. TRP ion channels in the nervous system. *Curr Opin Neurobiol* 14: 362-369, 2004.
Morris J, Maynard DM. Recordings from the stomatogastric nervous system in intact lobsters. *Comparative Biochem and Physiol* 33: 969-974, 1970.
Morris LG, Hooper SL. Mechanisms underlying stabilization of temporally summated muscle contractions in the lobster (*Panulirus*) pyloric system. *J Neurophysiol* 85: 254-268, 2001.
Morris LG, Hooper SL. Muscle response to changing neuronal input in the lobster (Panulirus interruptus) stomatogastric system: spike number- versus spike frequency-dependent domains. *J Neurosci* 17: 5956-5971, 1997.
Morris LG, Thuma JB, Hooper SL. Muscles express motor patterns of non-innervating neural networks by filtering broad-band input. *Nat Neurosci* 3: 245-250, 2000.
Myers BR, Sigal YM, Julius D. Evolution of thermal response properties in a cold-activated TRP channel. *PLoS One* 4: e5741, 2009.
Nadim F, Booth V, Bose A, Manor Y. Short-term synaptic dynamics promote phase maintenance in multi-phasic rhythms. *Neurocomputing* 52: 79-87, 2003.
Nusbaum MP, Beenhakker MP. A small-systems approach to motor pattern generation. *Nature* 417: 343-350, 2002.
O'Leary T, Williams AH, Caplan JS, Marder E. Correlations in ion channel expression emerge from homeostatic tuning rules. *Proc Natl Acad Sci U S A* 110: E2645-E2654, 2013.
Oprisan SA, Prinz AA, Canavier CC. Phase resetting and phase locking in hybrid circuits of one model and one biological neuron. *Biophys J* 87: 2283-2298, 2004.
Ouyang Q, Goeritz M, Harris-Warrick RM. Panulirus interruptus Ih-channel gene PIIH: modification of channel properties by alternative splicing and role in rhythmic activity. *J Neurophysiol* 97: 3880-3892, 2007.
Pearson KG, Wolf H. Comparison of motor patterns in the intact and deafferented flight system of the locust. . *J Comp Physiol A* 160: 259-268, 1987.
Peck JH, Nakanishi ST, Yaple R, Harris-Warrick RM. Amine modulation of the transient potassium current in identified cells of the lobster stomatogastric ganglion. *J Neurophysiol* 86: 2957-2965, 2001.

Pinsker HM. Aplysia bursting neurons as endogenous oscillators. I. Phase-response curves for pulsed inhibitory synaptic input. *J Neurophysiol* 40: 527-543, 1977.

Pinsker HM, Kandel ER. Short-term modulation of endogenous bursting rhythms by monosynaptic inhibition in Aplysia neurons: effects of contingent stimulation. *Brain Res* 125: 51-64, 1977.

Preuss T, Faber DS. Central cellular mechanisms underlying temperature-dependent changes in the goldfish startle-escape behavior. *J Neurosci* 23: 5617-5626, 2003.

Prinz AA. Computational approaches to neuronal network analysis. *Philos Trans R Soc Lond B Biol Sci* 365: 2397-2405, 2010.

Prinz AA, Abbott LF, Marder E. The dynamic clamp comes of age. *Trends in Neurosciences* 27: 218-224, 2004a.

Prinz AA, Billimoria CP, Marder E. Alternative to hand-tuning conductance-based models: construction and analysis of databases of model neurons. *J Neurophysiol* 90: 3998-4015, 2003a.

Prinz AA, Bucher D, Marder E. Similar network activity from disparate circuit parameters. *Nat Neurosci* 7: 1345-1352, 2004b.

Prinz AA, Thirumalai V, Marder E. The functional consequences of changes in the strength and duration of synaptic inputs to oscillatory neurons. *J Neurosci* 23: 943-954, 2003b.

Ransdell JL, Nair SS, Schulz DJ. Rapid homeostatic plasticity of intrinsic excitability in a central pattern generator network stabilizes functional neural network output. *J Neurosci* 32: 9649-9658, 2012.

Raper JA. Nonimpulse-mediated synaptic transmission during the generation of a cyclic motor program. *Science* 205: 304-306, 1979.

Rathbun MJ. The cancroid crabs of America of the families Euryalidae, Portunidae, Atelecyclidao, Cancridao and Xanthidae. In: *US National Museum Bulletin*, edited by Institution S1930, p. 193.

Rezer E, Moulins M. Expression of the crustacean pyloric pattern generator in the intact animal. *J Comp Physiol* 153: 17-28, 1983.

Rezer E, Moulins M. Humoral induction of pyloric rhythmic output in lobster stomatogastric ganglion: in vivo and in vitro studies. *J Exp Biol* 163: 209-230, 1992.

Rinberg A, Taylor AL, Marder E. The effects of temperature on the stability of a neuronal oscillator. *PLoS Comput Biol* 9: e1002857, 2013.

Robertson RM, Money TGA. Temperature and neuronal circuit function: compensation, tuning and tolerance. *Curr Opin Neurobiol* 22: 724-734, 2012.

Robertson RM, Xu H, Shoemaker KL, Dawson-Scully K. Exposure to heat shock affects thermosensitivity of the locust flight system. *J Neurobiol* 29: 367-383, 1996.

Saideman SR, Blitz DM, Nusbaum MP. Convergent motor patterns from divergent circuits. *J Neurosci* 27: 6664-6674, 2007.

Schulz DJ, Goaillard JM, Marder E. Variable channel expression in identified single and electrically coupled neurons in different animals. *Nat Neurosci* 9: 356-362, 2006.

Schulz DJ, Goaillard JM, Marder EE. Quantitative expression profiling of identified neurons reveals cell-specific constraints on highly variable levels of gene expression. *Proc Natl Acad Sci U S A* 104: 13187-13191, 2007.

Selverston AI. Invertebrate central pattern generator circuits. *Philos Trans R Soc Lond B Biol Sci* 365: 2329-2345, 2010.

Selverston AI, Miller JP. Mechanisms underlying pattern generation in lobster stomatogastric ganglion as determined by selective inactivation of identified neurons. I. Pyloric system. *J Neurophysiol* 44: 1102-1121, 1980.

Selverston AI, Moulins M. Oscillatory neural networks. *Annu Rev Physiol* 47: 29-48, 1985.

Sharp AA, O'Neil MB, Abbott LF, Marder E. The dynamic clamp: artificial conductances in biological neurons. *Trends Neurosci* 16: 389-394, 1993a.

Sharp AA, O'Neil MB, Abbott LF, Marder E. Dynamic clamp: computer-generated conductances in real neurons. *J Neurophysiol* 69: 992-995, 1993b.

Sieling FH, Canavier CC, Prinz AA. Predictions of phase-locking in excitatory hybrid networks: excitation does not promote phase-locking in pattern-generating networks as reliably as inhibition. *J Neurophysiol* 102: 69-84, 2009.

Skinner FK, Mulloney B. Intersegmental coordination in invertebrates and vertebrates. *Curr Opin Neurobiol* 8: 725-732, 1998.

Smarandache CR, Daur N, Hedrich UBS, Stein W. Regulation of motor pattern frequency by reversals in proprioceptive feedback. *Eur J Neurosci* 28: 460-474, 2008.

Sober SJ, Sabes PN. Multisensory integration during motor planning. *J Neurosci* 23: 6982-6992, 2003.

Soofi W, Archila S, Prinz AA. Co-variation of ionic conductances supports phase maintenance in stomatogastric neurons. *J Comput Neurosci* 33: 77-95, 2012.

Soto-Trevino C, Thoroughman KA, Marder E, Abbott LF. Activity-dependent modification of inhibitory synapses in models of rhythmic neural networks. *Nat Neurosci* 4: 297-303, 2001.

Stehlik LL, Mackenzie CL, Morse WW. Distribution and abundance of four brachyuran crabs on the northwest Atlantic shelf. *Fish Bull* 89: 473-492, 1991.

Stein W. Modulation of stomatogastric rhythms. *J Comp Physiol A* 195: 989-1009, 2009.

Swensen AM, Bean BP. Ionic mechanisms of burst firing in dissociated Purkinje neurons. *J Neurosci* 23: 9650-9663, 2003.

Swensen AM, Bean BP. Robustness of burst firing in dissociated purkinje neurons with acute or long-term reductions in sodium conductance. *J Neurosci* 25: 3509-3520, 2005.

Szucs A, Pinto RD, Rabinovich MI, Abarbanel HD, Selverston AI. Synaptic modulation of the interspike interval signatures of bursting pyloric neurons. *J Neurophysiol* 89: 1363-1377, 2003.

Tang LS, Goeritz ML, Caplan JS, Taylor AL, Fisek M, Marder E. Precise temperature compensation of phase in a rhythmic motor pattern. *PLoS Biol* 8: 2010.

Tang LS, Taylor AL, Rinberg A, Marder E. Robustness of a rhythmic circuit to short- and long-term temperature changes. *J Neurosci* 32: 10075-10085, 2012.

Taylor AL, Goaillard JM, Marder E. How multiple conductances determine electrophysiological properties in a multicompartment model. *J Neurosci* 29: 5573-5586, 2009.

Taylor AL, Hickey TJ, Prinz AA, Marder E. Structure and visualization of high-dimensional conductance spaces. *J Neurophysiol* 96: 891-905, 2006.

Temporal S, Desai M, Khorkova O, Varghese G, Dai A, Schulz DJ, Golowasch J. Neuromodulation independently determines correlated channel expression and conductance levels in motor neurons of the stomatogastric ganglion. *J Neurophysiol* 107: 718-727, 2012.

Thirumalai V. Implications of cotransmission and neuromodulation for neural network function. Brandeis University, 2002.

Thompson SM, Masukawa LM, Prince DA. Temperature dependence of intrinsic membrane properties and synaptic potentials in hippocampal CA1 neurons *in vitro*. *J Neurosci* 5: 817-824, 1985.

Thuma JB, Hobbs KH, Burstein HJ, Seiter NS, Hooper SL. Temperature sensitivity of the pyloric neuromuscular system and its modulation by dopamine. *PLoS One* 8: e67930, 2013.

Thuma JB, Morris LG, Weaver AL, Hooper SL. Lobster (*Panulirus interruptus*) pyloric muscles express the motor patterns of three neural networks, only one of which innervates the muscles. *J Neurosci* 23: 8911-8920, 2003.

Tobin AE, Cruz-Bermudez ND, Marder E, Schulz DJ. Correlations in ion channel mRNA in rhythmically active neurons. *PLoS One* 4: e6742, 2009.

Tohidi V, Nadim F. Membrane resonance in bursting pacemaker neurons of an oscillatory network is correlated with network frequency. *J Neurosci* 29: 6427-6435, 2009.

Turrigiano G, LeMasson G, Marder E. Selective regulation of current densities underlies spontaneous changes in the activity of cultured neurons. *J Neurosci* 15: 3640-3652, 1995.

Vervaeke K, Hu H, Graham LJ, Storm JF. Contrasting effects of the persistent Na+ current on neuronal excitability and spike timing. *Neuron* 49: 257-270, 2006.

Weigeldt D, Böhm H, Heinzel H-G. Sensory feedback in the operating stomatogastric nervous system of the crab (*Cancer pagurus*). In: *The Crustacean Nervous System*, edited by Wiese K. Berlin: Springer-Verlag, 2002.

Weimann JM, Marder E, Evans B, Calabrese RL. The effects of SDRNFLRFamide and TNRNFLRFamide on the motor patterns of the stomatogastric ganglion of the crab *Cancer borealis*. *J Exp Biol* 181: 1-26, 1993.

Whelan PJ, Pearson KG. Comparison of the effects of stimulating extensor group I afferents on cycle period during walking in conscious and decerebrate cats. *Exp Brain Res* 117: 444-452, 1997.

Wolfart J, Debay D, Le Masson G, Destexhe A, Bal T. Synaptic background activity controls spike transfer from thalamus to cortex. *Nat Neurosci* 8: 1760-1767, 2005.

Yamaguchi A, Gooler D, Herrold A, Patel S, Pong WW. Temperature-Dependent Regulation of Vocal Pattern Generator. *J Neurophysiol* 100: 3134-3143, 2008.

Zhurov Y, Brezina V. Temperature compensation of neuromuscular modulation in aplysia. *J Neurophysiol* 94: 3259-3277, 2005.